FILE NOT INTENDED FOR PRODUCTION

Hierarchical imaging and computational analysis of three-dimensional vascular network architecture in the entire postnatal and adult mouse brain

Thomas Wälchli[1,2,3,4*], Jeroen Bisschop[1,2,3,4,5], Arttu Miettinen[6,7,8], Alexandra Ulmann-Schuler[9], Christoph Hintermüller[10], Eric P. Meyer[9], Thomas Krucker[11], Regula Wälchli[12], Philippe P. Monnier[5,13,14], Peter Carmeliet[15,16], Johannes Vogel[17,18], Marco Stampanoni[6,7,18]

[1]Group of CNS Angiogenesis and Neurovascular Link, Neuroscience Center Zurich, and Division of Neurosurgery, University and University Hospital Zurich, Switzerland; [2]Division of Neurosurgery, University Hospital Zurich, Zurich, Switzerland; [3]Group Brain Vasculature and Perivascular Niche, Division of Experimental and Translational Neuroscience, Krembil Brain Institute, Krembil Research Institute, Toronto Western Hospital, University Health Network, University of Toronto, Toronto, Ontario, Canada; [4]Division of Neurosurgery, Department of Surgery, Toronto Western Hospital, University of Toronto, Toronto, Ontario, Canada; [5]Department of Physiology, Faculty of Medicine, University of Toronto, Toronto, Ontario, Canada. [6]Swiss Light Source, Paul Scherrer Institute, Villigen, Switzerland; [7]Institute for Biomedical Engineering, University and ETH Zurich, Zurich, Switzerland; [8]Department of Physics, University of Jyväskylä, Jyväskylä, Finland; [9]Institute of Molecular Life Sciences, University of Zurich, Zurich, Switzerland; [10]Institute of Biomedical Mechatronics, Johannes Kepler University, Linz, Austria; [11]Novartis Institutes for BioMedical Research Inc, Emeryville, CA 94608, United States of America; [12]Department of Dermatology, Pediatric Skin Center, University Children's Hospital Zurich, Zurich, Switzerland; [13]Krembil Research Institute, Vision Division, Krembil Discovery Tower, Toronto, Ontario, Canada; [14]Department of Ophthalmology and Vision Sciences, Faculty of Medicine, University of Toronto, Toronto,

Ontario, Canada; [15]Laboratory of Angiogenesis and Vascular Metabolism, Department of Oncology, KU Leuven, B-3000 Leuven, Belgium; [16]Laboratory of Angiogenesis and Vascular Metabolism, VIB Center for Cancer Biology, VIB, B-3000 Leuven, Belgium; [17]Institute of Veterinary Physiology, Vetsuisse Faculty, University of Zurich, Zurich, Switzerland; [18]These authors contributed equally.

*Corresponding author:
Thomas Wälchli

Group of CNS Angiogenesis and Neurovascular link
Division of Neurosurgery
Neuroscience Center Zurich, and Division of Neurosurgery
University and University Hospital Zurich

Frauenklinikstrasse 10
CH-8057 Zürich / CH-8091 Zürich, Switzerland.
Phone : +41 44 635 32 16 / +41 79 243 86 10
Fax : +41 44 635 33 03

E-mail: waelchli@irem.uzh.ch
thomas.waelchli@usz.ch

Group of Brain Vasculature and Perivascular Niche
Division of Neurosurgery,
Krembil Neuroscience Institute

Toronto Western Hospital, University of Toronto
60 Leonard Avenue
Toronto, Ontario, M5T 2S8
+1 647 394 86 10

thomas.waelchli@uhn.ca
thomas.waelchli@uoft.ca

EDITORIAL SUMMARY This protocol uses vascular corrosion casting, hierarchical synchrotron radiation μCT imaging, and computational image analysis to assess the three-dimensional vascular network architecture in the entire adult and postnatal mouse brain.

TWEET New protocol for 3D hierarchical imaging (#μCT, #synchrotron) and computational analysis of the entire mouse brain vasculature @KrembilRI @ETH_en @UZH_en

COVER TEASER Hierarchical 3D imaging of mouse brain vasculature

ABSTRACT

The formation of new blood vessels and the establishment of vascular networks are crucial during brain development, in the adult healthy brain, as well as in various diseases of the central nervous system (CNS). Here, we describe a step-by-step protocol for our recently developed method that enables hierarchical imaging and computational analysis of vascular networks in postnatal- and adult mouse brains. The different stages of the procedure include resin-based vascular corrosion casting, scanning electron microscopy, synchrotron radiation and desktop μCT imaging, and computational network analysis. Combining these methods enables detailed visualization and quantification of the three-dimensional (3D) brain vasculature. Network features such as vascular volume fraction, branch point density, vessel diameter, -length, -tortuosity, and -directionality as well as extravascular distance can be obtained at any developmental stage from the early postnatal to the adult brain. This approach can be used to provide a detailed morphological atlas of the entire mouse brain vasculature at both the postnatal and the adult stage of development. Our protocol allows the characterization of brain vascular networks separately for capillaries and non-capillaries. The entire protocol, from mouse perfusion to vessel network analysis, takes approximately 10 days.

INTRODUCTION

The growth of tissues and organs during embryonic and postnatal development, tissue homeostasis in adulthood, as well as tumor growth, require adequate vascularization via the establishment of complex three-dimensional (3D) vascular networks and subsequent tissue perfusion and oxygenation[1-3]. In these physiological and pathological conditions, the formation of new blood vessels can occur via different mechanisms[1,2,4-6]. Vasculogenesis is defined as the *de novo* formation of blood vessels during which bone-marrow – respectively blood islets – derived angioblasts (endothelial progenitor cells) differentiate into endothelial cells[1,2]. Occurring throughout life, vasculogenesis is most active during embryonic and early postnatal development. Sprouting angiogenesis describes the formation of new blood vessels from pre-existing ones[2,3], relying on a number of spatiotemporally tightly regulated cellular mechanisms involving cell adhesion and -spreading, sprout initiation and -formation, endothelial tip cell migration, endothelial stalk cell proliferation, tube formation, and vessel anastomosis[1,2]. Another mechanism of physiological vessel formation that also occurs throughout the entire life span is intussusceptive angiogenesis, the process during which pre-existing vessels split and give rise to daughter vessels without a corresponding increase in the number of endothelial cells[1,7,8]. Besides these three modes of physiological blood vessel formation, which can also occur in pathological settings, three additional mechanisms modifying blood vessels have been described in pathological settings (mainly tumors)[4]. These include vascular co-option, describing the organization of tumor cells into perivascular cuffs around existing microvessels of the surrounding healthy tissue to allow the oxygenation of the early tumor mass[4,9,10]; vascular mimicry, defined as the integration of tumor cells into the blood vessel wall mimicking endothelial cells[11,12]; and glioma stem-to-endothelial or glioma stem-to-pericyte transdifferentiation[13-16]. The relative importance of these modes of vessel formation and modification in the formation of a well-established 3D vascular network depends on the

developmental stage and the pathology in the respective organs[1,2,5] and are still not completely understood[1].

Angiogenesis and vascular network formation in the postnatal and adult mouse brain

The human brain crucially depends on its vasculature for proper functioning as despite accounting for only 2% of the body mass it consumes 20% of the cardiac output and 20% of the oxygen and glucose of the entire body, corresponding to a 10-fold higher rate of energy metabolism compared to an equivalent tissue volume in the rest of the body[17,18]. The brain vasculature is constituted of a complex 3D vascular network of 644 kilometers (400 miles)[19,20], anatomically organized so that each individual neuron is not more than 22 to 27µm (in humans, depending on the cortical depth) away from the closest microcapillary, thereby assuring proper oxygen delivery[21,22]. In the mouse brain, the absolute numbers are obviously lower but show similar relative values[22-24].

Cerebral angiogenesis in mice and humans (and in all mammals) is highly active during embryonic and postnatal brain development and almost quiescent in the adult healthy brain[2,3,25], but is reactivated in vascular-dependent central nervous system (CNS) pathologies[6,26,27]. Thus, addressing how the brain vasculature network shapes from the developmental to the adult stage is crucial for a better understanding of underlying vascular dynamics also in pathological conditions[6,28].

In the developing mouse brain, the functional, perfused vascular network of the CNS parenchyma is established following multiple distinct steps: it starts at around embryonic day 7.5 – 8.5 (E7.5 – E8.5) with the formation of the perineural vascular plexus (PNVP, responsible for the vascularization of the future meninges)[29,30,31] via vasculogenesis in the ventral neural tube following a ventral-to-dorsal gradient[6,32-34]. In a subsequent step, at around E9.5, vascular endothelial sprouts emanating from the PNVP invade the CNS parenchyma in a caudal to cranial direction, vascularizing the CNS tissue via sprouting angiogenesis, thereby forming the intraneural vascular plexus (INVP)[3,6,28,32,35,36]. The INVP is expanded and refined via

subsequent vessel sprouting, branching and anastomosis[6,32,35,36] while these vascular sprouts migrate from the PNVP radially inwards towards the ventricles[3,28,35]. These important angiogenic processes of blood vessel formation and remodeling start during embryonic CNS development[32,35] and continue at the postnatal stage of brain development[17,28,31,37-39]. The expansion and remodeling of the intricate 3D CNS vascular network is required in order to adapt to local metabolic needs and neural activity[28,37,38,40]. To stabilize the newly formed blood vessels, perivascular cell types of the neurovascular unit (NVU) such as vascular smooth muscle cells, pericytes, neurons and astrocytes, are recruited to the vessel wall[3,26,36,41-43], thereby establishing the mature, functional CNS vasculature[3,6,26,44]. The establishment of the CNS vascular network via sprouting angiogenesis requires a subset of specialized endothelial cell types: endothelial tip cells at the leading edge of the vascular sprout extend finger-like filopodia to sense environmental cues thereby guiding the blood vessel sprout towards gradients of pro-angiogenic growth factors such as vascular endothelial growth factor (VEGF), basic fibroblast growth factor (bFGF)[1-3,45,46], platelet-derived growth factor (PDGF)[47], Ephrins[48] and Angiopoietins (Angs)[49], and away from gradients of anti-angiogenic factors such as Thrombospondin[50,51], Endostatin[52], Angioarrestin[53], Netrin-1[54], Semaphorins 3A-B-E-F-G[55] or Nogo-A[38,39]. Behind the leading tip cells, endothelial stalk cells elongate the growing vascular sprout as they proliferate and form the vascular lumen[1-3,56-58]. Neighboring sprouts then fuse and form vascular anastomosis resulting in perfusion of the newly formed vessels[1-3,57,59-61]. While the new blood vessel further matures and reaches a functional stage, its endothelial cells acquire a quiescent state, called endothelial phalanx cells[1,2,62]. Perfusion is a prerequisite for the stabilization and maintenance of a functional vascular network, acting most likely via flow-induced shear-stress related signaling pathways, such as the Sphingosine 1-Phosphate Receptor 1 (S1PR1) signaling[63-66] and the VEFR-2[67] and flow-induced dose-dependent expression of the transcription factor Krüppel-like factor 2 (KLF2)[68,69], which regulates the expression of various antioxidative and anti-inflammatory mediators to stabilize the vessel wall. Accordingly, the

absence of perfusion of newly formed vascular sprouts leads to vessel regression, fine-tuned mainly by non-canonical Wnt signaling[70-72]. Whereas sprouting angiogenesis and vascular remodeling remain highly dynamic throughout the first postnatal month until around postnatal day 25 (P25) – with a peak in endothelial cell proliferation at around postnatal day 10 (P10)[25] – most of these redundant newly formed vessel sprouts undergo strategic pruning (most likely influenced by regional metabolic needs related to neural activity) and only a small fraction ends up forming mature perfused capillaries[25]. After the first month, the number of vessel segments remains largely constant and the vascular network stabilizes, followed by a progressively decreased turnover between formed and eliminated vessels during physiological aging[25].

Reactivation of developmentally active angiogenic signaling cascades in vascular-dependent CNS pathologies and the concept of the neurovascular link (NVL)

Cerebral angiogenesis is highly active during embryonic and postnatal brain development and almost quiescent in the adult healthy brain[2,3,25]. In a variety of angiogenesis-dependent CNS pathologies such as brain tumors, brain arteriovenous malformations, or stroke, developmental signaling programs driving angiogenic growth during development are reactivated[1,2,6], thereby activating endothelial- and perivascular cells of the NVU[3,6,73]. However, which (developmental) molecular signaling cascades are reactivated in these angiogenesis-dependent CNS pathologies and how they regulate angiogenesis and vascular network formation on a cellular and subcellular level is not well understood. Thus, more knowledge is needed to better define the mechanisms of angiogenesis and vascular network formation during brain development, in the adult healthy brain as well as in brain pathologies.

Directly related to this reactivation of developmentally active signaling cascades is the concept of the neurovascular link (NVL), defining the cellular and molecular basis of the parallel organization and alignment of arteries and nerves in the brain, which is of crucial importance to understand brain vascular development, both at the embryonic and at the postnatal stage[6,26].

At the (sub)cellular level, the growth cones of newly formed axons resemble the endothelial tip cells of sprouting blood vessels[3]. Microenvironmental stimulating and inhibiting signals result in extension and retraction of these structures thereby inducing directed movements of growing nerves and blood vessels[6,26,42]. At the functional level, numerous common molecular cues that guide both endothelial tip cells and axonal growth cones via these specialized cellular and subcellular structures have been discovered[3,6,74]. As angiogenesis is highly active during postnatal brain development[37,38,75], it provides an adequate model system to address the process of sprouting angiogenesis, which is the predominant mode of vessel formation in the brain[6,32]. Molecularly, sprouting angiogenesis and endothelial tip cells are regulated via numerous signaling axes. For instance, endothelial tip cells are, similar to axonal growth cones, guided by the interplay of attractive and repulsive cues such as the classical axonal guidance molecules Netrins, Semaphorins, Slits and Ephrins, as well as the neural growth inhibitor Nogo-A[3,4,6,26,38,39]. We have previously shown that in mice lacking functional Nogo-A, additional endothelial tip cells and vascular sprouts and can result in an increased number of perfused blood vessels that integrate into the vascular network[28,38].

It is further known that the transition from sprouting endothelial tip cells to functional, perfused blood vessels that integrate into vascular networks is mainly regulated by the VEGF-VEGFR-delta-like ligand 4 (Dll4)-Jagged1-Notch pathway[1,2,61,76-81], thought to be a central pattern generator of vascular sprout- and endothelial tip cell formation. The spatiotemporally tightly regulated balance between endothelial tip- and stalk cell numbers and the balance between tip migration and stalk proliferation affect branching frequency and plexus density[77]. It was also shown that disturbance of these molecular processes may result in non-productive angiogenesis with the formation of aberrant blood vessels[79-83]. Importantly, the remodeling of the final perfused vascular network exerting its crucial functions depends on many different factors that include tissue-specific metabolic and mechanical feedbacks from the microenvironment as well as blood-flow related signaling pathways, respectively[72]. Nowadays, these processes of

vascular remodeling from the developing to the adult, mature stage are incompletely understood[61].

For instance, most of the numerously generated vascular sprouts in the first postnatal, highly angiogenic month in the mouse brain, undergo pruning and only a small fraction results in functional, perfused capillaries[25]. Thereafter the brain vascular network remains relatively stable. Nevertheless, despite the vascular stability at the adult stage, some vessel formation and elimination continue throughout life[25].

Another interesting aspect is that while we observed a significantly increased vessel density in young postnatal mice lacking function Nogo-A, this effect was almost completely gone in the adult Nogo-A$^{-/-}$ mice[38], raising questions regarding compensatory mechanisms by other molecules in the Nogo-A$^{-/-}$ mice but also regarding the plasticity of the vasculature in the young postnatal versus the adult stage.

These findings underline the need for a detailed protocol to describe how to quantitatively chart the 3D architecture of the brain vascular network of mice at any postnatal age. The protocol presented here will enable the mechanical and metabolic feedback that is finally responsible for maturation and stability of functional, perfused, 3D vascular networks to be investigated[72]. It allows direct and quantitative comparison of the brain vascular network tree between different postnatal and / or adult developmental stages as well as to distinguish capillaries and non-capillary blood vessels based on various parameters such as vascular volume fraction, vascular branch point density and -degree, vessel segment length, -diameter, -volume, -tortuosity, -directionality, and extravascular distance.

Development of the protocol

Vascular network formation has previously been evaluated using vascular corrosion casting techniques in mice at the embryonic, postnatal and adult stages of development. In mice at the

embryonic stage (8.5-13 days of gestation), vascular corrosion casting has been applied to investigate embryonic aortic development[86] and the fetal circulation in relation to the placenta[84,85]. In adult mice, vascular corrosion casting techniques are widely used in all major organs, and have been shown, for example, to be particularly useful to study cochlear vasculature in age-related hearing loss[86-89], the microvasculature in the urine bladder[90], and to investigate alveolar anatomy during both physiological development[91,92] and in several diseases[93,94].

Vascular corrosion casting is a well-established technique to study cerebrovascular anatomy in physiological settings in mice[39,95-103]. Angiogenesis and vascular network morphology have previously been described by our group using vascular corrosion casting in the adult healthy mouse brain[28,38], for instance using brain-specific $VEGF_{165}$-overexpressing mice (age: 16±2 weeks = P112) to study the effects of this pro-angiogenic stimulus on the adult brain vascular network[104]. Moreover, various vascular-dependent CNS pathologies have been investigated using the technique. As an example, we previously applied brain vascular corrosion casting to mouse models of Alzheimer's disease using APP23 transgenic mice (age: ranging from 3 to 27 months of age = P90 to P810)[105,106]. Others described the application of the technique to pathologies such as brain arteriovenous malformations utilizing *Alk-1*$^{2f/2f}$ (exons 4-6 flanked by loxP-sites) VEGF stimulated mouse models[107,108], microvascular networks in brain tumors in rats and primates using gliosarcoma xenotransplantation[109], post-traumatic brain injury models[110], transient focal cerebral ischemia in rats[111], and traumatic brain injury in postmortem human patients[112].

Recently, we have adapted the vascular corrosion casting technique enabling to describe the effects of the well-known axonal growth-inhibitory protein Nogo-A, which we have previously identified as a negative regulator of CNS angiogenesis and endothelial tip cell filopodia[38], on the 3D vascular network in the postnatal mouse brain[39].

Here, we demonstrate an optimized adaptation and extension of these previously described methods, allowing hierarchical imaging and computational analysis of the vascular network tree during any postnatal brain developmental stage in the mouse brain. Using vascular corrosion casting, hierarchical, desktop- and SRμCT-based imaging and image analysis we provide a refined, quantitative 3D analysis generating absolute parameters, characterizing the entire 3D mouse brain vessel network at a μm-resolution.

Overview of the procedure

Here, we present a technique for the visualization and computational analysis of the 3D vascular network in the postnatal and adult mouse brain. Figure 1 illustrates the different steps of the procedure with the corresponding timescale. A more detailed description of the procedure is provided in the paragraph "Experimental Design - Detailed description of the procedure". Briefly, the protocol starts with transcardial perfusion of artificial cerebrospinal fluid (ACSF) containing Heparin, followed by 4% (wt/vol) paraformaldehyde in phosphate-buffered saline (PBS) and the resin PU4ii (vasQtec, Zürich, Switzerland) at the desired day of postnatal development (in our case P10, corresponding to the peak of endothelial cell proliferation in the mouse brain according to Harb et al., *J Cereb Blood Flow Metab,* 2013[25]) or adulthood (in our case P60) (Steps 1-8) (Figures 2,3, Extended Data Figure 1). This is followed by resin curing (overnight) (Step 9), soft tissue maceration (for 24h) (Step 11), decalcification of the surrounding bone structures (overnight) (Step 12), dissection of the cerebral vascular corrosion casts from the remaining extracranial vessels (Step 13), followed by subsequent washing (Step 14), sputter-coating with gold on a subset of casts (Step 15), contrasting (osmium tetroxide) (Step 16), another round of washing (Step 17), freeze-drying (lyophilization) (Step 18), mounting and evaluation by Scanning Electron Microscopy (SEM) of a subset of casts (Steps 19-20) (Extended Data Figure 2 Supplementary Figure 1), optional low-resolution desktop-μCT scanning for region-of-interest selection (Steps 21-22), high-resolution SR-μCT or

desktop-μCT scanning (Steps 23-24), computational analysis (Steps 25-49), and statistical analysis (Step 50) (Figure 4).

Applications of the protocol

The protocol comprises vascular corrosion casting, hierarchical imaging and computational analysis of individual vessel segments of the 3D vascular network in postnatal and adult mouse brains. The method distinguishes between vessels of different diameters, for instance between capillaries (inner diameter of < 7 μm) and non-capillaries (inner diameter ≥ 7 μm). The protocol allows the influence of any angiogenic molecule to be studied including pharmacological compounds and blocking antibodies, and to test their pro- or antiangiogenic effects on vascularization and various specific parameters of the vascular network in postnatal as well as adult wild-type or genetically modified mice[38,113]. Importantly, the method provides a detailed quantitative description of the 3D vasculature allowing precise comparison of different experimental settings or genetic modifications. Quantitative information gained include vascular volume fraction, vascular branch point density and -degree, vessel segment length, -diameter, -volume, -tortuosity, -directionality, and extravascular distance, on both the level of global vascular network morphometry as well as local vascular network topology. This is quite different from the classical use of the corrosion cast technique for which in general only gross visual comparisons have been made and described. Importantly, the method could be used with laboratory/desktop μCT scanners only, which significantly increases the applicability of the protocol as compared to combined desktop μCT plus SRμCT setups. The protocol can also be applied to the analysis of the 3D vascular network in the entire mouse brain by creating artefact-free, high-resolution images of the complete and intact vascular corrosion cast, allowing the vascular network morphology of any given region of interest to be visualized within the mouse brain. This improves precision and is a significant simplification in contrast to the two-step ROI-based approach during which the ROIs first have to be placed on a lower resolution

overview μCT scan with subsequent high-resolution SRμCT or desktop μCT scanning of selected ROIs. Finally, given the crucial role of angiogenesis and vascular networks during both tissue development as well as in various pathologies in- and outside the CNS[1,2,6,114,115], and referring to previous vascular corrosion casting-based analyses of Alzheimer's disease, brain tumors, and other pathologies[106,107,109,110], the improved method presented here can – after validation in other tissues or pathological conditions – in principle be applied to virtually any physiological or pathological setting.

Although corrosion casts represent only a snapshot in time, they can also serve as templates for blood flow simulations that can, in addition to simulating cerebral blood flow in healthy brains, be used to simulate impaired oxygen and nutrient supply as a consequence of altered vascular network architecture in different cerebrovascular pathologies, such as brain tumors, brain vascular malformations, and stroke.

Advantages of the protocol compared with alternative methods

The hierarchical imaging of vascular corrosion casts combined with the computational analysis at the level of individual vessel segments up to entire vascular networks in both the postnatal and adult mouse brain as described here has several key advantages as compared to alternative methods.

This method enables visualization and quantitative assessment of the structure of blood vessel networks in the developing postnatal as well as in the entire adult mature mouse brain down to the level of capillaries, with yet unmet precision.

The brain microvasculature has proven hard to image due to the small size of the capillaries and large regions of interest required for network-level analysis. Traditional, non-invasive, in-vivo imaging modalities such as Doppler tomography[116,117], μMRI[118] and magnetic resonance angiography[119], have a resolution in the range of tens of micrometers but that is not high enough

to detect the microvasculature (compared to the near 1 μm resolution in μCT imaging). Confocal single-photon and two-photon imaging can provide the required resolution but have depth limitations[22,25], whereas other, classical (automated) histology-based methods are often limited to smaller regions, can be disturbed by deformations of the tissue slices especially at high resolutions (thin slices) and are therefore not suitable for quantification of the brain vasculature on a network level[120-122]. Recently, light-sheet fluorescence microscopy (LSFM) of the stained blood vessel network in both cleared non-CNS[123,124] and in cleared CNS tissue[125-128] has received increasing attention. LSFM has proved to be a very attractive and efficient method for imaging of large vessel networks with relatively high resolution. Contrary to corrosion casting, the LSFM technique requires optically clear or cleared samples (for the excitation wavelength). In corrosion casting, there are no such requirements and therefore no possibility of typical LSFM artefacts such as shadowing or photobleaching. Routinely achievable isotropic resolution of μCT techniques is near 1 μm, but in LSFM the resolution is often anisotropic. For example, here we have an isotropic voxel size of 0.65 μm, compared to 1.625 μm x 1.625 μm x 3 μm achieved through multi-dye vessel staining, tissue clearing, and 3D LSFM in[127]. For analysis, anisotropic voxels are often resampled to isotropic voxel size corresponding to the lowest resolution component, as was also done in[127], resulting in isotropic voxel size of 3 μm for convolutional neural network vessel segmentation and subsequent analysis of the vasculature of the whole mouse brain[127].

Micro CT imaging with use of intravascular contrast agents is used both in-vivo and ex-vivo and made it possible to image the vasculature in whole organs in 3 dimensions with increasing resolution[103,129-132]. Ex-vivo, vascular corrosion casts have shown to be an excellent method to investigate brain vasculature in particular[39,100,102,103,105,106,133]. Corrosion casting, in combination with recent advances in imaging techniques for both for SRμCT and desktop μCT setups, as used in this protocol, results in a resolution that is at least 3 times higher (0.65 μm vs

2 µm pixel size) than another recent paper that used a similar approach to study the mouse brain vasculature[103].

The protocol used here allows the postnatal and adult CNS blood vessel network to be quantitatively described in detail down to the capillary level, (Figures 5-14, Extended Data Figures 3-6, Supplementary Figures 2-21), including visualization and quantification of vessel directionality in the x-, y-, z-planes (Figure 12, and Supplementary Figures 12-16,21), which provides important additional information. Moreover, it permits to distinguish between capillaries and non-capillaries using clearly defined morphological parameters. In this paper we classified a vessel as a capillary if its inner diameter was less than 7 µm (Figures 3,6-10). Similar morphological classification is more difficult and tedious with other, classical (automated) histology-based methods due to dye color variations, staining artefacts, and distortion of the true vessel diameter by perivascular cells[120-122]. Histology-based methods including recently published LSFM based methods[123-127] are also less precise in addressing inner vessel diameters.

Hierarchical imaging and computational reconstruction of the 3D vascular network via global vascular network morphometry and local vascular network topology allow accurate, complete and quantitative analysis and description of the 3D vessel structure in the postnatal- and the adult mouse brain at the network level. These computational 3D analyses result in vessel parameters (Figures 5-14, Extended Data Figures 3-6, Supplementary Figures 2-21) with direct biological relevance instead of single measures such as 'percentage of section area occupied by vessels', that are obtained in classical 2D-section analysis methods.

For instance, maximum intensity projections of tissue slices are often used, even though they lead to an overestimation of the vessel density, as the vascular volume fractions of multiple optical sections are summed up, an error that adds up with increasing section thickness. A 3D analysis resulting in true vessel volume fractions, therefore, provides more accurate quantifications of the vascular networks and also allow better comparison between different

studies. Three-dimensional analyses can be either obtained by combining vascular corrosion casting techniques with computational analysis as described here, or by stereological methods as we[28], and others[134] have previously reported.

In contrast to section analysis (2D, maximum intensity projections), computational analysis of 3D hierarchical images allows characterization of additional parameters of the vascular network such as vessel volume fraction, branch point density and -degree, vessel density, -diameter, -length, -tortuosity, -volume, -directionality, and extravascular distance (Figures 5-12, and Extended Data Figures 3-6). This is similar to the image analysis obtained from confocal *z*-stacks using stereological methods[28].

Our protocol allows clear identification of capillary (inner vessel diameter < 7 µm, Figure 6a,b) and non-capillary (inner vessel diameter ≥ 7 µm, Figure 6a,b) blood vessels based on the morphological criteria of the inner vessel diameter (Figures 3,6-10, Extended Data Figure 4-6, Supplementary Figures 2-8,17-19). This biologically important distinction is more difficult to address with classical immunofluorescence[120-122], *in vivo* imaging modalities such as µMRI[118], µCT[132,135], contrast-enhanced digital subtraction and CT angiography[136], as well as with more recently developed methods such as LSFM analyses, with which vessel diameter cannot be determined as adequately. Moreover, there is also a lack of reliable capillary markers[124-127] which otherwise might solve this issue for staining-based methods. Indeed, markers for capillary endothelial have been proposed in recent years, for instance, Mfsd2a[137], TFRC, SKC16a2, CA4, CXCL12, Rgcc, SPOCK2 and others that were recently identified in large endothelial single-cell-RNA sequencing datasets[138-140]. However, to the best of our knowledge, there is currently no established cellular marker that selectively labels capillaries, as all the proposed and above-mentioned markers also label non-capillary blood vessels, even though to a lesser extent[139,140]. Accordingly, the most adequate method for distinguishing capillary and non-capillary blood vessels is still based on the morphological criteria of the inner vessel

diameter, e.g. < 7 µm for capillaries versus ≥ 7 µm for non-capillary blood vessels (Figures 3,6-10, Extended Data Figure 4-6, and Supplementary Figures 2-8,17-19).

High-resolution hierarchical imaging and computational analyses enable the 3D visualization, quantification and characterization of the entire vascular brain network. These analyses permit to obtain various quantitative parameters at the level of both the entire vascular network as well as of individual vessel segments, such as the volume fraction, extravascular distance, branch point density and -degree, vessel density (entire vascular network), -diameter, -length, -tortuosity, -volume and -directionality (individual vessel segment) (Figures 5-10,12,13 Extended Data Figures 5,6, and Supplementary Figures 2-21). Moreover, the number of vessel branch points enables better understanding of the 3D aspects of vessel branching within the process of sprouting angiogenesis (Figure 8, Extended Data Figures 5,6, and Supplementary Figures 9-11), which constitutes the predominant model of vessel formation in the brain[3,28,39]. Interestingly, the combination of vessel branch point analyses with the above-mentioned distinction between capillaries and non-capillaries allows revealing underlying mechanisms of sprouting angiogenesis in different brain regions such as cortex, hippocampus, and superior colliculus (Figures 8, Extended Data Figures 5,6, Supplementary Figures 9-11). For instance, branching events emanating from the penetrating vessels of the INVP in the cortex can clearly be visualized and quantified (Figures 7,8). Such computational/quantitative analyses are not commonly feasible using either classical staining-based methods[120-122] or novel methods including LSFM[123-127].

This protocol enables functional consequences of the vascular network formation to be addressed, such as the extravascular distance – e.g. the shortest distance of any given point in the tissue to the next vessel structure (Figure 11, Supplementary Figures 2,20), which are more difficult to address throughout the whole brain with alternative methods.

In principle, for simultaneous analysis of vasculature and the surrounding tissue, our protocol can also be combined with immunofluorescence using various vascular markers, e.g., pericyte

markers (PDGFR-β, CD13), astrocyte markers (GFAP) or neuronal markers (Nf160 and Tub-βIII), to visualize perivascular cell types. This can be done by sectioning the resin perfused brains without tissue maceration and bony structure decalcification, thereby leaving the brains intact, followed by immunofluorescence staining. By mixing in specific fluorescent dyes with the resin solution, it is also possible to improve and specify the inherent fluorescence of PU4ii (Extended Data Figure 7). Accordingly, virtually any protein of interest can be analyzed in the morphological context of the developing postnatal and adult vascular network, without the risk of collapse or deformation of vascular structures that is often encountered with a staining-only, histological approach[120,122].

Recent technical improvements allow scanning the whole postnatal and adult brain vascular corrosion cast at once with the same resolution as the method involving ROI selection prior to the scan. This whole-brain scan allows to analyze any region of interest, even after SRμCT scanning (Figure 13, Supplementary Figures 17-21).

Limitations of the method

Despite the advantages described above, this method has some disadvantages and limitations.

In contrast to classical immunofluorescent-based methods, the technique described here is more labor-intensive. For instance, the imaging and analysis of the superficial vascular plexus of the postnatal retina[141,142] or of the embryonic hindbrain[33] – which both form a 2D flat vascular structure and are the most commonly used *in vivo* angiogenesis models – can easily be assessed, in principle even with a standard fluorescence microscope. The quantitative analysis of angiogenesis in the postnatal mouse brain[28] – in which the vasculature develops in 3D with vessel sprouting occurring in all directions – requires confocal imaging for proper analysis, thus resulting in longer image acquisition times and larger data sets as compared to the postnatal retina and embryonic hindbrain models[33,141]. The method using confocal imaging is similar

regarding labor-intensiveness to the protocol described here but cannot be applied at once to the whole brain vasculature.

Comparable to the immunofluorescent-based analysis of the postnatal mouse brain[28], the structural complexity of the postnatal- and adult mouse brain angioarchitecture requires meticulous navigation within each individual sample to assure that really equivalent brain areas are selected. This is crucial as vascular density and angiogenic activity vary considerably among different brain regions[37,39,103,127]. Navigation within postnatal mouse brain samples as prepared with the present protocol is hampered because even though the combination of vascular corrosion castings with histological staining (such as e.g. Nissl or H&E stains, which would disturb the immunofluorescence) is feasible (Extended Data Figure 7), these different kinds of sample preparation preclude the 3D hierarchical imaging as described. Therefore, for detailed navigation (and ROI placement, see Figure 4a-l) throughout the postnatal and adult mouse brain, we recommend referring to the Developing- and Adult Allen Mouse Brain Atlas or to other commonly used Mouse Brain Atlases (Figure 4a-l).

Radiopaque CT contrasts agents (e.g. radiopaque resin PU4ii) do not require soft tissue to be macerated prior to imaging and do not require staining with osmium tetroxide. This is in contrast to the resin PU4ii employed here. We would like to emphasize that a direct comparison of the imaging quality of different contrast agents/technologies is impossible to make without a dedicated comparative study of the different technologies. However, we could speculate that in the intact (not macerated), resin-perfused brain tissue, contrast arises from X-ray absorption differences between tissues and the resin PU4ii-perfused vessels, whereas in our case (macerated tissue), contrast arises from the difference in X-ray absorption between air and resin PU4ii-perfused vessels[143]. The non-macerated tissue is known to attenuate X-rays to a greater extent than air, thereby resulting in a less contrasted image as compared to techniques including tissue maceration[143].

This protocol for vascular corrosion casting and computational 3D analysis does not enable endothelial tip cells or newly formed but yet immature, non-perfused blood vessels to be directly identified as a percentage of functional, perfused vessels since only the perfused part of the vessel tree can be analyzed. Endothelial tip cells and immature non-perfused blood vessels can, however, be identified by combining vascular corrosion casting with classical immunofluorescence staining techniques (Extended Data Figure 7). Moreover, blood flow in the functional vessels cannot be measured. In light of the finding that an increased density of perfused blood vessels does not necessarily result in higher blood flow, as it has for instance been shown for transgenic overexpression of VEGF165 (= VEGF-A) in the adult mouse brain[104], this needs to be taken into account.

The protocol described here provides only snapshots of brain angiogenesis at given time-points for individual mice, and in consequence requires a relatively large number of animals in order to study the dynamics of angiogenesis and vascular network architecture over time. We have partially addressed this aspect here by comparing the P10 with the P60 mouse brain. Although methods to study *in vivo* angiogenesis in the developing postnatal and adult mouse brain are currently not widely available, methods for real-time imaging of the brain vasculature exist[25,40], and may, in the future, complement our protocol.

In contrast to immunofluorescent-based methods evaluating angiogenesis in the postnatal retina, in the embryonic hindbrain, and in the postnatal brain[28,141], the identification of and distinction between endothelial tip cells, trailing stalk cells, and filopodia is not possible with vascular corrosion casting and computational 3D analysis, thereby limiting the ability to characterize patterns of sprouting angiogenesis and to differentiate between active and quiescent vessel sprouts. Our protocol allows the distinction between capillaries and non-capillaries based on their inner diameter (Figures 3,6-10), and this is in principle possible for every other vessel of a given size (Figure 5, Extended Data Figure 3). However, it does not permit directly differentiation between arteries and veins or between arterioles and venules,

which have similar inner vessel diameters but different functionalities[103]. The differentiation between arteries and veins is possible using SEM images revealing different shapes of nuclei impressions on the vascular cast depending on arterial versus venous flow (e.g. elongated nuclei impression in arteries versus more round nuclei impressions in veins), as we have previously described[101]. SEM, does, however, not allow for computational analysis of the vascular parameters. To circumvent these problems, the combination of vascular corrosion casting and immunofluorescence using classical markers for arteries (such as EphrinB2[144], Jagged-1[145], Alk-1[146] etc.) and veins (such as VCAM-1[147], COUP-TFII[148], EphB4[149] etc.) (Extended Data Figure 7) allows both 3D computational analysis of the vascular network as well as parameters and arterio-venous differentiation to be undertaken.

Extravasation of intravascularly infused resin has been described in experimental liver[150] and mammary[151] tumor models. Although not described in brain vascular corrosion casting, and also not observed by us in the postnatal mouse brain with more angiogenic active vessels that are supposed to be leakier than mature vessels, some resin extravasation for example in vascular-dependent CNS pathologies associated with an impaired blood-brain barrier such as stroke, brain trauma or brain tumors cannot be excluded.

Another limitation of the described protocol is the invasive nature of the technique as the mice need to be sacrificed for resin perfusion (Figure 2, Extended Data Figure 1); similar to the other, above-mentioned techniques of mouse postnatal retina-, embryonic hindbrain-, and postnatal brain angiogenesis[28,35,141]. Vessel size index-MRI (VSI-MRI) has been proposed as a quantitative, non-invasive MRI derived imaging biomarker, for the non-invasive assessment of tumor blood vessel architecture and in order to evaluate the effects of vascular targeted therapy. The technique was validated in high-grade human gliomas[152] and a direct comparison between *in vivo* MRI and post mortem µCT vessel calibers showed excellent agreement in vessel size measurements[153]. However, the parameters addressed with VSI-MRI are limited to an estimation of fractional blood volume and blood vessel size (resolution of 1.875 x 1.875 mm

with a total matrix size of 240 x 218 mm), and the additional vascular parameters such as vessel length, tortuosity, vessel directionality, branch point density and extravascular distance addressed with our protocol are not measurable with VSI-MRI techniques[153].

EXPERIMENTAL DESIGN

Detailed description of the procedure

As a first step, after the animal is properly anesthetized, the chest is opened in order to gain access to the left ventricle (Figure 2a-f, Extended Data Figure 1a,b) (Steps 1-2). To this end, the skin is lifted with the forceps and then cut perpendicular to expose the sternum (Figure 2c,d,g,h, Extended Data Figure 1b) (Step 3). The sternum is then lifted and lateral cuts through the rib cage are made exposing the chest cavity. The rib cage flap is pulled back and fixed using a pin/needle and the pericardium is carefully removed using rounded forceps. The heart is lifted slightly using forceps and then a winged perfusion needle is inserted into the left ventricle through the apex and the point of insertion is sealed with instant glue (Figure 2e,i, Extended Data Figure 1c) (Steps 4-5). Note the insertion at a flat angle of about 30° (Figure 2e,i). Care must be taken during this procedure to avoid inserting the needle too deep into the heart in order to avoid damage of the atrioventricular valve. After proper placing and securing of the needle (using the wings of the needle and pins/needles) in the left ventricle, the right atrium is opened to allow the blood and perfused fluid to leave the circulation, providing unlimited outflow (Figure 2b,f,j, Extended Data Figure 1d, Supplementary Video 1) (Step 6). Perfusion of 5 ml (for P10 animals) and 20 ml (for adult animals) of artificial cerebrospinal fluid (ACSF) containing 25,000 U/L Heparin through the left ventricle, is followed by perfusion with 4% (wt/vol) paraformaldehyde (solved in PBS) in order to fixate the vasculature and prevent the blood vessels from collapsing, and the resin PU4ii solution (Steps 6-7). All perfusion solutions are perfused at a pressure of 90-100 mmHg (4 ml/min) for P10 mice and 100-120 mmHg (8 ml/min) for P60 mice. Successful perfusion is indicated by sufficient outflow of the solutions

from the opening in the right atrium and by the bluish appearance of the paws, snout and tail immediately after starting the resin perfusion (Figure 2f,j, Extended Data Figure 1d, Supplementary Video 1) (Step 8). After 24 hours of resin curing, soft tissue is macerated in 300-400 ml 7.5% (wt/vol) potassium hydroxide (KOH) for at least 24 hours, followed by incubation in 300-400 ml 5% (vol/vol) formic acid for another 24 hours to decalcify bony structures (Steps 9-12). The brain vascular corrosion cast is dissected out of the skull and freed from extracranial vessels (Figure 2k-n, Extended Data Figure 1e-h, Supplementary Video 1) (Step 13).

The principle of vascular corrosion casting is schematically shown in Figure 3. The step-by-step procedure of intracardial polymer resin perfusion, tissue maceration, bone decalcification, and brain dissection, is illustrated in Figure 2, in Extended Data Figure 1 and in Supplementary Video 1.

As an additional sidestep, not part of the main protocol pipeline, a combination of resin perfusion and immunofluorescence staining and imaging can be performed (Extended Data Figure 7) (Step 10). For this purpose, resin curing is immediately followed by removal of bony structures (without tissue maceration), in order to preserve soft tissue required for immunofluorescence staining. After cutting, the soft tissue slices are then incubated with any biological markers of interest such as Fluoro Myelin Red (Molecular Probe Inc) for myelin and DAPI. Additional to the inherent fluorescence of PU4ii, specific fluorescent dyes can be used (Extended Data Figure 7). For conventional immunofluorescence microscopy, we recommend a slice thickness of 100 to 150 µm.

For quality control, random samples of vascular corrosion casts are mounted on stubs and sputter-coated with gold[105,133] for SEM (SEM, Hitachi S4000) (see Extended Data Figure 2 for sufficiently perfused casts, see Supplementary Figure 1 for insufficiently perfused casts) (Steps 14-15, Step 20). Optionally scanning helium ion microscopy that does not require sputter

coating could be used for quality control. In this case, the same casts that will be μCT imaged can be used for quality control.

The casts that are to be μCT imaged are stained using osmium tetroxide to increase X-ray absorption, which leads to higher signal to noise ratio (SNR) and, thus, better contrast in X-ray imaging[104] (Steps 16-17). Afterwards, the osmicated casts are lyophilized overnight and mounted on plexiglas stubs or other suitable sample holders using cyanoacrylate glue (Steps 18-19). Optionally, the entire corrosion casts are first imaged with low-resolution desktop-μCT to select desired ROIs (Step 21-22). This step is not required if the whole casts are to be imaged. The corrosion casts are scanned with high-resolution desktop-, or SR-μCT (either preselected ROIs or the whole brain) and analyzed using a computational imaging processing pipeline (Step 23-24). The image analysis procedure allows segmentation of the 3D data such that voxels representing vessels are assigned value 1 and all other voxels are assigned value 0. Furthermore, this binary representation is converted into a vessel graph (Figure 4) that facilitates quantitative analysis of all network parameters, optionally separated for capillaries and non-capillaries, including vascular volume fraction (Figures 5-7, Extended Data Figures 3,4, Supplementary Figures 2-5), branch point density and branch point degree (Figure 8, Extended Data Figures 5,6, Supplementary Figure 6,9-11), segment density, -diameter, -length, -volume and -tortuosity (Figure 9,10, Supplementary Figure 7), extravascular distance (Figure 11, Supplementary Figure 8), and vessel directionality (Figure 12, Supplementary Figures 12-16) (Steps 25-49). Finally, the data extracted using image analysis procedures are evaluated statistically (Step 50).

Experimental animals

Although we have used C57/BL6 WT and Nogo-A$^{-/-}$ mice at the ages of P10 and P60, the present protocol is applicable to mice of any type, either sex, and at any postnatal and adult stage of development. To illustrate the potency of this technique in detecting the effects of

different molecules, proteins and drugs on 3D vessel morphology, we quantified the difference in 3D vessel morphology between healthy P10 and P60 mice as well as wildtype and Nogo-A$^{-/-}$ mice of either age. Importantly, as genetic or other experimental manipulations such as intraperitoneal antibody- or tamoxifen injections were described to affect the growth and thus the weight of animals[141], it is crucial to weigh the animals prior to resin perfusion. Although genetic modifications are not necessarily reflected to the same extent in all organs, similar weights and ages were chosen as parameters to ensure comparable developmental stages of mice between the different study groups. This is especially true for mouse pups at the early postnatal stage because the vasculature develops relatively fast at that stage[37]. Therefore, it is important to monitor the developmental stage of the mice (including age and weight of the animals) carefully . Since various genetic modifications were shown to alter the overall postnatal development, matching animal weight is important to enable comparative vessel structure analysis[154]. Moreover, littermate controls should always be used where available.

Power calculations based on the expected or biologically relevant difference between the groups should be made prior to the experiments. In principle, more pronounced differences between two test groups require a smaller number of animals to detect the effect and vice versa. Incorporation of appropriate controls, for instance, brains from postnatal wild-type littermates, is essential for analyses of angiogenesis and vascular network architecture in genetically modified mice during postnatal CNS development as well as in adulthood. For all quantitative analysis in the different brain regions (Figures 5-12, Extended Data Figures 5,6, Supplementary Figures 2-16), we used 4-6 postnatal (P10), and 8-12 adult (P60) animals, respectively. All animal procedures must be carried out in accordance with the guidelines outlined by the institutional and local review committees for animal experiments. All the animal experiments in this study were approved by the Veterinary Office of the Canton of Zurich (license number 173/2010).

Vascular corrosion casts - Resin PU4ii infusion

The resin we use, PU4ii (vasQtec, Zürich, Switzerland), is a polyurethane-based casting resin with superior physical and imaging characteristics, timely polymerization, minimal shrinking and low viscosity persisting up to 25 minutes using a 30% (wt/vol) dilution with ethylmethylketone (EMK), which guarantees perfusion into the finest capillaries[101] (Step 8). These casts are highly elastic while retaining their original structure to facilitate post-casting tissue dissection and pruning[101].

The adapted perfusion protocol had to be optimized for postnatal animals in order to fulfil two requirements: i) to perfectly fill the vessels with PU4ii, ii) to simultaneously preserve the mechanical vessel integrity in order to avoid rupture of the more immature vessels (Extended Data Figure 2, Supplementary Figure 1).

Therefore, mice (P10 or P60) are first intracardially perfused through the left ventricle with 10–20 ml ACSF containing 25,000 U/L Heparin, followed by 4% (wt/vol) paraformaldehyde (PFA) in PBS, and then by resin PU4ii (vasQtec, Zürich, Switzerland), at 90-100 mmHg (4 ml/min) for postnatal animals and 100-120 mmHg (8 ml/min) for adult mice (Steps 1-8). This adapted infusion pressure for P10 mice as compared to adult animals ensured mechanical stability preventing vessel rupture while ensuring at the same time adequate perfusion of the blood vessel network.

Resin curing, maceration/decalcification and brain dissection

After resin curing of the perfused mouse at room temperature for at least 24 hours (embedded in a diaper), the tissue is macerated in 7.5% (wt/vol) KOH at 50°C for 24 hours followed by decalcification of the surrounding bone structures with 5% (vol/vol) formic acid, also at 50°C for 24 hours (Figure 2k,l, Extended Data Figure 1e,f) (Steps 9-12). The cerebral vasculature is then dissected from the remaining extra-cranial vessels (Figure 2k-n, Extended Data Figure

1g,h) (Step 13). Subsequently, the cerebral vascular corrosion casts are washed thoroughly in distilled water and dried by lyophilization (Steps 14-15).

Imaging and quantification - Scanning electronic microscopy (SEM)

For qualitative control of the vascular corrosion casts, we inspect the perfused blood vessels of the entire mouse body including the whole brain by visual observation and conventional light microscopy (Extended Data Figure 2). Then, a subset of the casts is mounted on stubs and sputter-coated with gold[105] for quality control SEM imaging (SEM; Hitachi S4000)[105,133] (Step 15). Imaging of resin-perfused, dissected and osmicated P10 and P60, WT and Nogo-A$^{-/-}$ brain tissue samples reveals a dense vascular network in the superficial cortex with well-defined vessel structures of all sizes (Extended Data Figure 2). Moreover, the entire brain vasculature is uniformly filled and the vessel lumen was molded with its finest details (Extended Data Figure 2).

In addition, larger blood vessels show oval endothelial nuclei imprints on the resin cast surface, a quality feature also observed in vascular corrosion casts of adult mice demonstrating the perfect molding of the vascular lumen, suggesting complete filling (Extended Data Figure 2)[106]. The fine capillary network is well visible and devoid of vessel interruptions in the selected P10 and P60 brain cortices (Extended Data Figure 2). Taken together, all these morphological blood vessel features indicate that the vascular corrosion casts are of excellent quality.

Typical signs of insufficient vascular corrosion casting consist of irregular shapes combined with rounded abrupt ends of larger vessels, lacking endothelial nuclei imprints (Supplementary Figure 1). A possible interpretation is that the casting material is pushing against air introduced during the perfusion by gaseous solutions, and trapped in vessels interrupting the normal flow[155,156]. This increased pressure in the preceding vessel segment distorts the vessel surface. Moreover, absence of imprints of endothelial cell nuclei further indicates insufficient casting (Supplementary Figure 1).

Desktop µCT imaging and region of interest selection

Three-dimensional images of whole-brain samples are acquired using a desktop µCT system (µCT 40, Scanco Medical AG). Details can be found in Steps 21-24 of the PROCEDURE. The images are evaluated visually and desired ROIs in various anatomical regions of the brain are chosen. To assure precise navigation within the postnatal mouse brain parenchyma, we refer to the Developing Mouse Allen Brain Atlas (http://developingmouse.brain-map.org/docs/Overview.pdf) or – alternatively – to any other Mouse Brain Atlas. In order to find the same ROIs in the SRµCT imaging (see below), the coordinates of the ROIs are determined relative to well-distinguishable details in the sample. For this purpose, we employ two metallic pins in the sample holder rod. When scanning the entire vascular corrosion cast, ROI selection can be omitted.

Synchrotron radiation-based micro-CT (SRµCT)

We acquired high-resolution (pixel size 0.73 µm) SRµCT images of the selected ROIs at the TOMCAT beamline of the Paul Scherrer Institute (Switzerland). The ROIs are located using the steel pins in the sample holder rod as described above. X-ray projection images are acquired with monochromatic X-rays. Paganin phase retrieval[58,157] is performed before tomographic reconstruction using the Gridrec algorithm[58,158] (more details can be found in Steps 23-24 of the PROCEDURE).

Additionally, high-resolution images of selected whole-brain casts are acquired using a similar setup as compared to the ROI-based approach, now with 0.65 µm pixel size. Here, the field of view of a single tomographic image is too small to cover the whole brain, and thus we use mosaic imaging mode where multiple smaller, partially overlapping, images are acquired. The reconstructions are then stitched into a single large image representing the whole brain

vasculature[159]. The SRμCT images obtained in this protocol have an SNR > 10 (and typically in the range 20-30), and therefore they seemed to be well suited for computational reconstruction of the vascular network (Supplementary Video 2).

Alternatives for broader accessibility

In this protocol, we propose to use a desktop μCT scanner to acquire a low-resolution overview of the whole brain sample after which we use a SRμCT imaging approach to study the selected ROIs at a high-resolution in more detail (Figure 4a-l). Alternatively, both the low-resolution ROI selection and the high-resolution imaging of the selected ROIs (Figure 4a-l) can be performed using SRμCT techniques without the use of a desktop μCT scanner, for instance in case of well accessible SRμCT scanners and in order to avoid relocalization in different CT machines. As another alternative, all the imaging steps in this protocol can also be performed with a high-resolution desktop μCT scanner only (machines from manufacturers such as Scanco, Bruker, Zeiss, Phoenix and Nikon can be used) without the use and need of an often less accessible SRμCT scanner, and if the number of samples is relatively small as scanning times are higher with desktop μCT scanners.

Computational reconstruction - Vessel segmentation

The vessels in the SRμCT reconstructions are segmented to yield a binary image where the foreground represents vessels and background represents the structures in between them (Figure 4m-p). The high SNR allows us to use simple Otsu thresholding[58,160], where all pixels with a value above a specific, algorithmically determined, threshold are classified as vessels (Figure 4o). In the Otsu method, the threshold is chosen such that it minimizes the intensity variance of pixels inside both groups. The threshold value does not seem to be very sensitive to the selection of the thresholding method, provided that the selected method is suitable for thresholding

images with bivariate histograms. For example, other previously described methods[161-163] typically give threshold values that are within a 10% range of the value given by the Otsu method (Step 25).

The thresholding step is followed by morphological closing using a spherical structuring element (radius = 0.75 μm) in order to eliminate small gaps in the vessels. A few regions primarily located in the largest vessels contained small, isolated background regions (i.e. holes or bubbles) that were eliminated by merging all isolated background regions to the foreground (Steps 26-27).

Computational reconstruction - Vessel skeletonization

In order to analyze the individual vessel branches, we convert the segmented image into a graph representing the vessel network. To this end, the segmented vessels are first reduced into a one-pixel wide skeleton that approximated the centerline of each vessel branch[58]. This is done by iterative thinning of the structures until only lines were left[58,164] (Figure 4o,p).

The skeleton is traced into a graph structure, where each graph node corresponds to an intersection point between three or more skeleton branches, and the branches are represented by edges between the nodes. For each edge, the locations of the skeleton pixels that form the corresponding branch are stored. Additionally, for each stored location, the distance to the nearest non-vessel pixel is calculated in order to determine the (local) radius of the vessel[58,165] (Steps 28-30).

An anchored convolution approach is used to smooth the pixel-accurate representation of the vessel branches for more accurate length measurements and visualizations[58,166]. In the anchored convolution the locations of the points forming the branch are convolved with a Gaussian kernel, but the points are not allowed to move more than a specific distance from their original locations. As a result, small deviations in the curve will smooth out but larger ones remain. In

our case, the standard deviation of the smoothing Gaussian was 1.125 µm, and the maximum distance a point was allowed to move was 0.5 µm. The endpoints of each branch were not allowed to move at all (Step 31).

Finally, spurious branches originating from the ill-conditioned nature of the skeletonization procedure and from remaining imaging noise re removed using a simple heuristic. Therefore, all branches with at least one free end and a length of less than twice the radius at the non-free end are removed. Additionally, isolated branches less than 5 µm in length are erased, as these corresponded to small, spurious foreground regions not representing vessels (Steps 32-36).

The image analysis is done using the freely available pi2 software (version 3.0) (https://github.com/arttumiettinen/pi2) and Python 3.6.

Computational reconstruction - Global morphometry and local topological vascular network analysis

Global morphometry and local topological vascular network analysis are performed for each high-resolution image in collaboration with Nemtics (http://www.nemtics.com) and in accordance with our previous work[39]. Global morphometry analysis is based on the vessel segmentation map, it considers the characteristics of the vascular structure on a per-voxel level, and allows the vascular parameters vascular volume fraction and extravascular distance to be assessed.

In contrast to global morphometry analysis, using local topological analysis of the 3D vascular network individual per-vessel parameters, such as branch point density and -degree, vessel/segment density, -diameter, -length, -tortuosity, -directionality, can be evaluated and calculated in addition to the vascular volume fraction.

The nodes in the previously created graph are interpreted as branch points and the edges in between nodes as vessel segments. Branch points are junctions between at least three vessel

segments where the number of vessel segments joining in one branch point is called branch point degree (which equals at least 3). The branch points and all segments were categorized into capillary (diameter < 7 μm), non-capillary (diameter ≥ 7 μm) and global (without distinction by diameter) being the union of capillaries and non-capillaries (Step 37).

We define the branch point diameter as the diameter of the thickest joining segment, allowing the discrimination between capillary and non-capillary branch points. The branch point density per volume is defined as the number of branch points per cubic millimeter (Figure 8, and Extended Data Figures 5,6, Supplementary Figures 6,9-11).

The number of branch points per degree is counted and separated for capillaries, non-capillaries and global branch points in order to plot branch point degree and branch point diameter statistics (Supplementary Figures 6,9-11). The values per branch point degree are then divided by network volume to obtain branch point density statistics (Figure 8c,f-h, Extended Data Figures 5,6, Supplementary Figure 6,9-11) (Step 38).

All segments are classified into either capillary or non-capillary, counted and divided by network volume to plot segment density statistics (Figure 9d-f, Supplementary Figure 7a-c). Segment diameter is obtained as the average value of local vessel diameter over all the points defining the segment (Figure 9g-j, Supplementary Figure 7d-f) . Segment length is calculated as the sum of lengths of line segments between points defining the vessel segment (Figure 9k-n, Supplementary Figure 7g-i) (Steps 40-44). Tortuosity is calculated as the ratio between the real length of a segment and the shortest distance between the segment's endpoints (Figure 10a-d, Supplementary Figure 7j-l) (Step 45). In order to calculate segment volume, each of the line segments is assumed to represent a cylinder whose diameter is taken to be the average vessel diameter at its endpoints, and the sum of all the cylinder volumes give the segment volume (Figure 10e-h, Supplementary Figure 7m-o).

In order to determine extravascular distance, the Euclidean distance transform of the background in the segmented image is calculated. The distance transformation gives the

distance to the nearest vessel for each background point (Figure 11). Binning the distance values into a histogram gives an estimate of the extravascular distance distribution (Figure 11b,i-k, Supplementary Figure 8) (Step 46).

The volume fraction of global segments is determined as the ratio between the count of vessel voxels and the total count of voxels in the segmented image (Figure 5-7, Supplementary Figures 2-5). This value is then divided into capillary- and non-capillary volume fractions in proportion to the total volumes of vessels in these two vessel groups (Figure 7f-h). In the example demonstrated in this protocol, quantitative analysis of the relative angles of the vascular segments emanating from a certain branch point was performed for both the developing P10 and mature P60 stages (Figure 12d-f, Supplementary Figure 12c-e,h-j). Three-dimensional renderings of the computationally reconstructed vessel networks were obtained, color-coded by i) the average vessel radius (Figure 5e-g), ii) the division to capillary and non-capillary vessels (Figure 7d,e, Supplementary Figures 3a,b,4a,b), and iii) vessel directionality (Figure 12b,c, Supplementary Figures 12a,b,f,g,13-16) (Steps 47-49).

Computational reconstruction - Statistical analysis

For the ROI-based approach, the mean of the parameters obtained from the animals in the different groups (e.g. P10 WT, P10 Nogo-A$^{-/-}$, P60 WT and P60 Nogo-A$^{-/-}$) are compared using an appropriate t-test (we used the Welch t-test, which is an adoption of the Student t-test to better cope with unequal sample distribution variance).

Histograms and boxplots were used to visualize the data (Figures 5-13, Extended Data Figures 5,6, Supplementary Figures 2-12,17-21) (Step 50), with whiskers spanning at most 1.5 times the inter-quartile-range (IQR, the height of the boxes) above and below the 25% and 75% quartiles. Whiskers are drawn at the highest/lowest data value if it is inside the 1.5 IQR. In compliance with the standard[167], the open dot represents the mean, the horizontal line represents the median[167]. We used Matplotlib (https://matplotlib.org) and NumPy (https://numpy.org) for

statistical testing and figure plotting. For all quantitative analysis in the different brain regions (Figures 5-12, Extended Data Figures 5,6, Supplementary Figures 2-12) we used 4-6 postnatal (P10), and 8-12 adult (P60) animals. On average, we analyze about three ROIs per brain region. In addition to the ROI-based approach and in order to visualize the variability of the measured quantities in a single brain specimen, we use whole-brain images acquired for one P10 WT and one P60 WT sample. The whole-brain images were manually registered to the Allen Mouse Brain Atlas and divided into regions of the same size as the ROIs used earlier. The vascular network in the cortex, hippocampus, superior colliculus, corpus callosum, hippocampal subregions – CA1, CA3, and dentate gyrus –, basal ganglia, thalamus, hypothalamus, olfactory bulb, cerebellum, pons, and medulla were analyzed using the same approach (Figure 13, and Supplementary Figures 17-21). The anatomical regions are divided into 5-126 parts depending on the size of that region and quantified similarly to the ROI-based approach. The means of the parameters obtained from each animal in both groups (n=1 for P10 WT, n=1 for P60 WT) were compared using the Welch t-test. We used histograms and boxplot to visualize the data (Figure 13, and Supplementary Figures 17-21), as well as statistical testing and figure plotting undertaken as described for the ROI-based approach above (Step 50).

MATERIALS

ANIMALS

- 10-d-old and 2-month-old mice (We used wild type and Nogo-A$^{-/-}$ C57BL/6, male or female) (Charles River Laboratories)

! CAUTION Institutional and governmental ethics regulations concerning animal use must be followed. All the animal experiments herein were performed in accordance with governmental, institutional (University of Zurich), and ARRIVE guidelines, and had been approved by the Veterinary Office of the Canton of Zurich (license number 173/2010).

REAGENTS

! CAUTION Some of the chemical substances mentioned below are extremely harmful if inhaled and swallowed, and/or are irritating to the eyes, respiratory system and skin. They may cause sensitization of skin upon contact. Therefore, in principle, wear protective goggles, clothing and gloves as appropriate. Use the chemicals in a fume hood. Carefully read the safety data sheets of all chemicals used in this protocol.

- Pentobarbital solution 1.0 mg/mL in methanol (Sigma Aldrich cat. no. P-010)
- NaCl, 0.9% (wt/vol) in distilled water (250 ml) (BBraun cat. no. 3570110)
- Heparin Sodium Salt from Porcine, Grade 1A (Sigma Aldrich cat. no. H3393-25KU)
- Paraformaldehyde (PFA; Sigma-Aldrich, cat. no. P6148)
- PU-4ii Resin, Hardener, Color, Fluorescence (www.vasqtec.com)
- Ethylmethylketon (EMK) EMPLURA® (Merck cat. no. 106014)
- XTEND-IT®, dry Gas Blanket (Kaupo, cat. no. 09291-010-000012)
- Potassium hydroxide (KOH) (1 kg) (Merck cat. no. 1050331000)
- Formic Acid, 99% techn. (Fisher Scientific cat. no. 270480250)
- Osmium tetroxide solution, 2% (wt/vol) in water (5 ml) (Sigma Aldrich cat. no. 20816-12-0). **!CAUTION:** OsO_4 is very toxic. Work under a fume hood and use protection gloves, glasses and lab coat. Properly dispose the OsO_4 waste.
- PBS, 0.1 M, or PBS tablets (Sigma-Aldrich, cat. no. P4417)
- Mounting medium (Dako, cat. no. 53023)
- Instant adhesive (Cyanoacrylate) (Kisling, Ergo, cat. no. 5889)
- Distilled water (Millipore, Milli-Q synthesis A10)
- DAPI (4',6-Diamidino-2-Phenylindole, Dihydrochloride) Nucleic Acid Stain (Invitrogen™) (excitation/emission maxima: 358/461 nm) staining for cell nuclei

- FluoroMyelin Red (Invitrogen™) (excitation/emission maxima: 558/654 nm) staining for myelin

EQUIPMENT

- Tabletop balance (e.g., ED Precision balance, Sartorius)
- Plastic foil
- Paper towels
- Green protection diapers (Polymed Medical Center)
- Gloves (M/L) Nitril (Sigma-Aldrich cat. no. Z543500/Z543519)
- Syringes, 1 ml (BD Luer-Lok™ cat. no. 309628)
- Syringes, 50ml (Fisher Scientific cat. no. 13-689-8)
- Omnifix Luer-lock syringes (20ml) (BBraun cat. no. 4616200V)
- Needles (0.5x16 mm/25G) (Gima cat. no. 23760)
- Butterfly needles 23G and 25G (needle: 20mm, 0.6/0.4mm; tube: 300mm, 0.36ml) (Ospedalia AG)
- Infusion pump (Harvard Apparatus Pump 11 Elite, Instech Laboratories Inc)
- Dissecting instruments: gross/fine dissection scissors (Aichele Medico AG)
- Dissection tray with corkboard (Shandon, Thermo Fisher Scientific)
- Pinning needles (1.2x40 mm/18G) (BBraun)
- Beaker cups (120ml/160ml) (Semadeni cat. no. 2294 or 4438)
- Pipette with pipette-tips (10ml) (Soccorex cat. no. 312.10)
- Wheaton scintillation vials (20ml) (Fisher Scientific cat. no. 03-340-25N)
- Vacuum pump (Laboport N820, KNF Group)
- Lyophilization Machine (benchtop freeze dry system, Labconco)
- Scanning Electron Microscopy specimen stubs (Agar Scientific, cat. no. AGG301)

- Light microscope (Axiolab 5, Zeiss). We use conventional light microscopes for quality control of vascular corrosion casts.
- Fluorescence microscope (Olympus, BX-UCB)
- Scanning Electron Microscope (Hitachi S4000), see Equipment Setup
- Gold sputter / coater device (Agar Scientific)
- Desktop µCT (µCT 40, Scanco Medical AG) , see Equipment Setup. Similar instruments from other manufacturers can be used as well.
- Synchrotron Radiation µCT. We used the TOMCAT beamline of the Swiss Light Source, see Equipment Setup. Similar experimental setups are available in most synchrotron facilities, and imaging settings should be selected according to the available instrumentation.

REAGENT SETUP

FA solution (4%, wt/vol in 0.1M PBS): Under a chemical fume hood, prepare 0.1M phosphate buffer (PB) (pH = 7.4) by adding 19 ml 0.2M NaH_2PO_4 x H_2O (27.58g/l) to 81ml Na_2HPO_4 (28.38 g/l). Next, add 8 g of paraformaldehyde (PFA) powder to 100 ml distilled water (aqua millipore). Dissolve the PFA powder by heating the solution (containing a clean magnetic stir bar) to 60 °C on a magnetic stirrer. To facilitate dissolving the PFA powder, add few drops of 5 or 10M NaOH when mixing starts. After PFA powder dissolved completely, filter the PFA solution using filter paper. To dilute the 8% (wt/vol) FA solution to the final concentration of 4% (wt/vol) PFA in 0.1M PB, add 100 ml of 0.2M PB. When the solution has cooled down to room temperature (18-23°C), check the pH and adjust to pH 7.4 if necessary. Aliquots can be stored at -20°C for up to 1 year[35,141], however, we recommend to freshly prepare the 4% (wt/vol) PFA solution for every experiment. Thaw the aliquots in a warm water bath (35-40°C) and cool them to 4°C on ice before use.

Artificial Cerebrospinal Fluid (ACSF) (with 24KU Heparin Sodium Salt): Under a chemical fume hood, mix NaCl (7.6 g/l), $NaHCO_3$ (2.02 g/l), Glucose, $MgSO_4$ x $7H_2O$ (0.37 g/l), KCl (0.26 g/l), NaH_2PO_4 x H_2O (0.17 g/l) (water-free 0.15 g/l), $CaCl_2$ x $2H_2O$ (0.29 g/l) (must be added last). Add 25KU Heparin Sodium salt per liter. If you prepare it one day in advance, store the solution at 4°C. Should be stored for no longer than 4 weeks[168]. Before use, warm up to 37°C in a water bath.

Resin (PU4ii): Dilute 5-10 mg of pigment into 3 g of ethylmethylketone (EMK). Then add the EMK/pigment mixture to 5g of PU4ii and mix in a glass vial using a vortex mixer. The hardener (0.8 g) should only be added to the resin mixture after infusion of the formaldehyde fixation solution. Mix this final resin mixture using a vortex mixer, briefly evacuated in a standard vacuum chamber to remove remaining air bubbles and then transfer into a 10 ml syringe. The hardener has the shortest shelf-life and should be covered with the dry gas (XTEND-IT®) (see reagent list) after each use. Use the resin mixture immediately after preparation.

EQUIPMENT SETUP

Dissection board: A dissection board placed into a tray is used for the perfusion steps. The board should be slightly tilted to collect the efflux after cardiac infusion.

Scanning electron microscope: We assess the quality of random samples of the corrosion casts before µCT imaging using Hitachi S4000 SEM with backscattering detector. Multiple resolutions and acceleration voltages are used until clear views of the perfused vessels can be attained. The imaging parameters and exact type of SEM are not critical as the images are used only for visual evaluation and pre-screening to eliminate any insufficiently perfused samples.

Desktop µCT system: We use a cone-beam micro-tomograph to create 3D overview images of the whole brain samples and facilitate selection of suitable regions for high-resolution imaging. A Scanco Medical µCT 40 device with a nominal isotropic voxel size of 16µm is used in this protocol. The imaging settings are set to suitable values as recommended by the device manufacturer (e.g. for the system we used, a resolution of <8 µm 10% MTF and a 3-72 µm nominal isotropic voxel size with an image format of 512 x 512 to 4096 x 4096 pixels could be selected). The exact settings are not as critical as the images are not used for quantitative analysis.

Synchrotron Radiation µCT: We acquired high-resolution tomographic images of selected regions of interest at the TOMCAT beamline of the Swiss Light Source. The imaging system was operated at 17.5 keV X-ray energy with a sample-detector distance of 30 mm. For each region of interest, 1001 projections images were acquired with 0.73 µm pixel size and 2 s exposure time. Paganin phase retrieval was used on the projection data, followed by reconstruction with the gridrec algorithm.

PROCEDURE

Perfusion with Resin PU4ii (day 1) ● TIMING ~5–10 min per mouse

1. After weighing, anesthetize mice using 100 mg/kg pentobarbital intraperitoneally. Check proper anesthetic depth before proceeding (if using the tail-pinch method, the mouse must not move anymore). Fix both the postnatal (P10) and adult (P60) animals onto a dissection board (Figure 2c-j, Extended Data Figure 1).

- **CRITICAL STEP** It is crucial to weigh the animals prior to resin perfusion as developmental stages are only comparable between the different study groups for mice with similar weights (and ages) .

! CAUTION All animal experiments must be performed in accordance with governmental, institutional, and ARRIVE guidelines. The procedure we describe here was approved by the Cantonal Veterinary Department of Zurich (license number 173/2010).

2. Test with the tail-pinch method if the mouse is properly anesthetized and turn it on its back.

3. For the surgical preparation, then lift the skin with forceps and cut perpendicular to expose the sternum (Figure 2g,d,g,h, Extended Data Figure 1a).

4. Next, lift the sternum and make lateral cuts through the rib cage to expose the chest cavity. Pull back the cage flap and fix using a pin/needle. Carefully remove the pericardium using rounded forceps (Figure 2d,h, Extended Data Figure 1b).

5. Lift the heart slightly using forceps and then insert butterfly needle (23G butterfly needle for adult mice, needle: 20mm, 0.6/0.4mm; tube: 300mm, 0.36ml, and 25G butterfly needle for P10 mice) into the left ventricle (Figure 2e,i, Extended Data Figure 1c). Note the angle of insertion of around 30°C in the sagittal plane (Figure 2e).

- **CRITICAL STEP:** Do not insert the needle too deep to avoid damage of the atrioventricular valve or puncture of the heart basis. The inserted perfusion needle should be glued to the heart using instant glue to prevent the needle from sliding out during perfusion and leakage of the perfusion fluids. Only a small drop is required.

6. Open the right atrium with a pair of sharp and pointed scissors. Immediately start the perfusion with 20 ml (for adult animals) and 5 ml (for P10 animals) artificial cerebrospinal fluid containing 25,000 U/L Heparin through the left ventricle, then stop the pump, block the tube with a hemostat and exchange the syringe.

- **CRITICAL STEP:** Before reconnecting the syringe, make sure that all air in the tube is completely removed.
- **CRITICAL STEP:** for P10 animals, adapt the amount of ACSF containing 25,000 U/L Heparin according to the animal age.

? TROUBLESHOOTING

7. Start perfusion with 4% (wt/vol) PFA (in PBS). Immediate muscle fasciculation indicates good quality of fixation.

8. Add the hardener (0.8 g) to Resin PU4ii solution (prepared by diluting 5-10 mg of pigment into 3 g of EMK, adding the EMK/pigment mixture to 5g of PU4ii, see Reagent Setup) and mix using a vortex mixer (Figure 2b,f,j, Supplementary Video 1). Briefly evacuate in a standard vacuum chamber to remove remaining air bubbles and then transfer into a 10 ml syringe. When perfusing the Resin solution, tilt the rear of the perfusion pump upwards to prevent occasional air bubbles leaving the syringe. The tray should be tilted to avoid a mess due to the efflux from the atrium.

- **CRITICAL STEP:** The resin perfusion is successful if the mouse turns bluish immediately. This can be particularly well monitored at the paws, snout or tail (Figure 2f,j, Supplementary Video 1).

? TROUBLESHOOTING

Resin curing (days 2-3) ● TIMING ~1 d

9. Keep animals for at least 24 hours at room temperature (18-23°C) without manipulation. The resin curing time does not differ between P10 and P60 animals.

- **CRITICAL STEP:** Do not manipulate the sample during the 24 hours. Otherwise, this may influence the curing and may lead to deformations in the vascular corrosion cast.

10. (**OPTIONAL)** For simultaneous visualization and analysis of both the blood vessel structures and the surrounding soft tissue as well as for co-visualization of vascular and e.g. perivascular cell markers, take selected resin-perfused brains. Make thick, 100-150 µm sections with a vibratome and then stain them with virtually any protein of interest (in our case DAPI for cell nuclei and FluoroMyelin Red (Invitrogen™) for myelin). Image the sections imaged with fluorescence light microscopy (Olympus, BX-UCB) (Extended Data Figure 7). Proceed to the next step to macerate the remaining brains.

Tissue maceration of soft tissue (day 2-3) ● TIMING ~1 d

11. Transfer the animal into 300-400 ml (for P60 animals) 7.5% (wt/vol) KOH and incubate at 50°C for at least 24 hours. Place only one animal into the solution at one time and make sure the entire body is covered.

Decalcification of bony structures (days 3-4) ● TIMING ~1d

12. Incubate the animal in 300-400 ml (for P60 animals) 5% (vol/vol) formic acid at 50°C for at least 24 hours. Place only one animal into the solution at one time and make sure the entire body is covered.

Brain dissection (day 4) TIMING ● ~5 min per cast

13. Free the cerebral vasculature from remaining extra-cranial vessels using fine scissors and forceps (Figure 2k-n). Optionally, the extracranial vessels can also be further processed and analyzed by following a similar procedure to the one described here, depending on the vessels/organs of interest.

- **CRITICAL STEP:** Perform the brain vascular corrosion cast dissection/pruning carefully (Figure 2k-n, Supplementary Video 1) because the vessel cast is mechanically sensitive.

Wash in distilled water (day 4) TIMING ● ~5 min per cast

14. Wash the brain vascular corrosion cast in distilled water. Place only one brain at a time into 15 ml of distilled water.

- **CRITICAL STEP:** Use plenty of distilled water in order to eliminate all residues of tissue and dissected pieces of the extracranial vessels.

Quality control using Scanning Electron Microscopy (SEM) (day 4) TIMING ● ~1 h per cast

15. For routine SEM, mount a small random sample of the brain casts on stubs and sputter-coat them with gold.

Osmification with osmium tetroxide (OsO_4) of brain vascular corrosion cast (day 4) TIMING ● ~24 hours

16. Transfer the brain vascular corrosion casts not used for SEM into 2% (wt/vol) OsO_4 in 5 ml water at room temperature and incubate for 24 hours to increase absorption contrast, and reduce CNR during the SRμCT imaging.

!CAUTION: OsO_4 is very toxic. Work under a fume hood and use protection gloves, glasses and lab coat. Properly dispose the OsO_4 waste.

Wash in distilled water (days 4-5) TIMING ● ~5 min per cast

17. Wash the brain vascular corrosion cast thoroughly in distilled water. Place only one brain at a time into 15 ml of distilled water.

- **CRITICAL STEP:** Use plenty of distilled water in order to eliminate all residues.

Lyophilization by freeze-drying (days 4-5) TIMING ● ~ 24 hours per cast

18. Dry the brain vascular corrosion casts by freeze-drying in a lyophilization machine overnight at -54°C in a vacuum.

Mounting on plexiglas stubs (days 5-6) TIMING ● ~5 min per cast

19. Mount each brain resin cast using cyanoacrylate glue on plexiglas stubs (size of the stubs is dependent on the μCT set-up and brand) equipped with stainless steel pins for sample

repositioning in the µCT. **!PAUSE POINT:** The brain vascular corrosion casts can be stored at room temperature (for years) before continuing with the imaging steps of the protocol.

Scanning electron microscopy (days 5-6) TIMING ● ~15 min per cast

20. Evaluate all corrosion casts by light microscopy, and then analyze the subset of corrosion casts selected and prepared in step 15 with SEM as quality control. Corrosion casts are suitable for further analysis if a dense vascular network without holes or irregularities is present and there are endothelial cell nuclei imprints on large vessel casts (Extended Data Figure 2, Supplementary Figure 1).

Desktop µCT imaging (day 6) TIMING ● ~15 min per cast

21. Acquire 3D images of whole-brain samples not used for SEM using a desktop µCT system by selecting the various imaging parameters according to manufacturer's instructions (or optionally using a SRµCT scanner, see "Experimental Design – Alternatives for wider accessibility"). We use a µCT 40, Scanco Medical AG setup, operated at 50 kVp and 160 µA with a nominal isotropic voxel size of 16µm. Per scan, we acquire 1000 projection images with an integration time of 200 ms and an additional three times frame averaging for improved SNR. The exact settings depend on the desktop µCT system used.

Selection of the regions of interest (ROIs) (day 6) TIMING ● ~15 min per cast

CRITICAL This step is not needed if the entire brain cast is scanned in high resolution in Steps 23-24.

22. Reconstruct, segment and import tomographic images into custom-made or existing ROI picker software (here, we used the Imaging Processing Language of Scanco Medical, http://www.scanco.ch/, for details we refer to[169]). Place one to three ROIs of 1 mm^3 per animal

and brain region in the cerebral cortex, hippocampus, superior colliculus and brain stem (Figure 4a-l). Then calculate relative coordinates of ROIs with respect to the two-sample holder pins and save them for subsequent re-orientation and measurement at the synchrotron beamline.

High-resolution SR-μCT imaging of selected ROIs or the entire brain vascular corrosion cast (days 6-7) TIMING ● ~30 min per cast (~24 h for scanning one entire brain vascular corrosion cast).

23. Acquire high-resolution 3D images of selected ROIs or the whole brain using the tomography setup established for the Synchrotron Radiation μCT system being used. We use a previously described local tomography setup detailed in refs[39,100,104]. Briefly, the system we use operates at 17.5 keV with a sample-detector distance of 30 mm for distinct edge enhancement, and an optical magnification resulting in an isotropic voxel size of 0.73 μm. Each measurement includes 2000 projections acquired at an integration time of 0.1 s each. Phase-retrieval is performed with the Paganin method and data reconstructed using the gridrec algorithm. The net volume of the final images is 2560 × 2560 × 2160 voxels, corresponding to 5.5 mm^3 of tissue volume.

24. When the entire brain vascular corrosion cast is scanned in high resolution (as compared to the high-resolution scanning of pre-selected ROIs), the mosaic images should be stitched together. To construct an artifact-free image mosaic from the sub-images, we use a non-rigid stitching approach, according to[159]. This image mosaic can then be registered to the Allen Mouse Brain Atlas (http://developingmouse.brain-map.org/docs/Overview.pdf) or – alternatively – to any other Mouse Brain Atlas and divided into segments. We divide the anatomical structures of interest into segments with the exact same dimensions as the previously used ROIs (in the ROI-based approach), in order to proceed with a similar analysis process.

Computational 3D reconstruction of the 3D vascular network – vessel segmentation (day 8-9) TIMING ● ~15 min per ROI (~10h for one whole brain scan, depending on the technical settings)

25. If the reconstructed CT images are noisy, apply bilateral filtering in order to improve the signal-to-noise ratio. This step is not required if the SNR is high. In order to separate vessels from the background in the reconstructed CT images, use the Otsu thresholding method[160] (Figure 4m-p).

26. Erase small gaps and holes in vessels by performing morphological closing with a spherical structuring element (with a suggested radius of 1-3 voxels).

27. Perform a hole filling operation that merges isolated background regions into the foreground.

28. Calculate the distance map of the segmented vessels, where each vessel voxel is assigned the distance to the nearest background pixel.

29. Calculate the skeleton of the segmented vessels, where each vessel is reduced into a one-voxel wide centerline (Figure 4o).

30. Trace the centerlines into a graph where graph nodes represent bifurcation points and graph edges represent vessels. For each edge, store a list of locations of voxels that form the edge. Store also the distance map value at each edge voxel as it describes the local radius of the vessel at that pixel (Figure 4o).

31. Use anchored convolution to smooth the voxel list of each edge (suggested sigma = 1.125 μm, maximal displacement = 0.5 μm). Do not allow any displacement in the ends of the edge.

32. Calculate the length of each edge by summing distances between consecutive smoothed edge voxels.

33. Remove all isolated branches whose length is small, suggested threshold length = 5 μm.

34. Remove all branches that have one free end and that satisfy $L < 2 \max(r_i, r_2)$ where L is the length of the branch, and r_i are the radii at the endpoints of the branch.

35. Remove all nodes that have exactly two edges connected to them (these might have been created in step 34) and combine the two branches into one.

36. Remove all nodes that have no edges connected to them.

Global vascular network morphometry and local vascular network topological analysis (day 10) TIMING ● ~variable (depending on the parameters to analyze)

37. Categorize vessels and branch points into capillary (diameter < 7µm), non-capillary (diameter ≥ 7µm) and global (without distinction by diameter). Global is the union of capillaries and non-capillaries.

38. Calculate the degree of each branch point. Count the number of branch points per degree, for capillary, non-capillary and global branch points. Use this to plot branch point degree statistics (Supplementary Figures 9-11).

39. Take the values per branchpoint degree (from Step 38) and divide them by network volume. Notice that the tomographic image that the graph is based on is usually cylindrical and the volume of the cylinder should be used. Use this to plot branch point density statistics (Figures 8c,f-h, Extended Data Figure 5,6). The branch point density per volume is defined as the number of branch points per cubic millimeter.

40. Use the branch point diameter (from Step 37), classified into global, capillary, and non-capillary, to plot branch point diameter statistics (Figure 8c, Extended Data Figures 5b,6b).

41. Classify segments into global, capillary, and non-capillary. Count all occurrences per classification. Divide by network volume to get the segment density. Use this to plot segment density statistics (Figure 8c,f-h, Extended Data Figure 5,6, Supplementary Figure 7a-c,9-11).

42. Take segment diameter, and -length per classification (from Step 41), to plot segment diameter, and -length statistics (Figure 9c,g-n, Supplementary Figure 7d-i).

43 Use the values from step 42 and relate length to diameter to plot their relation (Figure 9c).

44. Use the values from step 42 and calculate the volume of the segment as the sum of volumes of cylinders corresponding to line segments in that segment. Use this to plot segment volume statistics (Figure 10e-h, Supplementary Figure 7m-o).

45. Calculate vessel tortuosity of each vessel segment as the ratio between the effective length/distance between the endpoints of a vessel segment and the shortest length/distance between those vessel segment endpoints. Use this to plot the vessel tortuosity statistics (Figure 10a-d, Supplementary Figure 7j-l).

46. Use the image containing the segmented vessels and calculate the Euclidean distance transform of non-vessel regions. This creates a volume containing the distance to the closest vessel for each non-vessel voxel. Create a histogram of the distance values to estimate the extravascular distance distribution (Figure 11b,i-k, Supplementary Figure 5).

47. Count the number of background and vessel voxels. Calculate vascular volume fraction (volume fraction of all vessels) as the ratio between number of vessel voxels and total number of voxels. (Figures 5h-j,7f-h, Supplementary Figures 2-5).

48. Calculate the sum of all segment volumes for global, capillary, and non-capillary segments. Divide the capillary volume by the global volume. Use this value to scale the volume fraction calculated in step 47 to get the approximate capillary volume fraction. Do the same for non-capillaries. Use these values to plot the capillary and non-capillary vascular volume fraction statistics (Figures 7f-h, Supplementary Figures 2-5).

49. Derive the vessel directionality by attributing every vessel to its main direction (x, y, z) in the 3D space within the selected ROI. For each line of each segment, normalize the vector that represents the line. To quantify the directions of vessels emanating from each branchpoint, calculate the relative angles between all segments that join at a branch point. This allows for a quantitative representation of how orthogonal (90°) or straight (0° and 180° ranges) vessels go in and out of branchpoints. This normalized direction (x,y,z) is directly mapped to “redness” (r), “blueness (b), and “greenness” (g) (r,g,b), and then scaled by 1.75 to get a better color

saturation and clamped to [0,1]. Render the computational 3D reconstructions with color mapped to 1) directionality, 2) vessel radius, and 3) classification (capillary or non-capillary) of each vessel (Figure 12, Supplementary Figures 12-16).

Statistical analysis (day 11) TIMING ● ~variable (depending on the parameters to analyze).

50. Compare the mean of the parameters of each ROI obtained from the different sample groups using the Welch t-test (statistically significant differences are defined as P-values below 0.05). Use Matplotlib (https://matplotlib.org) and NumPy (https://numpy.org) or comparable software to visualize the data with histograms and boxplots.

! CRITICAL STEP In our example for the whole-brain scan method, the mean of the parameters obtained from one animal in the different groups (P10 WT, P60 WT) were also compared using the Welch t-test. Histograms and boxplot to visualize the data (Figure 13, Supplementary Figures 17-21), as well as statistical testing and figure plotting were performed in the exact same manner as described for the ROI-based method.

TIMING

Steps 1-8, animal perfusion with resin PU4ii (day 1): ~5–10 min per mouse

Steps 9, resin curing (days 2-3): 1 d

Step 10, immunofluorescence staining (optional step, days 2-3): 2 d

Step 11, tissue maceration of soft tissue (days 2-3): 1 d

Steps 12, decalcification of bony structures (days 3-4): 1 d

Steps 13, brain dissection (day 4): ~5 min per cast

Steps 14, wash in distilled water (day 4): ~5 min per cast

Steps 15, gold-sputtering for SEM (quality control) (day 4): ~1 h per cast

Step 16, osmification with osmium tetroxide (day 4): ~24 h

Step 17, wash in distilled water (days 4-5): ~5 min per cast

Step 18, lyophilization by freeze drying (days 4-5): 24 h per cast

Step 19, mounting on plexiglas stubs (days 5-6): ~5 min per cast

Step 20, SEM imaging (quality control) (days 5-6): ~15 min per cast

Step 21, desktop μCT imaging (day 6): ~15 min per cast

Step 23, selection of the regions of interest (day 6): ~15 min per cast

Steps 23-24, high-resolution SRμCT imaging of selected ROIs or the whole brain (days 6-7): ~30 min per cast (~10-24 h for one whole brain scan, depending on the technical settings)

Steps 25-36 (days 8-9), computational reconstruction of the 3D vascular network – vessel segmentation: ~15 min per ROI (~10 h for one whole brain scan, depending on the technical settings)

Steps 37-49 (day 10), global vascular network morphometry and local vascular network topological analysis: ~variable (depending on the parameters to analyze)

Step 50 (day 11), statistical analysis: ~variable (depending on the parameters to analyze)

TROUBLESHOOTING

Troubleshooting guidance can be found in Table 1.

Table 1. Troubleshooting Table

Step	Problem	Possible reasons	Possible solution
6-8	Air bubbles in the ACSF containing heparin, in the 4% PFA, or in the resin solutions that can lead to incomplete perfusion through interruption of flow and/or to rupture of the vessel wall.	Air was trapped in the syringe while filling it with ACSF containing heparin, the 4% PFA, or the resin. Air bubbles are difficult to see in the ACSF containing heparin, in the 4% PFA, or the resin solutions.	Look under a strong light source and remove any air bubble(s) from the syringe. Tilt syringe forward and let air bubble accumulate at the stopper. Stop injection before air enters the tubing.
8	Animal does not become bluish immediately.	Resin leaks out or flows retrogradely into the lung due to mitral valve damage.	Check for leakage between needle and ventricle wall. If leakage is detected, stop infusion and try sealing the leakage using instant glue. In case of retrograde perfusion of the lung exclude animal. Puncture left ventricle very carefully.

8	Animal does not become blue immediately, and the ACSF containing Heparin, the 4% PFA, or the resin solution comes out of the nose (the respective solution went into the lungs because of damage of lung blood vessels due to retrograde perfusion caused by injury to the mitral valve during needle puncture of the left ventricle).	Injury of the mitral valve due to needle puncture while puncturing the left ventricle.	Low chance of obtaining complete perfusion of tissue and organs. Animal needs to be excluded. Inject/infuse a new animal. Puncture the left ventricle very carefully and inject/infuse very carefully.

ANTICIPATED RESULTS

With the protocol described here, perfused blood vessels of the total vascular network can be quantitatively assessed in any desired mouse brain region, starting from the postnatal (at least as early as P10) to the adult stage by analyzing various vessel parameters such as vascular volume fraction, branch point density and -degree, segment density, -diameter, -length, -tortuosity, -volume, -directionality, and the extravascular distance. Here we present examples of the types of data that can be obtained using this protocol. The vascular volume fraction, the vessel segment-, and branch point density in various brain regions including cortex, hippocampus, and superior colliculus are significantly increased in the adult (P60) as compared to the postnatal (P10) mouse brain (Figures 5h-j,7a-c,f-h,8f-h, Extended Data Figures 5e-g,6e-g), indicating active sprouting angiogenesis and vascular network formation from the developing postnatal- to the mature adult stage of mouse brain development.

Application of the existing protocol to the postnatal mouse brain vasculature

The 3D vasculature of mice during postnatal brain development and at the adult stage is visible in the polyurethane resin PU4ii- perfused P10 WT and P60 WT mice (Extended Data Figure 2). Light microscopy and SEM of brain tissue samples from resin-perfused P10 and P60 WT mice reveals a dense vascular network in the superficial cortex with well-defined vessel structures of all sizes (Extended Data Figure 2). During resin perfusion, endothelial cell nuclei

are exposed to the passing resin material, resulting in imprints of blood vessels on the cast surface (Extended Data Figure 2f), which were observed in vascular corrosion casts of both P10 and P60 mice, demonstrating the perfect molding of the vascular lumen[106]. Moreover, the fine capillary network was well defined and visible and devoid of vessel interruptions in both the P10 and the P60 brain cortices (Extended Data Figure 2). All these morphological features are in line with the characteristics of the normal cerebral vasculature in postnatal adult mice that we and others have previously published[39,100,105]. The raw images of the SRμCT of the vascular corrosion casts, that were the basis for subsequent computer-aided 3D-reconstruction (Figure 5a), showed very high quality (Figures 4m,n,5a-d, Supplementary Video 2). These typical results further confirm that the vascular corrosion casting technique is an excellent method to visualize the 3D vessel network architecture in the brains of both P60 and also developing P10 mice. This results demonstrate that by making the minor adaptations discussed here, vascular corrosion casting can be applied in very young and small mice at the stage of postnatal brain development at which vascular sprouting is highly active[2,3,24,37,38,75].

Functional, perfused blood vessels that constitute the 3D brain vascular network can be best visualized with a marker that is perfused into the circulation of an intact mouse. We therefore used polyurethane resin PU4ii as this labels the inner vascular lumen of actively, *in vivo*–perfused blood vessels (Figure 2k-n, 3). Resin PU4ii-perfused blood vessels and in consequence, the entire 3D brain vascular network can be imaged and computationally analyzed in both postnatal and adult mouse brains (Figures 5-14), allowing the development of the vascular network to be compared between two developmental stages.

As an additional validation step, vascular corrosion casting can be combined with immunofluorescent or other stainings which may ease navigation within the vascular network, and allows direct correlation with molecules or cell structures of interest (Extended Data Figure 7), e.g. perivascular cells of the neurovascular unit such as pericytes, astrocytes, or neurons.

We recommend using additional labelling with other markers such as DAPI to label cell nuclei when using markers for any other cell or protein of interest (Extended Data Figure 7).

Hierarchical 3D imaging of the postnatal and adult mouse brain vasculature – global vascular network morphometry and local vascular network topology

Perfused blood vessels were hierarchically imaged by SRμCT and subsequently computationally analyzed and quantified by an image analysis pipeline (Figure 4m-p,5a-d,6a-d). Various vessel parameters (see above) of PU4ii resin-perfused vessels, as well as the extravascular distance, can be quantified using computational analysis consisting of either global vascular network morphometry analysis or local topological vascular network analysis[39,141,160,164-166].

Global vascular network morphometry

Global vascular network morphometry allows quantification of properties of each dataset without considering the form- and shape properties of individual vascular structures, generating an abstract quantification of the data (Figures 5,7-9). The typical results we present here demonstrated that in the P10 WT animals, between 1.67% in the cortex, 1.93% in the superior colliculus, and 2.14% in the hippocampus of the total volume of the postnatal mouse brain tissue was occupied by perfused vessel structures, and this percentage was between 2.58% in the cortex, 2.81% in the superior colliculus, and 2.97% in the hippocampus of the total volume of the adult mouse brain tissue. This data is in accordance with previous findings by our[28,39,104] and other groups[22,25]. In the P60 WT mouse brain, the vascular volume fraction was significantly increased as compared with P10 WT animals in the cortex (P60 WT vs. P10 WT (mean ±SD; applies also for all subsequent values): 2.58 ±0.77% vs. 1.67 ±0.45%, P = 0.0032), hippocampus (P60 WT vs. P10 WT: 2.97 ±0.70% vs. 2.14 ±0.22%, P = 0.019), and superior colliculus (P60 WT vs. P10 WT: 2.81 ±1.15% vs. 1.93 ±0.26%, P = 0.048) (Figure 5h-j). The

increase of the vascular volume fraction of perfused vessels between the two developmental stages P10 and P60 was between 39% and 54% (+54% in cortex, +39% in hippocampus, +45% in superior colliculus), in line what we observed previously using stereological methods[38]. This demonstrates that postnatal and adult mouse brain vasculatures can be compared using this protocol at the network level.

To illustrate the sensitivity and broad applicability of the proposed method, we used a knockout mouse model of the well-known anti-angiogenic molecule Nogo-A (Nogo-A$^{-/-}$)[28,38,39,170-172], at both the developing P10 as well as at the P60 stages. Interestingly, the increase in vascular volume fraction in the P10 Nogo-A$^{-/-}$ as compared to the P10 WT was similar to the comparison between the P60 WT and the P10 WT mice in all brain regions, whereas these effects were no longer visible between P60 Nogo-A$^{-/-}$ and P60 WT mice (Supplementary Figure 5), indicating i) a hypervascularization/accelerated vascularization in the Nogo-A$^{-/-}$ mice during postnatal brain development, and ii) that these effects are compensated/strongly attenuated in the adulthood[38], in agreement with what we previously showed[38,39]. Given the redundancy of mechanisms acting on the vascular system, effects of genetic deletion of angiogenic/anti-angiogenic molecules on angiogenesis and the vasculature network that are observed during embryonic or postnatal development are often compensated at the adult stage, and this is also the case for the Nogo-A$^{-/-}$ mouse[38,39] (Supplementary Figures 5-8).

Local vascular network topology

In contrast to global vascular morphometry, local vascular network topology analyzes each individual vascular structure and bifurcation point separately, thereby allowing quantification of the form and shape of the vascular network (Figure 6a-d). The vessel-specific properties of each individual vascular structure (= each vessel segment) and each bifurcation point within the dataset thereby affects the quantification and analysis of the 3D vascular network and local topological analysis of the 3D vascular network allows the characterization of individual per-

vessel parameters such as segment density, -diameter, -length, -tortuosity, -volume, and branch point density and -degree (Figures 6-10). Importantly, local topological analysis allows differentiation between capillary (< 7 µm in diameter) and non-capillary vessels (≥ 7 µm in diameter) of the highly interwoven hierarchical 3D vessel/capillary network (Figures 6,7)[21,173]. For quantitative assessment of angiogenic features such as branch point density and -degree, segment density, -diameter, -length, -tortuosity, -volume and vascular branch points, we therefore referred to local topological vessel analysis provided by a computational image analysis pipeline (Figures 6-10, PROCEDURE steps 24-48). Examples of the quantification of the aforementioned vessel parameters in different regions of the postnatal- and adult mouse brains are shown in Figures 5h-j,7a-c,f-h,8c,f-h,9c-n,10a-h, Extended Data Figures 5b,e-g,6b,e-g). The absolute values for the vascular volume fraction are in accordance with previous findings by our group using immunofluorescent staining and stereological analysis[28,38] and with studies using similar[100,104] or different 3D methods[22,174].

Distinction of capillaries and non-capillaries

Based on the distinction between capillaries and non-capillaries, there is a very important significant increase in the density of capillary blood vessels (as revealed by the vascular volume fraction) between the developing postnatal- and the mature adult mouse brain vascular network (Figure 5h, Supplementary Figures 2-5), whereas the non-capillary blood vessels showed only a non-significant increase between these two time points, in various brain regions (Figure 7g, Supplementary Figures 2-5). Local vascular network topology revealed that the 3D vascular volume fraction in the P60 WT cortex was increased by 54% as compared to the P10 WT cortex (Figure 7f), and by 39% and 45% in the hippocampus (Supplementary Figure 3c) and superior colliculus (Supplementary Figure 4c), respectively, and these values were all similar to the fold change calculated by global vascular morphometry (Figure 5h,i,j). Deeper insight into the 3D

vascular network architecture is provided by addressing specific properties of each individual vessel structure, for instance by addressing the vessel diameter (Figures 5-7).

Accordingly, of the total vessel tissue volume (= vascular volume fraction) of 1.67% in the P10 cortex, 1.24% (74,2% of the total vessel volume) was occupied by non-capillary vessels (Figure 7g) and 0.43% (25.8% of the total vessel volume) by capillaries (Figure 7h). Values for the hippocampus and superior colliculus can be found in Supplementary Figures 3,4.

Increase in capillary density from the postnatal to the adult stage

Adult (P60) WT animals showed an increased absolute frequency of capillaries as compared to P10 WT animals throughout the different brain regions, whereas the absolute frequency of bigger vessels was very similar between the two developmental stages (Figure 7f-h). Computational 3D analysis revealed that the increased vascular volume fraction in the cortices, hippocampi, and superior colliculi of P60 WT animals was mainly due to a significant increase in the vascular volume fraction at the capillary level (cortex: P60 WT vs. P10 WT: 1.16 ±0.37% vs. 0.43 ±0.22, P = 5.8×10^{-6}) whereas a slight increase of the vascular volume fraction of larger vessels (cortex: non-capillaries, P60 WT vs. P10 WT: 1.42 ±0.56% vs. 1.24 ±0.37%, P = 0.41) did not reach statistical significance (Figure 7f-h, see Supplementary Figures 3,4 for hippocampus and superior colliculus). Quantitatively, the vascular volume fraction was increased by 169% for capillaries and by 14% for non-capillaries in the cortex (Figure 7f-h, see Supplementary Figures 3,4 for hippocampus and superior colliculus). Taken together, these results indicate that the increased vascular volume fraction observed from the postnatal to the adult stage is mainly due to additionally formed capillaries whilst the number of larger non-capillaries remains relatively unaffected.

Increase of vascular branching of capillary microvessels from the postnatal to the adult stage

The observed increased vascular volume fraction may be due to increased vessel branching and concomitant newly formed vessel segments or caused by an increased vessel diameter, by an increased vessel length, or a combination of these factors. To illustrate that this protocol allows addressing the origin of the additionally formed vessels, the number of vascular branch points in the cortices of P10 WT and P60 WT animals referring to local topological analysis was determined (Figure 8). Vessel branch points are characterized by their degree[104], defined as the number of vessels adjacent to a vessel branch point, usually ranging from degree 3 to degree 5[175] (Figure 8b). Accordingly, vascular branch points were defined as points where three (branch point degree 3), four (branch point degree 4), or five (branch point degree 5) vessel segments converge (Figure 8b). For discrimination between "capillary branch points" and "non-capillary branch points," the branch point diameter was considered to be that of the thickest vessel adjacent to a given branch point (Figure 8b). Accordingly, if the thickest vessel adjacent to a given branch point was < 7 μm, the branch point was classified as a "capillary branch point," whereas if the thickest vessel adjacent to a given branch point was ≥ 7 μm, the branch point was classified as a "non-capillary branch point". Adult (P60) WT animals showed a pronounced increase of branch point density (of all degrees) at the capillary level (P60 WT vs. P10 WT: 13994.1 ±7395.6mm^{-3} vs. 1929.1 ±819.1mm^{-3}, $P = 5.3 \times 10^{-5}$) and a slighter increase of the number of branch points for non-capillaries (P60 WT vs. P10 WT: 2959.9 ±1559.7mm^{-3} vs. 1993.3 ±683.7mm^{-3}, P = 0.10) as compared to the P10 WT mice in the cortex, as well as in the hippocampus, and superior colliculus (Figure 8c,f-h, Extended Data Figure 5b,e-g). Computational reconstructions revealed an increased number of vessel branch points in cortices, hippocampus, and superior colliculi of P60 WT animals as compared with P10 WT mice (Figure 8d,e, Extended Data Figures 5c,d,6c,d). Quantitatively, the density of branch points for all vessels in the cortex was significantly – by 332%, 230%, 435%, respectively – increased (cortex: P60 WT vs. P10 WT: 16954.0 ±8329.6mm^{-3} vs. 3922.4 ±1376.9mm^{-3}, $P = 9.6 \times 10^{-5}$) in adult (P60) WT as compared to postnatal (P10) WT animals (Figure 8d,f-h, see

Extended Data Figures 5e-g,6e-g for hippocampus and superior colliculus), predominantly due to a more than seven fold increased (+625%) number of branch points in the capillary bed in the cortex (cortex: P60 WT vs. P10 WT: 13994.1 ±7395.6mm^{-3} vs. 1929.1 ±819.1mm^{-3}, P $=5.3 \times 10^{-5}$) (Figure 8d,f-h, see Extended Data Figures 5e-g,6e-g for hippocampus and superior colliculus). Interestingly, in the adult animals, this was mainly due to an increased number of vessel branch points of degree 4 for all vessel sizes (cortex: +839% for all vessels, P60 WT vs. P10 WT: 1769.4 ±1047.0mm^{-3} vs. 188.4 ±62.2mm^{-3}, P = 0.00015, +182% for non-capillaries, and +1345% for capillaries) (Supplementary Figure 9h-j, and see Supplementary Figures 9h-j,10h-j, for hippocampus and superior colliculus), while showing a highly significant increase also for vessel branch points of degree 3 for all vessel sizes (cortex: +304% for all vessels, +42% for non-capillaries, and +578% for capillaries) (Supplementary Figures 9e-g, and see Supplementary Figures 9e-g,10e-g, for hippocampus and superior colliculus), indicating both formation of new vessel branch points (degree 3) and further branching of existing degree 3 branch points (degree 4). Vessel branch points of degree 5 were not detected in either study group (Supplementary Figures 7-9). Moreover, the mean vessel branch point degree for the different vessel sizes showed an overall increase between the two developmental stages (cortex: +2% for all vessels, +1% for non-capillaries, and +2% for capillaries; hippocampus: +2% for all vessels, +2% for non-capillaries, and +2% for capillaries; superior colliculus: +3% for all vessels, +2% for non-capillaries, and +3% for capillaries) (Supplementary Figures 7-9), indicating that branch point degree increases during physiological vascular brain development. Together, these data reveal that the enhanced vascular volume density observed from the postnatal to the adult stage can be mainly explained by an increased number of vascular branch points mainly at the level of capillaries.

Interestingly, we observed a significant increase (+39%** for all vessels) for the vascular volume fraction (again mainly at the level of capillaries, +71%**) when comparing data on the cortex of P10 Nogo-A$^{-/-}$ with P10 WT mice, and these effects were reminiscent of the

comparison between P10 WT and P60 WT mice mentioned above (Supplementary Figure 5). At the adult stage, however, the effect of genetic deletion of Nogo-A did not show significant differences in the brain vasculature between the WT and Nogo-A$^{-/-}$ groups, suggesting that the inhibitory effect of Nogo-A on sprouting angiogenesis is compensated by the redundancy of mechanisms acting on the vascular system during these later stages of cerebrovascular development[38].

Both the effects of the developmental stage (e.g. adult P60 versus developing P10) as well as the effect of deletion of the Nogo-A gene at the postnatal (but not adult) stage were consistent throughout various brain regions (Figures 5-12, Extended Data Figures 5,6, Supplementary Figures 2-16).

Morphological changes (segment density, -diameter, -length, - tortuosity, and extravascular distance) in the three-dimensional vascular network from the postnatal to the adult stage

In addition to these measured values, this protocol allows the quantification of parameters such as the average segment density (Figure 9d-f, Supplementary Figure 7a-c), -diameter (Figure 9g-j, Supplementary Figure 7d-f), -length (Figure 9k-n, Supplementary Figure 7g-i), -tortuosity (Figure 10a-d, Supplementary Figure 7j-l), -volume (Figure 10e-h, Supplementary Figure 7m-o), and the average maximal perfusion distance (Figure 11, Supplementary Figure 8). Given the high angiogenic activity in the postnatal rodent brain[28,37], the precise values of the aforementioned parameters will obviously depend on the exact developmental stage of the mouse.

The functional consequences of the increased vascular volume fraction in the P60 (and the Nogo-A knock-out animals), can be addressed by determining the extravascular distance – defined as the shortest distance of any given extravascular voxel in the tissue to the nearest vessel structure (Figure 11, Supplementary Figure 8) – which measures the diffusion distance.

The extravascular distance in P10 WT cortices was 31.9 µm on average and thus similar to our previous work[39,175], whereas the P10 WT hippocampus and P10 WT superior colliculus showed lower average values of 18.4 µm and 19.2 µm, respectively (Figure 11i-k, Supplementary Figure 8). Overall, the extravascular distance was markedly reduced in P60 WT mice as compared to P10 WT cortices, hippocampi, and superior colliculi (Figure 11i-k, Supplementary Figure 8). Accordingly, histogram distribution analysis revealed a marked shift towards smaller extravascular distances in the P60 animals (Figure 11i-k, Supplementary Figure 8), which is a consequence of the higher vascular volume fractions observed in the P60 as compared to the P10 WT animals. Quantitative analysis showed a highly significant reduction of the extravascular distance in P60 WT animals to almost half (−45%) as compared to P10 WT mice in the cortex, (P60 WT vs. P10 WT: 17.42 ±6.52 µm vs. 31.94 ±10.63 µm, P $=1.6 \times 10^{-5}$, Figure 11i), with similar findings in the hippocampus (Figure 11j), and superior colliculus (Figure 11k). Although we are aware that the EVD reflects the distance from any given extravascular voxel within the tissue to the nearest vascular structure. this absolute value of 17.42 µm (P60 WT) is comparable with a study by Tsai et al. [22], which, using automated histological imaging and analysis tools simultaneously mapping the locations of all neuronal and non-neuronal nuclei and centerlines of the entire vasculature within slabs of mice adult mice neocortex, found that each individual neuron is no more than 15 µm away from the closest microcapillary, thereby assuring proper oxygen delivery[22].

In line with the findings presented above, the extravascular distance was also reduced in the P10 Nogo-A$^{-/-}$ animals as compared to the P10 WT animals in the different regions, and the effects observed were similar to the comparison between P60 WT mice and P10 WT mice (Supplementary Figure 8).

Together, these data suggest that as the 3D vascular network undergoes significant changes (e.g. increased vascular volume fraction and increased vessel branching) from the developing

P10 to the P60 mature stage, these results in a markedly lowered vessel spacing and diffusion distance throughout various brain regions.

Vessel directionality as a novel parameter in the postnatal and adult mouse brain

Further, this protocol illustrates the ability to derive the parameter vessel directionality by determining for every vessel segment its main angle to the x-, y-, and z-axis in the 3D space within the selected ROIs (Figure 12, Supplementary Figures 12-16) and observed different patterns of vessel directionality throughout the different brain regions examined. Most notably, in the cortex, the superficial PNVP extended in the x- and y-directions, whereas the INVP exhibited a radial sprouting pattern into the brain parenchyma along the z-axis, perpendicular to the PNVP (Figures 12b,c), in accordance with literature[28,33,127]. The distinction between non-capillaries and capillaries revealed that the PNVP and INVP were mainly composed of non-capillary vessels (Supplementary Figures 12-15), and that non-capillaries also formed the base of vessel sprouts emanating from the INVP (and to a lesser extent from the PNVP) mainly in the x- and y-directions (Supplementary Figures 12-15). Capillaries, on the other hand, vascularized the cortical CNS parenchyma via sprouting from non-capillaries and extended equally in all directions (x-,y-,z-), thereby assuring adequate micro vascularization and perfusion of the brain (Supplementary Figures 12-15). At the adult stage, these patterns of vessel directionality observed at the postnatal developing stage were confirmed and further strengthened (Figure 12c, and Supplementary Figure 12-15). Region-dependent variations and region-specific properties in vessel directionality were observed in the hippocampus and superior colliculus (Supplementary Figure 12).

Quantitative analysis of the relative angles of the vascular segments emanating from a certain branch point revealed that the capillaries in the cortex, hippocampus, and superior colliculus derived at angles between around 75° and 150° at both the developing P10 and mature P60 stages (Figure 12d-f, Supplementary Figure 12c-e,h-j). The non-capillaries, however, showed

two main angles of orientation, namely around 90° and at around 170° in three brain regions examined (Figure 12d-f, Supplementary Figures 12c-e,h-j). Interestingly, these two main angles of orientation were more pronounced at the adult P60 as compared to the P10 stage (Figure 12d-f, Supplementary Figures 12c-e,h-j), indicating some sort of preferred vessel orientation of the larger vessels (non-capillaries) that is established throughout vascular brain development. Strikingly, these results were again very similar in the three brain regions, suggesting a more general underlying concept of vessel directionality/orientation. Even though we do not fully understand these data at present, one might think of these preferred orientations of non-capillaries as predefined vascular "routes" into specific brain structures that then terminate into the capillary beds which are more randomly orientated. Comparison of the quantification of individual vascular parameters obtained by scanning the entire mouse brain in high resolution with that of the two-step ROI-based approach during which the ROIs first have to be placed on a lower resolution overview µCT scan with subsequent high-resolution SRµCT scanning of selected ROIs, revealed very similar results (Figure 13 and Supplementary Figures 17-21).

The exact values might vary in different experimental settings and thus correlate with the angiogenic activity of the specificity of investigated tissue[77]. Nevertheless, we feel that the selected parameters, obtained by our improved protocol might be helpful readouts for better understanding angiogenesis in various biological settings.

A powerful novel tool to image and analyze the postnatal and adult mouse brain vasculature

Concluding, 3D computational reconstructions of corrosion casts are a powerful tool to investigate any biologically relevant question regarding angiogenesis (genetic mechanisms in physiology and pathophysiology as well as the effect of drugs) because it allows quantification of the morphological features of entire vascular networks. This protocol of vascular corrosion casting techniques combined with SEM, with or without SRµCT imaging, and computational

network analysis, can be used to demonstrate quantitatively the morphological changes occurring in the mouse brain between birth and adult stage of vascular brain development. We anticipate that, following appropriate validation, this method could be used to visualize and analyze 3D vascular networks in additional mouse organs.

ACKNOWLEDGMENTS

We thank Katrien De Bock, Marc Schwab, Moheb Ghobrial, and Jing Zhang for help with the animal perfusions, Sebastian Eichelbaum for help with the computational analysis and 3D visualizations (http://www.nemtics.com), and Nancy Chu Ji for help with the illustrations. T.W. was supported by the OPO Foundation, the Swiss Cancer Research foundation (KFS-3880-02-2016-R, KFS-4758-02-2019-R), the Stiftung zur Krebsbekämpfung, the Kurt und Senta Herrmann Foundation, Forschungskredit of the University of Zurich, the Zurich Cancer League, the Theodor und Ida Herzog Egli Foundation, the Novartis Foundation for Medical-Biological Research, and the HOPE Foundation. P.C. was supported by long-term structural Methusalem funding by the Flemish Government (14/08), and a European Research Council (ERC) Advanced Research Grant (EU-ERC269073). J.V. was supported by the Swiss National Science Foundation (no. 310000 120321/1). All the animal experiments were conducted in J.V.'s laboratory and were approved by the Veterinary office of the Canton of Zurich.

AUTHOR CONTRIBUTIONS

T.W. had the idea for the study, designed the experiments, wrote the manuscript, and made the figures. T.W., A.U.S., E.P.M., and C.H. conducted the experiments. T.W., J.V., A.M. and J.B. analyzed the data. T.W. wrote the manuscript, J.B. helped editing the manuscript and figures. R.W. helped with the animal experiments and gave critical inputs to the manuscript. A.M., A.U.S., T.K., K.D.B., P.C., J.V., and M.S. gave critical inputs to the manuscript. All authors read and approved the final version of the manuscript.

DISCLOSURE/CONFLICT OF INTEREST

T.K. is an employee of the Novartis Institutes for BioMedical Research, Inc., E.P.M is co-founder of vasQtec.

DATA AVAILABILITY

The raw data underlying all graphical figures is provided in individual Excel (comma separated value (".csv")) files via Figshare (https://doi.org/10.6084/m9.figshare.13483119). For each panel of every figure, a ".csv" file is provided with the linked figure noted within both the file and the file name.

RELATED LINKS

Key references using this protocol:

1. Heinzer, S. *et al*. *Neuroimage* **39**, 1549-1558 (2008). https://doi.org/10.1016/j.neuroimage.2007.10.054
2. Meyer, E. P. *et al*. *Proc Natl Acad Sci U S A* **105**, 3587-3592 (2008). https://doi.org/10.1073/pnas.0709788105
3. Wälchli, T. *et al. J Cereb Blood Flow Metab* **37**, 614-631 (2017). https://doi.org/10.1177/0271678X16675182

FIGURE LEGENDS

Figure 1 Flow chart, summary, and time frame of the procedure

The different sections of the protocol are indicated in color-coded boxes. White boxes indicate preparation steps, green boxes describe experimental steps, blue boxes indicate analysis steps and brown boxes describe quality control steps. Black arrows indicate the order in which the different steps of the protocol are performed. A time scale in days is shown on the left.

Figure 2 Intracardial resin perfusion and brain dissection for postnatal day 10 (P10) animals

a-b Schematic drawing illustrating the experimental setup before (**a)** and after **(b)** resin perfusion. Surgical opening (**c**,**d**), angle of 30° in the sagittal plane (**e**) and site of needle insertion (**e**) for intracardial perfusion with 10–20 ml artificial cerebrospinal fluid containing 25,000 U/L Heparin via the left ventricle, followed by 4% (wt/vol) paraformaldehyde in phosphate buffered saline, and by **(f)** the polymer resin PU4ii (vasQtec, Zürich, Switzerland), were all infused at the same rate (4 ml/min and 90-100 mmHg) in a P10 mouse pup (see also Supplementary Video 1). Successful perfusion is indicated by a bluish aspect of the animal, which can be well observed at the paws (white arrow), snout (white arrowhead) or tail (white outlined arrowhead). **g-j** Schematic drawings depicting the individual steps visible in **c-f**. **k** Resin cast of a P10 animal after soft tissue maceration, before (**k**) and after (**l**) bony tissue decalcification (paw, white arrow and snout, white arrowhead). **m** The cerebral vasculature is sharply dissected from the extracranial vessels resulting in the isolated brain vascular corrosion cast of the P10 mouse brain (white arrow, **m**) (**n**). Scale bars, 5 mm (**k-n**).

Figure 3 The principles of (brain) vascular corrosion casting

a-g Photograph **(a)** and schematic drawing (**b**) of a whole adult (P60) mouse after perfusion of resin PU4ii. Insets showing a schematic illustration of the principle of vascular corrosion casting (**c**,**d**), in which the vascular corrosion casts represents the inner volume of perfused blood vessels in blue; defined by the inner vessel diameter, before **(c)** and after **(d)** maceration of soft tissues. Maceration of the surrounding CNS tissue including the blood vessel wall and decalcification of bony structures, exposes the entire vascular corrosion cast (**e**,**f**), with a schematic drawing of the casted brain vasculature in more detail **(g)**.

Figure 4 The placement of the regions of interest (ROIs) and process of computational 3D reconstruction

Schematic visualization of the ROI placement in both postnatal (P10) (**a-d**) and adult (P60) (**e-h**) mouse brains with 3D overviews (**a**,**e**) and detailed panels for the respective anatomical plane (**b**,**f** coronal, **c**,**g** sagittal, **d**,**h** axial). The µCT scanning procedure of a vascular corrosion cast, includes the placement of ROIs, here depicted in the 3D rendering of a whole postnatal (P10) WT brain, shown in the different anatomical planes **(i-l)** (red: cortex, blue: hippocampus, yellow: superior colliculus, green: corpus callosum, and black: brain stem). **m** Raw images of single µCT projections in the x-plane, y-plane, and in the z-plane (from left to right) of a ROI placed in the cortex of a P10 WT animal, followed by **(n)** the same z-plane for which the edges of the segmented regions are shown as red outlines (Otsu's thresholding method). **o** Visualization of the image segmentation and skeleton tracing process. In the imaging process, the original vessel structure (left) is converted into a digital approximation that is segmented using the Otsu method (middle). The centerlines of the vessels are found using skeletonization (middle, highlighted pixels). The pixel-accurate centerline (middle, black dotted line) is smoothed for better representation of the centerlines of the individual vessel branches (right, colored lines). For each branch its length is measured as a sum of distances between the smoothed centerline points (right, colored points), and its diameter as the average diameter of the branch (right, arrows). **p** Three-dimensional visualization of the original data (P10 WT cortex) showing the CT plane (grayscale), the segmented vessels (red, left side) and the vessel centerlines (blue lines, right side). Part of segmentation has been cut off in the front of the CT plane. Scale bars: 250 µm (**i-l**),100 µm (**m**,**n**)

Figure 5 Global vascular network morphometry - Increased vascular volume fraction in various regions of the adult (P60) WT versus postnatal (P10) WT mouse brain

a-d Computational 3D reconstructions of the vascular network using surface rendering based on the synchrotron radiation μCT data showing a ROI as volume mask (**a**), after the vessel segmentation process (**b**), and after the placement of centerlines (**c**), with a zoom of both stages combined (**d**)**.** Blood vessel structures of all sizes are well defined. **e-g** Computational 3D reconstructions of μCT scans of vascular networks of the postnatal (P10) WT and adult (P60) WT mouse brains displayed with color-coded vessel thickness. The increased vessel density in the P60 WT cortices (**e**), hippocampi (**f**) and superior colliculi (**g**) is obvious. Color bar indicates vessel radius (μm). The boxed areas are enlarged at right. **h-j** Quantification of the 3D vascular volume fraction in P10 cortex (**h**), hippocampus (**i**), and superior colliculus (**j**), by computational analysis using a global morphometry approach. The vascular volume fraction in all these brain structures was significantly higher in the P60 WT animals than that in the P10 WT animals (n = 4-6 for P10 WT; n = 8-12 for P60 WT animals; and in average three ROIs per animal and brain region have been used). All data are shown as mean distributions, where the open dot represents the mean. Boxplots indicate the 25% to 75% quartiles of the data. *P < 0.05, **P < 0.01, ***P < 0.001. Scale bars: 100 μm (**e-g**, overview); 50 μm (**e-g**, zoom).

Figure 6 Local vascular network topology – Increased vascular volume fraction of the adult (P60) WT versus postnatal (P10) WT cortex mainly found at the capillary level

a,**b** Scheme illustrating a capillary bed and the distinction between capillaries and non-capillaries based on the radius of the inner volume of resin-perfused blood vessels after maceration of the surrounding CNS tissue including the blood vessel wall. A capillary is defined as a blood vessel with an inner diameter (**a**,**b**, green) of < 7µm, whereas a non-capillary vessel is defined a blood vessel with an inner diameter (**a**,**b**, magenta) of ≥ 7µm, according to[173]. **c**,**d** Three-dimensional computational reconstruction of µCT scans of cortical vascular networks in a P60 WT sample highlighting a vessel tree with non-capillaries in magenta and capillaries in green.

Figure 7

a-c Histograms showing the distribution of vessel diameter in P10 WT and P60 WT animals. P60 WT animals show an increased absolute frequency of capillaries as compared to the P10 WT situation, whereas the number of non-capillaries remains largely unchanged in (**a**) the cortex, (**b**) hippocampus, (**c**) and superior colliculus (bin width = 0.36 µm; number of bins = 55). Black dashed line marks the separation between capillaries (< 7µm) and non-capillaries (≥ 7µm). **d**,**e** Computational 3D reconstructions of µCT images of vascular networks of P10 WT and P60 WT mice in the cortices separated for non-capillaries (magenta) and capillaries (green). The increased density of capillaries (green) in the P60 WT samples for the cortices is evident, density in non-capillaries (magenta) is also increased. The boxed areas are enlarged at the right for capillaries (**d**,**e**). **f-h** Quantification of the 3D vascular volume fraction for all vessels (**f**), non-capillaries (**g**), and capillaries (**h**) in P10 WT and P60 WT calculated by local topology analysis. The significant increase of the vascular volume fraction for all vessels in the P60 WT animals (**f**) was mainly due to a significant increase at the level of capillaries (**h**) (n = 4-6 for P10 WT; n = 8-12 for P60 WT animals were used; and in average three ROIs per animal and brain region were used). All data are shown as mean distributions where the open dot represents the mean. Boxplots indicate the 25% to 75% quartiles of the data. The shaded blue and red areas indicate the SD. *P < 0.05, **P < 0.01, ***P < 0.001. Scale bars: 100 µm (**d**,**e**, overviews); 50 µm (**d**,**e**, zooms).

Figure 8 Local vascular network topology – visualization and quantification of vascular branch point diameter and vascular branch point density in various regions of the adult (P60) WT versus the postnatal (P10) WT mouse brain

a Scheme illustrating a capillary bed and the distinction between capillaries and non-capillaries based on the radius of the inner volume of resin-perfused blood vessels (see legend figure 6a). **b** Scheme depicting the definition of vascular branch points. Each voxel of the vessel center line (black) with more than two neighboring voxels was defined as a vascular branch point. This results in branch point degrees (number of vessels joining in a certain branch point) of minimally three. In addition, two branch points were considered as a single one if the distance between them was below 2µm (**b**). Branch point are depicted as black dots in **a**,**b**. **c** Histogram showing the distribution of branch point diameter in P10 WT and P60 WT animals. P60 WT animals show an increased branch point density as compared to P10 WT mice mainly at the capillary level (bin width = 0.38µm; number of bins = 40). Black dashed line marks the separation between capillaries (< 7µm) and non-capillaries (≥ 7µm), as defined in Figure 6. **d**,**e** Computational 3D reconstructions of µCT images of cortical vascular networks of P10 WT and P60 WT mice with visualizations of the vessel branch points displayed as dots, separately for non-capillaries (magenta) and capillaries (green). The higher density of branch points in the P60 WT cortices especially at the capillary level (green) is obvious, a slight increase of branch point density can be observed at the non-capillary level (magenta). The boxed areas are enlarged at the right. **f-h** Quantitative analysis of the branch point density for all vessels (**f**), non-capillaries (**g**), and capillaries (**h**) in P10 WT and P60 WT cortices by local morphometry analysis. The significant increase of the branch point density for all vessels in the P60 WT animals (**f**) was mainly due to a significant increase at the level of capillaries (**h**) and in part due to a significant increase at the level of non-capillaries (**g**). (n = 4-6 for P10 WT; n = 8-12 for P60 WT animals were used; and in average three ROIs per animal were used). All data are shown as mean distributions where the open dot represents the mean. Boxplots indicate the 25%

to 75% quartiles of the data. The shaded blue and red areas indicate the SD. *P<0.05, **P<0.01, ***P<0.001. Scale bars: 100 μm (**d**,**e**, overviews); 50 μm (**d**,**e**, zooms).

Figure 9 Local vascular network topology – segment density, -diameter, -length, -tortuosity, and -volume of the adult (P60) WT versus the postnatal (P10) WT mouse brain

a,**b** Schemes showing the definition of vessel diameter (**a**), vessel length (**a**), and vessel tortuosity (**b**). The segment diameter is defined as the average diameter of all single elements of a segment (**a**). The segment length is defined as the sum of the length of all single elements between two branch points (**a**). The segment tortuosity is the ratio between the effective distance l_e and the shortest distance l_s between the two branch points associated to this segment (**b**). The segment density is defined as the number of segments, classified into global, capillary and non-capillary segments, divided by the network volume. **c** Graph depicting the relationship between segment diameter and segment length in P10 WT and P60 WT animals. The ratio "segment diameter-to-segment length" was higher in P10 WT mice compared to P60 WT mice (bin width = 4.93; number of bins = 14). **d-f**,**g-n** Quantification of the 3D vessel network parameters segment density (**d-f**), segment diameter (**g-j**), and segment length (**k-n**) for all vessels, non-capillaries, and capillaries in P10 WT and P60 WT cortices calculated by local morphometry analysis. The segment density (**d**) was significantly increased for all vessels in the cortices of P60 WT mice as compared to the P10 WT mice, whereas the segment diameter (**h**) and segment length (**l**) were significantly decreased for all vessels in the P60 WT mice as compared to the P10 WT mice. In line with the other parameters, these differences were mainly due to a highly significant increase respectively decrease at the level of capillaries (**f**,**j**,**n**) and in part due to an increase respectively decrease at the level of non-capillaries (**e**,**i**,**m**) (n = 4-6 for P10 WT; n = 8-12 for P60 WT animals; and in average three ROIs per animal and brain region were used). (**g** bin width = 0.36 µm; number of bins = 55, **k** bin width = 2.5 µm; number of bins = 40). All data are shown as mean distributions where the open dot represents the mean. Boxplots indicate the 25% to 75% quartiles of the data. The shaded blue and red areas indicate the SD. *P < 0.05, **P < 0.01, ***P < 0.001.

Figure 10

Quantification of the 3D vessel network parameters segment tortuosity and segment volume (**a-h**) for all vessels, non-capillaries, and capillaries in P10 WT and P60 WT cortices calculated by local morphometry analysis. The segment tortuosity (**a,b**) and segment volume (**e,f**) were significantly increased for all vessels in the cortices of P60 WT mice as compared to the P10 WT mice. In line with the other parameters, these differences were mainly due to a highly significant increase respectively decrease at the level of capillaries (**d,h**) and in part due to an increase respectively decrease at the level of non-capillaries (**c,g**) (n = 4-6 for P10 WT; n = 8-12 for P60 WT animals; and in average three ROIs per animal and brain region were used). (**a** bin width = 0.013; number of bins = 80, **e** bin width = 2957.74 μm^3; number of bins = 55). All data are shown as mean distributions where the open dot represents the mean. Boxplots indicate the 25% to 75% quartiles of the data. The shaded blue and red areas indicate the SD. *P < 0.05, **P < 0.01, ***P < 0.001.

Figure 11 Local vascular network topology – extravascular distance is decreased in various regions of the adult (P60) WT versus the postnatal (P10) WT mouse brain

a Schematic defining the extravascular distance as the shortest distance of any given voxel in the tissue to the next vessel structure. **b** Histogram showing the distribution of the extravascular distance in P10 WT and P60 WT animals. P60 WT animals show an increased relative frequency of shorter extravascular distances as compared to the P10 WT situation (bin width = 10; number of bins = 20). **c-h** Color map indicating the extravascular distance in the cortices, hippocampi and superior colliculi of P10 WT and P60 WT mice. Each voxel outside a vessel structure is assigned a color to depict its shortest distance to the nearest vessel structure. The reduced extravascular distance in P10 WT animals as compared to the P60 WT animals is obvious. The color bars indicate the shortest distance to the next vessel structure. **i-k** Quantification of the extravascular distance in P10 WT and P60 WT in the three brain regions calculated by global morphometry analysis. The extravascular distance in the cortices (**i**), hippocampi (**j**) and superior colliculi (**k**) of P60 WT animals was significantly decreased as compared to the P10 WT animals (n = 4-6 for P10 WT; n = 8-12 P60 WT animals were used; in average three ROIs per animal and brain region were analyzed). All data are shown as mean distributions where the open dot represents the mean. Boxplots indicate the 25% to 75% quartiles of the data. The shaded blue and red areas indicate the SD. *P<0.05, **P<0.01, ***P<0.001. Scale bars: 100 µm (**c-h** overviews); 50 µm (**c-h** zooms).

Figure 12 Global vascular network morphology – visualization of distinct patterns of vessel directionality in various brain regions of the adult (P60) WT and postnatal (P10) WT mouse brain

a Computational 3D reconstruction of μCT scans of cortical vascular networks of P60 WT displayed with color-coded directionality obtained by attributing every vessel segment to its main direction in the x (red), y (green), and z (blue) planes within the selected ROIs. **b**,**c** Computational 3D reconstruction of μCT scans color-coded for vessel directionality depicting the P10 WT (**b**) and P60 WT (**c**) cortex. Cortical renderings clearly show that the superficial perineural vascular plexus (PNVP) extended in the x- and y-directions, whereas the interneural vascular plexus (INVP) exhibited a radial sprouting pattern into the brain parenchyma along the z-axis, perpendicular to the PNVP. **d-f** Quantitative analysis showing histograms for the distribution of the relative angles of the vascular segments emanating from a certain branch point (segment angle for adjacent vessels) in P10 and P60 animals in the cortex. Non-capillaries revealed two main angles of orientation, namely around 90° and at around 170°, and these two main angles of orientation were more pronounced at the adult P60 as compared to the developing P10 stage (**e**). The capillaries derived at angles between around 75° and 150° at both the developing P10 and mature P60 stages in the cortex, (**f**). (**d-f** bin width = 5; number of bins = 55). Scale bars: 100 μm (**b**,**c**).

Figure 13 High resolution SRμCT scan of the entire postnatal (P10) and adult (P60) mouse brain – visualization and quantification of various anatomical brain regions reveals increased vascular volume fractions in the P60 versus P10 mouse brain

Cross sections of the whole-brain scan in both P10 (**a-d**) and P60 (**e-h**) mouse brains with 3D overviews (**a**,**e**) and detailed panels for the respective anatomical planes (**b**,**f** coronal, **c**,**g** sagittal, **d**,**h** axial). Computational 3D reconstructions of μCT scans of vascular networks of the P10 WT and P60 whole brain scans, displayed with color-coded vessel thickness. The increased vessel density in the P60 WT (**j**) cortex, hippocampus, thalamus, cerebellum, medulla and pons, as compared to the P10 WT (**i**) samples is obvious. Color bar indicates vessel radius (μm). **k-r** Quantification of the 3D vascular volume fraction in P10 cortex (**k**), hippocampus (**l**), superior colliculus (**m**), thalamus (**n**), hypothalamus (**o**), cerebellum (**p**), pons (**q**), medulla (**r**) by computational analysis using a global morphometry approach. The vascular volume fraction in all these brain structures was higher in the P60 WT animals than that in the P10 WT animals (the anatomical regions were divided into ROI-sized sections for analysis: between n = 5, dentate gyrus, and n = 126, cortex for P10 WT; and between n = 4, CA3, and n = 76, cortex, of these sections for P60 WT were analyzed, highly dependent on the size of the anatomical region). All data are shown as mean distributions, where the open dot represents the mean. Boxplots indicate the 25% to 75% quartiles of the data. *P < 0.05, **P < 0.01, ***P < 0.001. Scale bars: 2.5 μm (**a-h**, overviews), 0.25 μm (**a**,**e**, zooms), 1 μm (**b-d**, **f-h**, zooms).

Figure 14 Working model summarizing the differences in 3D vascular network architecture between adult (P60) WT and postnatal (P10) WT mice

a-d Schematic illustrations of the postnatal and adult mouse brain vasculature, both as 3D whole brains (**a**) and as enlargements specified for the different anatomical regions, namely cortex (**b**), hippocampus (**c**) and superior colliculus (**d**). **e**,**f** From the P10 to the P60 stage, an increased vascular volume fraction of functional blood vessels established via increased vascular endothelial sprouting, branching, and -migration mainly at the capillary level can be observed (**e**,**f**). **g** Schematics summarizing the most important differences in the 3D vascular network architecture of P10- and P60 mouse brains: The vascular volume fraction (percentage of tissue volume occupied by the entire vascular network), the branchpoint- and vessel/segment density, the branchpoint degree, and the vessel/segment tortuosity are increased in the mature P60 as compared to the developing P10 animals. On the other hand, the vascular parameters vessel/segment length, vessel/segment volume, vessel/segment- and branchpoint diameter, and the extravascular distance are decreased in the mature P60 as compared to the developing postnatal P10 mice. The vessel directionality showed more pronounced angles of orientation for non-capillaries at the P60 stage as compared to P10 stage, whereas the orientation of the capillaries seemed largely unchanged between the two developmental stages.

EXTENDED DATA FIGURE LEGENDS

Extended Data Figure 1 Intracardial resin perfusion and brain dissection for adult (P60) animals

The main steps of resin perfusion and brain dissection are shown as photographs for the perfusion and brain dissection of adult (P60) mice. **a-c** Fixation (**a)**, surgical opening (**b**,**c**) and site of needle insertion (**c**) for intracardial perfusion (via the left ventricle) with 10–20 ml artificial cerebrospinal fluid containing 25,000 U/L Heparin, followed by 4% paraformaldehyde in phosphate buffered saline, and then by the polymer resin PU4ii (vasQtec, Zürich, Switzerland), all infused at the same rate (8 ml/min and 100-120 mmHg) in an adult (P60) mouse (see also Supplementary Video 1). **d** Successful perfusion is indicated by a bluish aspect of the animal, which can be easiest observed at the paws (white arrow) or the snout (white arrowhead). **e**,**f** Resin cast of a P60 animal after soft tissue maceration, and before (**e**) and after (**f**) decalcification of bone structures. **f-h** The cerebral vasculature is sharply dissected from the extracranial vessels resulting in the isolated brain vascular corrosion cast of the P60 mouse brain (**g**,**h**). Scale bars, 10 mm (**e-h**).

Extended Data Figure 2 Validation of vascular corrosion casting in postnatal (P10) and adult (P60) mice using light microscopy (LM) and scanning electron microscopy (SEM)

a-f Quality control of the vascular corrosion casts of P10 and P60 WT mice by visual inspection by LM (**a**), and by SEM (**b-f**). **a** Light microscopy image of the entire brain vasculature of the P60 WT mice (gold sputtered for SEM). **b** SEM image of the entire brain vascular corrosion cast illustrating the dense vascular network including blood vessels of all sizes with recognizable vascular anatomy. **c-f** The entire brain was uniformly filled with resin and the lumen of the vessels imprinted in the casting material with the finest details. **e** The capillary network in the cortex is well defined and devoid of interruptions. **f** Note the elongated cellular and nuclear imprints on the large vessel that are also typical for good-quality vascular corrosion casts in adult mice[106]. Scale bars: 4 mm (**a**); 4 mm (**b**); 50 μm (**c**); 50 μm (**d**), 100 μm (**e**), 100 μm (**f**)

Reproduced with permission from:

a,d-f Wälchli et al. Nogo-A Regulates Vascular Network Architecture in the Postnatal Brain. *J Cereb Blood Flow Metab* 2017 Feb;37(2):614-631

b Krucker et al. New polyurethane-based material for vascular corrosion casting with improved physical and imaging characteristics. *Microsc Res Tech* 2006 Feb;69:138–147

Extended Data Figure 3 Global vascular network morphometry – Increased vascular volume fraction in various regions of the adult (P60) Nogo-A$^{-/-}$ versus postnatal (P10) Nogo-A$^{-/-}$ mouse brain

Genetic deletion of Nogo-A leads to increased vascular volume fraction in various regions of the postnatal mouse brain. **a-c** Computational 3D reconstructions of μCT scans of vascular networks of P10 and P60 Nogo-A$^{-/-}$ mice displayed with color-coded vessel thickness. The increased vessel density in the Nogo-A$^{-/-}$ animals, as compared to the WT animals (Figure 5) in the cortices (**a**), hippocampi (**b**) and superior colliculi (**c**) is obvious. Color bar indicates vessel radius. The boxed areas are enlarged at right. (n = 11 for P10 Nogo-A$^{-/-}$; n = 13 for P60 Nogo-A$^{-/-}$ animals; and in average three ROIs per animal and brain region were used). Scale bars: 100 μm (**a-c** overviews); 50 μm (**a-c** zooms).

Extended Data Figure 4 Local vascular network topology – Increased vascular volume fraction of the adult (P60) Nogo-A$^{-/-}$ versus postnatal (P10) Nogo-A$^{-/-}$ mouse brain mainly found at the capillary level

Genetic deletion of Nogo-A leads to increased vascular volume fraction in various regions of the P10 mouse brain. **a** Computational 3D reconstruction of μCT images of vascular networks of P10 and P60 Nogo-A$^{-/-}$ mice separated for non-capillaries (magenta) and capillaries (green). The increased density of capillaries (green) in the P60 and P10 Nogo-A$^{-/-}$ samples is evident when compared to the WT animals (Figure 7), non-capillaries (magenta) appear largely unchanged. The boxed areas are enlarged at right (**a-c**). Scale bars: 100 mm (**a-c**, overviews); 50 mm (**a-c**, zooms).

Extended Data Figure 5 Local vascular network topology - visualization and quantification of vascular branch point diameter and vascular branch point density in the hippocampus of the adult (P60) WT versus the postnatal (P10) WT mouse brain

The vascular branch point diameter and vascular branch point density are significantly increased in the P60 as compared to the P10 mouse brain hippocampus. **a** Scheme depicting the definition of vascular branch points (see Figure 8b for details) **b** Histogram showing the distribution of branch point diameter plotted against the branch point density in P10 WT and P60 WT animals. P60 WT animals show an increased branch point density as compared to P10 WT (bin width = 0.38µm; number of bins = 40). Black dashed line marks the separation between capillaries (< 7 µm) and non-capillaries (≥ 7 µm), as defined in Figure 6. **c,d** Computational 3D reconstructions of µCT images of vascular networks in the hippocampi of P10 WT and P60 WT mice with visualizations of the vessel branch points displayed as dots, separated for non-capillaries (magenta) and capillaries (green). The higher density of branch points in the P60 WT hippocampi especially at the capillary level (green) is obvious, a slight increase of branch point density can be observed at the non-capillary level (magenta). The boxed areas are enlarged at right. **e–g** Quantitative analysis of the branch point density for all vessels (**e**), non-capillaries (**f**), and capillaries (**g**) in P10 WT and P60 WT hippocampi by local morphometry analysis. The significant increase of the branch point density for all vessels in the P60 WT animals (**e**) was mainly due to a significant increase at the level of capillaries (**g**) and in part due to a significant increase at the level of non-capillaries (**f**). In average, n = 2-7 animals were used for the hippocampi and in average three ROIs per animal and brain region were used. All data are shown as mean distributions where the open dot represents the mean. Boxplots indicate the 25% to 75% quartiles of the data. The shaded blue and red areas indicate the SD. *P<0.05, **P<0.01, ***P<0.001. Scale bars: 100 µm (**c-d** overviews); 50 µm (**c-d** zooms).

Extended Data Figure 6 Local vascular network topology – visualization and quantification of vascular branch point diameter and vascular branch point density in the superior colliculus of the adult (P60) WT versus the postnatal (P10) WT mouse brain The vascular branch point diameter and vascular branch point density are significantly increased in the P60 as compared to the P10 mouse brain superior colliculus. **a** Scheme depicting the definition of degree 3 and 4 vascular branch point (see Figure 8b for details). **b** Histogram showing the distribution of branch point diameter plotted against the branch point density in P10 WT and P60 WT animals. P60 WT animals show an increased branch point density as compared to P10 WT mice mainly at the capillary level (bin width = 0.38; number of bins = 40). Black dashed line marks the separation between capillaries (< 7 μm) and non-capillaries (≥ 7 μm), as defined in Figure 6. **c**,**d** Computational 3D reconstructions of μCT images of vascular networks of the superior colliculi of P10 WT and P60 WT mice with visualizations of the vessel branch points displayed as dots, separately for non-capillaries (magenta) and capillaries (green). The higher density of branch points in the P60 WT superior colliculi especially at the capillary level (green) is obvious, a slight increase of branch point density can be observed at the non-capillary level (magenta). The boxed areas are enlarged at right. **e–g** Quantitative analysis of the branch point density for all vessels (**e**), non-capillaries (**f**), and capillaries (**g**) in P10 WT and P60 WT superior colliculi by local morphometry analysis. The significant increase of the branch point density for all vessels in the P60 WT animals (**e**) was mainly due to a significant increase at the level of capillaries (**g**) and in part due to a significant increase at the level of non-capillaries (**f**). In average, n = 2-4 animals were used for the superior colliculus; and in average three ROIs per animal and brain region were used. All data are shown as mean distributions where the open dot represents the mean. Boxplots indicate the 25% to 75% quartiles of the data. The shaded blue and red areas indicate the SD. *P<0.05, **P<0.01, ***P<0.001. Scale bars: 100 μm (**c**,**d**, overviews); 50 μm (**c**,**d**, zooms).

Extended Data Figure 7 Resin PU4ii vascular corrosion casting combined with immunofluorescence

Visualization by fluorescence light microscopy of the brain vasculature after the addition of fluorescent pigments to the PU4ii resin solution in the P60 mouse brains with preserved/non-macerated soft tissue (**a**-**f**), co-labeled with red fluorescent myelin stainings (**g-j**). Overviews (**a,b**,**d,e**) and coronal cortical sections (**c**,**f**) of P60 mouse brains with yellow/green- (**a**,**b**,**c)** and UV-blue (**d**,**e,f**) fluorescent dyes (vasQtec) added to the PU4ii resin showing the brain vasculature; overviews: dorsal overviews (**a**,**d**), ventral overviews (**b**,**e**), coronal sections (**c**,**f**). The selection of the brain regions analyzed here has been done on coronal sections in the structures selected using the Allen Mouse Brain Atlas. **c**,**f**,**g-j** Fluorescence light microscopy overviews of multiple brain regions in 150 µm coronal sections of a P60 mouse brain perfused with either yellow/green- (**c**,**h-j**) or UV-blue (**f**,**g**) fluorescent pigments added to the PU4ii resin solution, showing the cortical layers and part of the hippocampus (**c**,**f**). Fluorescence light microscopy of coronal sections in which the preserved/non-macerated soft tissue was labeled with a red fluorescent myelin stain (FluoroMyelin Red, Molecular Probes Inc) to visualize the corpus callosum and other highly myelinated brain structures (red). Scale bars, 1 mm (**a**,**b**,**d**,**e**); 500 µm (**c**,**d**,**g-j**). Excitation/emission of the yellow/green pigments at 450nm/550nm, excitation/emission of the UV-blue fluorescent pigment at 375nm/430nm.

SUPPLEMENTARY FIGURE LEGENDS

Supplementary Figure 1 Validation of vascular corrosion casting in adult (P60) mice using scanning electron microscopy (SEM) – examples of insufficiently perfused mouse brain vasculature

Quality control of the vascular corrosion casts of P60 WT mice by SEM. **a**,**b** SEM images showing the cortical surface of a vascular corrosion cast illustrating abrupt changes in segment diameter (arrowheads), likely caused by vessel lumen obstruction during resin perfusion. **c**,**d** The irregular surface shape of vessels combined with rounded abrupt ends of larger vessels are the typical signs of incomplete vascular corrosion casting. The rounded abrupt dead-ends (arrowheads) are caused by casting material pushing against trapped air pockets that were introduced during the perfusion procedure, thereby interrupting physiological flow. Absence of imprints of endothelial cell nuclei further indicates insufficient casting. **e**,**f** Larger vessels are visibly distended with rounded abrupt dead-ends (arrowheads) and are missing endothelial cell nuclei imprints. The capillary network in the cortex is not well defined and shows interruptions, further illustrating incomplete casting. Scale bars: 200 μm (**a**); 200 μm (**b**); 150 μm (**c**); 150 μm (**d**), 150 μm (**e**), 150 μm (**f**).

Supplementary Figure 2 Overview of the main vascular parameters in various regions of the wildtype postnatal and adult mouse brain

Quantification of the main vascular parameters, depicted as fold change of the mean in the WT P60 mouse brain as compared to the P10 mouse brain. **a**,**b**,**g** On a volumetric level, the vascular volume fraction (VVF), was analyzed by computational analysis using the global morphometry, and local topology approach in the cortex (**a**), hippocampus (**b**) and superior colliculus (**g**). The vascular volume fraction in all these brain structures was significantly higher in the WT P60 animals than that in the P10 WT animals. **c**,**d**,**h** On the level of vascular segments, the parameters segment- diameter, - length, - tortuosity, - volume and -density are depicted as fold change of the mean. The parameters segment diameter, - length and -volume show a highly significant decrease or non-significant increase, whereas the parameters segment tortuosity and -density show an increase. All these changes are most pronounced on the capillary level. **e**,**f**,**i** Investigating the difference in branchpoint characteristics between P60 and P10 wildtype mouse brains, the vascular parameters branch point diameter, -degree, -density, branch point degree 3 density and branch point degree 4 density were analyzed. Branch point diameter shows a significant decrease in the P60 as compared to the P10 mouse brain on a capillary level in all three brain regions. The vascular parameters branch point degree, - density, branch point degree 3 density and branch point degree 4 density all show a relative increase, again most pronounced on the capillary level, in all three brain regions (n = 4-6 for P10 WT; n = 8-12 for P60 WT; n = 3-5 for P10 Nogo-$A^{-/-}$; n = 8-11 for P60 Nogo-$A^{-/-}$ animals; and in average three ROIs per animal and brain region were used). All data are shown as fold change of the mean distributions, where the magenta bars correspond to the non-capillaries and the green bar corresponds to the capillaries. *P < 0.05, **P < 0.01, ***P < 0.001.

Supplementary Figure 3 Local vascular network topology – Increased vascular volume fraction of the adult (P60) WT versus postnatal (P10) WT hippocampi mainly found at the capillary level

a,**b** Three-dimensional computational reconstruction of µCT scans of vascular networks in the hippocampus of a P60 WT sample highlighting a vessel tree with non-capillaries in magenta and capillaries in green. **c-e** Quantification of the 3D vascular volume fraction for all vessels (**c**), non-capillaries (**d**), and capillaries (**e**) in P10 WT and P60 WT calculated by local topology analysis. The significant increase of the vascular volume fraction for all vessels in the P60 WT animals (**c**) was mainly due to a significant increase at the level of capillaries (**e**) (n = 4-6 for P10 WT; n = 8-12 for P60 WT animals were used; and in average three ROIs per animal and brain region were used). All data are shown as mean distributions where the open dot represents the mean. Boxplots indicate the 25% to 75% quartiles of the data. The shaded blue and red areas indicate the SD. *P < 0.05, **P < 0.01, ***P < 0.001. Scale bars: 100 µm (**a**,**b**, overviews); 50 µm (**a**,**b**, zooms).

Supplementary Figure 4 Local vascular network topology – Increased vascular volume fraction of the adult (P60) WT versus postnatal (P10) WT superior colliculi mainly found at the capillary level

a,**b** Three-dimensional computational reconstruction of µCT scans of vascular networks in the superior colliculus of a P60 WT sample highlighting a vessel tree with non-capillaries in magenta and capillaries in green. **c-e** Quantification of the 3D vascular volume fraction for all vessels (**c**), non-capillaries (**d**), and capillaries (**e**) in P10 WT and P60 WT calculated by local topology analysis. The significant increase of the vascular volume fraction for all vessels in the P60 WT animals (**c**) was mainly due to a significant increase at the level of capillaries (**e**) (n = 4-6 for P10 WT; n = 8-12 for P60 WT animals were used; and in average three ROIs per animal and brain region were used). All data are shown as mean distributions where the open dot represents the mean. Boxplots indicate the 25% to 75% quartiles of the data. The shaded blue and red areas indicate the SD. *P < 0.05, **P < 0.01, ***P < 0.001. Scale bars: 100 µm (**a**,**b**, overviews); 50 µm (**a**,**b**, zooms).

Supplementary Figure 5 Overview of the effects of physiological ageing and of genetic deletion of Nogo-A on the vascular volume fraction in various regions of the adult (P60) and postnatal (P10) mouse brain

a-i Quantification of the 3D vascular volume fraction in cortex (**a-c**), hippocampus (**d-f**), and superior colliculus (**g-i**), by computational analysis using global morphometry. The vascular volume fraction in all these brain structures was significantly higher in the Nogo-A deficient animals than that in the WT control animals. This same increase can be observed in the P60 WT group, when compared to the P10 WT animals, and is most pronounced at the level of capillaries (**c**,**f**,**i**) (n = 4-6 for P10 WT; n = 8-12 for P60 WT; n = 3-5 for P10 Nogo-$A^{-/-}$; n = 8-11 for P60 Nogo-$A^{-/-}$ animals; and in average three ROIs per animal and brain region were used). *P < 0.05, **P < 0.01, ***P < 0.001.

Supplementary Figure 6 Overview of the effects of physiological ageing and of genetic deletion of Nogo-A on the branch point density in various regions of the adult (P60) and postnatal (P10) mouse brain

a-i Quantification of the branch point density in cortex (**a-c**), hippocampus (**d-f**), and superior colliculus (**g-i**), by local topology analysis. The branch point density in all these brain structures was significantly higher in the Nogo-A deficient animals than that in the WT control animals. This same increase can be observed in the P60 WT group, when compared to the P10 WT animals, and is most pronounced at the level of capillaries (**c**,**f**,**i**) (n = 4-6 for P10 WT; n = 8-12 for P60 WT; n = 3-5 for P10 Nogo-$A^{-/-}$; n = 8-11 for P60 Nogo-$A^{-/-}$ animals; and in average three ROIs per animal and brain region were used). *P < 0.05, **P < 0.01, ***P < 0.001.

Supplementary Figure 7 Overview of the effects of physiological ageing and of genetic deletion of Nogo-A on the segment density, -diameter, -length, -tortuosity and -volume in various regions of the adult (P60) and postnatal (P10) mouse brain

a-o Quantification of segment density, -diameter, -length, -tortuosity and -volume in the cortex (**a**,**d**,**g**,**j**,**m**), hippocampus (**b**,**e**,**h**,**k**,**n**), and superior colliculus (**c**,**f**,**i**,**l**,**o**), by local topology analysis. The segment density and -tortuosity in all these brain structures was significantly higher in the Nogo-A deficient animals than that in the WT control animals. This same increase can be observed in the P60 WT group, when compared to the P10 WT animals, and is most pronounced at the level of capillaries (**c**,**l**). The parameters segment diameter, -length, and -volume are significantly decreased in the Nogo-A deficient animals as compared to the WT control animals. Here, also this same increase, predominantly at the capillary level (**f**,**i**,**l**) can be observed in the P60 WT group, when compared to the P10 WT animals (n = 4-6 for P10 WT; n = 8-12 for P60 WT; n = 3-5 for P10 Nogo-A$^{-/-}$; n = 8-11 for P60 Nogo-A$^{-/-}$ animals; and in average three ROIs per animal and brain region were used). *P < 0.05, **P < 0.01, ***P < 0.001.

Supplementary Figure 8 Overview of the effects of physiological ageing and of genetic deletion of Nogo-A on the extravascular distance in various regions of the adult (P60) and postnatal (P10) mouse brain

a-c Quantification of the extravascular distance in P10 and P60 in the three brain regions calculated by global morphometry analysis. The extravascular distance in the cortices (**a**), hippocampi (**b**) and superior colliculi (**c**) was lower in the P10 Nogo-A deficient animals than that in the WT control animals, whereas this effect was less obvious in the P60 Nogo-A versus WT (n = 4-6 for P10 WT; n = 8-12 for P60 WT; n = 3-5 for P10 Nogo-$A^{-/-}$; n = 8-11 for P60 Nogo-$A^{-/-}$ animals; and in average three ROIs per animal and brain region were used).

All data are shown as mean distributions where the open dot represents the mean. Boxplots indicate the 25% to 75% quartiles of the data. The shaded blue and red areas indicate the SD. *P<0.05, **P<0.01, ***P<0.001.

Supplementary Figure 9 Local vascular network topology – visualization and quantification of vascular branch point diameter, vascular branch point density and branch point degree in the cortex of the adult (P60) WT versus the postnatal (P10) WT mouse brain

The vascular branch point diameter and vascular branch point density are significantly increased in the P60 as compared to the P10 mouse brain cortex. **a** Scheme depicting the definition of degree 3 and 4 vascular branch point (see Figure 8b for details). **b** Histogram showing the distribution of branch point degree in P10 WT and P60 WT animals. P60 WT animals show an increased branch point degree as compared to P10 WT mice mainly at the capillary level. Of note, nearly all branch points had a degree of 3. Branch point degrees of four or even higher accounted together for far less than 1% of all branch points (bin width = 1; number of bins = 3). **c**,**d** Computational 3D reconstructions of µCT images of cortical vascular networks of P10 WT and P60 WT mice with visualizations of the vessel branch points displayed as dots, separately for non-capillaries (magenta) and capillaries (green) and for branch point degree 3 and 4 where branch points with degree 4 are enlarged and brighter than branch points with degree 3 (also see legend below **d**). The higher density of branch points in the P60 WT cortices especially at the capillary level (green) is obvious, a slight increase of branch point density can be observed at the non-capillary level (magenta). Furthermore, an increase in the branch points with degree 4 can be observed in the P60 WT (**d**) as compared to the P10 WT (**c**) reconstructions. The boxed areas are enlarged at right (**c**,**d**). Quantitative analysis of the branch point degree-3 density for all vessels (**e**), non-capillaries (**f**), and capillaries (**g**) in P10 WT and P60 WT cortices by local morphometry analysis shows that the significant increase in density of branch points with degree-3 for all vessels in P60 WT animals (**e**) was mainly due to a significant increase at the level of capillaries (**g**) and in part due to a significant increase at the level of non-capillaries (**f**). **h-j** The same quantitative analysis for branch point degree-4 (**h-j**) shows that the significant increase of the branch points with degree-4 for all vessels in P60 WT

animals (**h**) was mainly due to a highly significant and very large increase at the level of capillaries (**j**) and in part due to a significant increase at the level of non-capillaries (**i**).

In average, n = 3-12 animals were used for the cortices data; and in average three ROIs per animal were used). All data are shown as mean distributions where the open dot represents the mean. Boxplots indicate the 25% to 75% quartiles of the data. The shaded blue and red areas indicate the SD. *P<0.05, **P<0.01, ***P<0.001. Scale bars: 100 µm (**c**,**d**, overviews); 50 µm (**c**,**d**, zooms).

Supplementary Figure 10 Local vascular network topology – visualization and quantification of vascular branch point diameter, vascular branch point density and branch point degree in the hippocampus in the adult (P60) WT versus the postnatal (P10) mouse brain

The vascular branch point diameter and vascular branch point density are significantly increased in the P60 as compared to P10 mouse brain hippocampus. **a** Scheme depicting the definition of vascular branch points (see Figure 8b for details). **b** Histogram showing the distribution of branch point diameter in P10 WT and P60 WT animals. P60 WT animals show an increased branch point degree as compared to P10 WT mice mainly at the capillary level. Of note, nearly all branch points had a degree of 3. Branch point degrees of four or even higher accounted together for far less than 1% of all branch points (bin width = 1; number of bins = 3). **c**,**d** Computational 3D reconstructions of μCT images of vascular networks of P10 WT and P60 WT mice with visualizations of the vessel branch points displayed as dots, separately for non-capillaries (magenta) and capillaries (green) and for branch point degree 3 and 4 where branch points with degree 4 are enlarged and brighter than branch points with degree 3 (see legend). The higher density of branch points in the P60 WT hippocampi especially at the capillary level (green) is obvious, a slight increase of branch point density can be observed at the non-capillary level (magenta). The boxed areas are enlarged at right (**c**,**d**). Quantitative analysis of the branch point degree-3 density for all vessels (**e**), non-capillaries (**f**), and capillaries (**g**) in P10 WT and P60 WT hippocampi by local morphometry analysis shows that the significant increase in density of branch points with degree-3 for all vessels in the P60 WT animals (**e**) was mainly due to a significant increase at the level of capillaries (**g**) and in part due to a significant increase at the level of non-capillaries (**f**). **h-j** The same quantitative analysis for branch point degree-4 (**h-j**) shows that the significant increase of the branch points with degree-4 for all vessels in the P60 WT animals (**h**) was mainly due to a highly significant and

very large increase at the level of capillaries (**j**) and in part due to a significant increase at the level of non-capillaries (**i**).

In average, n = 2-7 animals were used for the hippocampi; and in average three ROIs per animal and brain region were used. All data are shown as mean distributions where the open dot represents the mean. Boxplots indicate the 25% to 75% quartiles of the data. The shaded blue and red areas indicate the SD. *P<0.05, **P<0.01, ***P<0.001. Scale bars: 100 μm (**c**,**d**, overviews); 50 μm (**c**,**d**, zooms).

Supplementary Figure 11 Local vascular network topology – visualization and quantification of vascular branch point diameter, vascular branch point density and branch point degree in the superior colliculus of the adult (P60) WT versus the postnatal (P10) WT mouse brain.

The vascular branch point diameter and vascular branch point density are significantly increased in the P60 as compared to the P10 mouse brain superior colliculi **a** Scheme depicting the definition of vascular branch points (see Figure 8b for details). **b** Histogram showing the distribution of branch point diameter in P10 WT and P60 WT animals. P60 WT animals show an increased branch point density as compared to P10 WT mice mainly at the capillary level. Of note, nearly all branch points had a degree of 3. Branch point degrees of four or even higher accounted together for far less than 1% of all branch points (bin width = 1; number of bins = 3). **c**,**d** Computational 3D reconstructions of μCT images of vascular networks of P10 WT and P60 WT mice with visualizations of the vessel branch points displayed as dots, separately for non-capillaries (magenta) and capillaries (green) and for branch point degree 3 and 4 where branch points with degree 4 are enlarged and brighter than branch points with degree 3 (see legend). The higher density of branch points in the P60 WT superior colliculi especially at the capillary level (green) is obvious, a slight increase of branch point density can be observed at the non-capillary level (magenta). The boxed areas are enlarged at right. Quantitative analysis of the branch point density for all vessels (**e**), non-capillaries (**f**), and capillaries (**g**) in P10 WT and P60 WT superior colliculi by local morphometry analysis. The significant increase of the branch point density for all vessels in the P60 WT animals (**e**) was mainly due to a significant increase at the level of capillaries (**g**) and in part due to a significant increase at the level of non-capillaries (**f**). **h-j** The same quantitative analysis for branch point degree-4 (**h-j**) shows that the significant increase of the branch points with degree-4 for all vessels in the P60 WT animals (**h**) was mainly due to a highly significant and very large increase at the level of capillaries (**j**) and in part due to a significant increase at the level of non-capillaries (**i**). In average, n = 2-4

animals were used for the superior colliculi; and in average three ROIs per animal and brain region were used. All data are shown as mean distributions where the open dot represents the mean. Boxplots indicate the 25% to 75% quartiles of the data. The shaded blue and red areas indicate the SD. *P<0.05, **P<0.01, ***P<0.001. Scale bars: 100 μm (**c**,**d**, overviews); 50 μm (**c**,**d**, zooms).

Supplementary Figure 12 Global vascular network morphology – visualization of distinct patterns of vessel directionality in the hippocampus and superior colliculus of the adult (P60) WT and postnatal (P10) WT mouse brain

Computational 3D reconstruction of µCT scans of hippocampal and superior colliculi vascular networks of P60 WT displayed with color-coded directionality obtained by attributing every vessel segment to its main direction in the x (red), y (green), and z (blue) planes within the selected ROIs (see Figure 12a for details). **a,b** Computational 3D reconstruction of µCT scans color-coded for vessel directionality depicting the P10 WT (**a**) and P60 WT (**b**) hippocampus. In the hippocampus, horizontally orientated main vessel branches in the x-axis were recognizable, most likely following the distinct curved shape of this anatomical structure. **f**,**g** In the superior colliculus, a comparable pattern of directionality as in the cortex was observed with recognizable INVP vessels radially sprouting into the brain parenchyma along the z-axis. **c-e**,**h-j** Quantitative analysis showing histograms for the distribution of the relative angles of the vascular segments emanating from a certain branch point (segment angle for adjacent vessels) in P10 and P60 animals in the hippocampus (**c-e**), and superior colliculus (**h-j**). Non-capillaries revealed two main angles of orientation, namely around 90° and at around 170° in the three brain regions examined (**d** for hippocampus, **i** for superior colliculus), and these two main angles of orientation were more pronounced at the adult P60 as compared to the developing P10 stage (**d**,**i**), and were very similar in the brain regions, suggesting a more general underlying concept of vessel directionality/orientation. The capillaries derived at angles between around 75° and 150° at both the developing P10 and mature P60 stages in the hippocampus (**e**), and superior colliculus (**j**) (**c-e**,**h-j** bin width = 5; number of bins = 55). Scale bars: 100 µm (**a**,**b**,**f**,**g**).

Supplementary Figure 13 Global vascular network morphology – visualization of distinct patterns of vessel directionality in the cortex of the adult (P60) WT and postnatal (P10) WT mouse brain with a division into capillaries and non-capillaries

a Computational 3D reconstruction of µCT scans of vascular networks of P60 WT displayed with color-coded directionality (see Figure 12 for details). **b-g** Computational 3D reconstruction of µCT scans color-coded for vessel directionality depicting the P10 WT (**b-d**) and P60 WT (**e-g**) cortex. A division was made between all vessels (**b**,**e**), non-capillaries (**c**,**f**), and capillaries (**d**,**g**), defined by an inner diameter of ≥ 7 µm for non-capillaries and < 7µm for capillaries. Cortical renderings clearly showed that the superficial perineural vascular plexus (PNVP) extended in the x- and y-directions, whereas the interneural vascular plexus (INVP) exhibited a radial sprouting pattern into the brain parenchyma along the z-axis, perpendicular to the PNVP, in accordance with literature[28,33,127]. The distinction between non-capillaries and capillaries revealed that the PNVP and INVP were mainly composed of non-capillary vessels (**c**,**f**). Vessel sprouts emanating from the base of these main vessel branches (non-capillaries) of the INVP (and to a lesser extent of the PNVP) in the x-.y-, and z-directions were identified as capillaries. These capillaries vascularized the cortical CNS parenchyma via sprouting from non-capillaries and extended in all directions (x-,y-,z-), thereby assuring adequate micro-vascularization and perfusion of the brain (**d**,**g**). At the adult stage, these patterns of vessel directionality observed at the postnatal developing stage were confirmed and further strengthened. Scale bars: 100 µm (**b-g**).

Supplementary Figure 14 Global vascular network morphology – visualization of distinct patterns of vessel directionality in the hippocampus of the adult (P60) WT and postnatal (P10) WT mouse brain with a division into capillaries and non-capillaries

a Computational 3D reconstruction of µCT scans of vascular networks of P60 WT displayed with color-coded directionality (see Figure 12 for details). **b-g** Computational 3D reconstruction of µCT scans color-coded for vessel directionality depicting the P10 WT (**b-d**) and P60 WT (**e-g**) hippocampus. A division was made between all vessels (**b**,**e**), non-capillaries (**c**,**f**), and capillaries (**d**,**g**), defined by an inner diameter of ≥ 7 µm for non-capillaries and < 7µm for capillaries. In the hippocampus, horizontally orientated main vessel branches in the x-axis were recognizable, most likely following the distinct curved shape of this anatomical structure. Differentiation between non-capillary and capillary vessel structures (**b**,**e**) indicated that these main vessel branches were mainly composed of non-capillary vessels (**c**,**f**). Similar to what we observed in the cortex, vessel sprouts emanating from the base of these main vessel branches (non-capillaries) in the x-, y-, and z-directions were identified as capillaries (**d**,**g**). These capillaries mostly formed the smaller side branches sprouting into the four subregions of the hippocampus proper (CA1, CA2, CA3, dentate gyrus) (**d**,**g**), similar to the human hippocampal vascularization pattern[176,177]. Scale bars: 100 µm (**b-g**).

Supplementary Figure 15 Global vascular network morphology – visualization of distinct patterns of vessel directionality in the superior colliculus of the adult (P60) WT and postnatal (P10) WT mouse brain with a division into capillaries and non-capillaries

a Computational 3D reconstruction of µCT scans of vascular networks of P60 WT displayed with color-coded directionality (see Figure 12 for details). **b-g** Computational 3D reconstruction of µCT scans color-coded for vessel directionality depicting the P10 WT (**b-d**) and P60 WT (**e-g**) cortex. A division was made between all vessels (**b**,**e**), non-capillaries (**c**,**f**), and capillaries (**d**,**g**), defined by an inner diameter of ≥ 7 µm for non-capillaries and < 7µm for capillaries. In the superior colliculus, a comparable pattern of directionality as in the cortex was observed with recognizable INVP vessels radially sprouting into the brain parenchyma along the z-axis. (**c**,**f**). Differentiation between non-capillary and capillary vessel structures (**b**,**e**) indicated that these main vessel branches were mainly composed of non-capillary vessels (**c**,**f**). Similar to what we observed in the cortex, vessel sprouts emanating from the base of these main vessel branches (non-capillaries) in the x-, y-, and z-directions were identified as capillaries (**d**,**g**). Scale bars: 100 µm (**b-g**).

Supplementary Figure 16 Global vascular network morphology – visualization of distinct patterns of vessel directionality in various brain regions of the adult (P60) Nogo-A$^{-/-}$ and postnatal (P10) Nogo-A$^{-/-}$ mouse brain

a Computational 3D reconstruction of µCT scans color-coded for vessel directionality depicting the P10 Nogo-A$^{-/-}$ and P60 Nogo-A$^{-/-}$ cortex (see Figure 12 for details). Cortical renderings clearly show that the superficial perineural vascular plexus (PNVP) extended in the x- and y-directions, whereas the interneural vascular plexus (INVP) exhibited a radial sprouting pattern into the brain parenchyma along the z-axis, perpendicular to the PNVP. **b** In the hippocampus, horizontally orientated main vessel branches in the x-axis were recognizable, most likely following the distinct curved shape of this anatomical structure. **c** In the superior colliculus, a comparable pattern of directionality as in the cortex was observed with recognizable INVP vessels radially sprouting into the brain parenchyma along the z-axis. Scale bars: 100 µm (**b-g**).

Supplementary Figure 17 Whole-brain scan – local vascular network topology – Increased vascular volume fraction of the adult (P60) WT versus postnatal (P10) WT mouse brain mainly found at the capillary level

a-ap Quantification of the 3D vascular volume fraction for all vessels (**a**,**d**,**g**,**j**,**m**,**p**,**s**,**v**,**y**,**ab**,**ae**,**ah**,**ak**,**an**), non-capillaries (**b**,**e**,**h**,**k**,**n**,**q**,**t**,**w**,**z**,**ac**,**af**,**ai**,**al**,**ao**), and capillaries (**c**,**f**,**i**,**l**,**o**,**r**,**u**,**x**,**aa**,**ad**,**ag**,**aj**,**am**,**ap**) in P10 WT and adult (P60) WT mouse brain calculated by local topology analysis in the whole-brain scan. The increase of the vascular volume fraction for all vessels in the P60 WT animals (**a**,**d**,**g**,**m**,**p**,**v**,**y**,**ab**,**ae**,**ah**,**ak**,**an**) was mainly due to a significant increase at the level of capillaries (**c**,**f**,**i**,**l**,**o**,**r**,**u**,**x**,**aa**,**ad**,**ag**,**aj**,**am**,**ap**) in all brain regions (the anatomical regions were divided into ROI-sized section for analysis: between n = 5, dentate gyrus, and n = 126, cortex ROI-sized sections for P10 WT; n = 4, CA3, and n = 76, cortex, ROI-sized sections for P60 WT ROIs were analyzed, highly dependent on the size of the anatomical region). All data are shown as mean distributions where the open dot represents the mean. Boxplots indicate the 25% to 75% quartiles of the data. *P < 0.05, **P < 0.01, ***P < 0.001.

Supplementary Figure 18 Whole-brain scan – local vascular network topology – Increased vascular branch point density in various regions of the adult (P60) WT versus the postnatal (P10) WT mouse brain

a-i Quantitative analysis of the branch point density for all vessels (**a**,**d**,**g**), non-capillaries (**b**,**e**,**h**), and capillaries (**c**,**f**,**i**) in the P10 WT and P60 WT mouse brain calculated by local topology analysis in the whole-brain scan. The significant increase of the branch point density for all vessels in the P60 WT animals (**a**,**d**,**g**) was mainly due to a significant increase at the level of capillaries (**c**,**f**,**i**) and in part due to a significant increase at the level of non-capillaries (**b**,**e**,**h**) (between n = 5, dentate gyrus, and n = 126, cortex ROI-sized sections for P10 WT; and n = 4, CA3, and n = 76, cortex, ROI-sized sections for P60 WT ROIs were analyzed, highly dependent on the size of the anatomical region). All data are shown as mean distributions where the open dot represents the mean. Boxplots indicate the 25% to 75% quartiles of the data. *P<0.05, **P<0.01, ***P<0.001.

Supplementary Figure 19 Whole-brain scan – local vascular network topology – segment density, -diameter, -length, -tortuosity, and -volume of the adult (P60) WT versus the postnatal (P10) WT mouse brain

a-l Quantification of the 3D vessel network parameters segment density (**a-c**), segment diameter (**d-f**), segment length (**g-i**), and segment tortuosity (**j-l**) for all vessels, non-capillaries, and capillaries in P10 WT and P60 WT cortices calculated by local morphometry analysis of the whole-brain scan. The segment density (**a**) and segment tortuosity (**j**) were significantly increased for all vessels in the cortices of P60 WT mice as compared to the P10 WT mice, whereas the segment diameter (**d**) and segment length (**g**) were significantly decreased for all vessels in the P60 WT mice as compared to the P10 WT mice. In line with the other parameters, these differences were mainly due to a highly significant increase respectively decrease at the level of capillaries (**c**,**f**,**i**,**l**) and in part due to an increase respectively decrease at the level of non-capillaries (**b**,**e**,**h**,**k**) (n = 126 ROI-sized sections for the P10 WT cortex; n = 76 for P60 WT cortex were analyzed). All data are shown as mean distributions where the open dot represents the mean. Boxplots indicate the 25% to 75% quartiles of the data. *P < 0.05, **P < 0.01, ***P < 0.001.

Supplementary Figure 20 Whole-brain scan – local vascular network topology – extravascular distance is decreased in various regions of the adult (P60) WT versus the postnatal (P10) WT mouse brain

a-f Color map indicating the extravascular distance in the cortices, hippocampi and superior colliculi of P10 WT and P60 WT mice. Each voxel outside a vessel structure is assigned a color to depict its shortest distance to the nearest vessel structure. The reduced extravascular distance in P10 WT animals as compared to the P60 WT animals is obvious. The color bar indicates the shortest distance to the next vessel structure. **g-i** Quantification of the extravascular distance in P10 WT and P60 WT in the three brain regions calculated by global morphometry analysis. The extravascular distance in the cortices (**g**), and superior colliculi (**i**) of P60 WT animals was significantly decreased as compared to the P10 WT animals. For the hippocampi (**h**) this difference was not significant (n = 1 for P10 WT; n = 1 for P60 WT animals were used; between n = 5, dentate gyrus, and n = 126, cortex ROI-sized sections for P10 WT; and between n = 4, CA3, and n = 76, cortex, ROI-sized sections for P60 WT ROIs were analyzed, highly dependent on the size of the anatomical region). All data are shown as mean distributions where the open dot represents the mean. Boxplots indicate the 25% to 75% quartiles of the data. *P<0.05, **P<0.01, ***P<0.001.

Supplementary Figure 21 Whole-brain scan – Quantification of vessel directionality

Quantitative analysis showing the relative angles of the vascular segments emanating from a certain branch point in the cortex, hippocampus, and superior colliculus on the level of all vessels, non-capillaries and capillaries. **a-i** Analysis revealed that, comparable to the all-vessels group, the capillaries in the cortex, hippocampus, and superior colliculus, derived at angles between around 75° and 150° at both the developing P10 and mature P60 stages (**c**,**f**,**i**). The non-capillaries, showed two main angles of orientation, namely around 90° and at around 170° in three brain regions examined (**b**,**e**,**h**). These two main angles of orientation were more pronounced at the P60 stage as compared to the P10 stage (**b**,**e**,**h**), and were very similar in the three brain regions, suggesting a more general underlying concept of vessel directionality/orientation. These findings, obtained from the whole-brain scans, show very similar findings to the ROI-based method (see Figure 12) (**a-i** bin width = 5; number of bins = 55).

SUPPLEMENTARY VIDEO LEGENDS

Supplementary Video 1 Intracardial resin perfusion of a postnatal (P10) wildtype mouse

This video shows the intracardial resin perfusion of a postnatal (P10) wildtype mouse pub. All steps are precisely explained in the “PROCEDURE” part of this manuscript.

Supplementary Video 2 Three-dimensional animation a reconstructed SRμCT scan of the entire vascular brain corrosion cast of an adult (P60) wildtype mouse

This animation shows a reconstructed SRμCT of an entire brain vascular corrosion cast of an adult (P60) wildtype animal. Five anatomical regions (cortex, hippocampus, superior colliculus, thalamus and cerebellum) were zoomed into with high resolution. Artificial coloring illustrates the vessel radius and the division between capillaries (vessel diameter <7 μm) and non-capillaries (vessel diameter ≥7 μm).

REFERENCES

1 Carmeliet, P. & Jain, R. K. Molecular mechanisms and clinical applications of angiogenesis. *Nature* **473**, 298-307, doi:10.1038/nature10144 (2011).

2 Potente, M., Gerhardt, H. & Carmeliet, P. Basic and therapeutic aspects of angiogenesis. *Cell* **146**, 873-887, doi:10.1016/j.cell.2011.08.039 (2011).

3 Walchli, T. *et al.* Wiring the Vascular Network with Neural Cues: A CNS Perspective. *Neuron* **87**, 271-296, doi:10.1016/j.neuron.2015.06.038 (2015).

4 Jain, R. K. & Carmeliet, P. SnapShot: Tumor angiogenesis. *Cell* **149**, 1408-1408.e1401, doi:10.1016/j.cell.2012.05.025 (2012).

5 Herbert, S. P. & Stainier, D. Y. Molecular control of endothelial cell behaviour during blood vessel morphogenesis. *Nat Rev Mol Cell Biol* **12**, 551-564, doi:10.1038/nrm3176 (2011).

6 Quaegebeur, A., Lange, C. & Carmeliet, P. The neurovascular link in health and disease: molecular mechanisms and therapeutic implications. *Neuron* **71**, 406-424, doi:10.1016/j.neuron.2011.07.013 (2011).

7 Burri, P. H., Hlushchuk, R. & Djonov, V. Intussusceptive angiogenesis: Its emergence, its characteristics, and its significance. *Developmental Dynamics* **231**, 474-488, doi:10.1002/dvdy.20184 (2004).

8 Makanya, A. N., Hlushchuk, R. & Djonov, V. G. Intussusceptive angiogenesis and its role in vascular morphogenesis, patterning, and remodeling. *Angiogenesis* **12**, 113-123, doi:10.1007/s10456-009-9129-5 (2009).

9 Garcia-Gomez, P. & Valiente, M. Vascular co-option in brain metastasis. *Angiogenesis*, doi:10.1007/s10456-019-09693-x (2019).

10 Kuczynski, E. A., Vermeulen, P. B., Pezzella, F., Kerbel, R. S. & Reynolds, A. R. Vessel co-option in cancer. *Nat Rev Clin Oncol* **16**, 469-493, doi:10.1038/s41571-019-0181-9 (2019).

11 Angara, K., Borin, T. F. & Arbab, A. S. Vascular Mimicry: A Novel Neovascularization Mechanism Driving Anti-Angiogenic Therapy (AAT) Resistance in Glioblastoma. *Transl Oncol* **10**, 650-660, doi:10.1016/j.tranon.2017.04.007 (2017).

12 Fernández-Cortés, M., Delgado-Bellido, D. & Oliver, F. J. Vasculogenic Mimicry: Become an Endothelial Cell "But Not So Much". *Front Oncol* **9**, 803-803, doi:10.3389/fonc.2019.00803 (2019).

13 Ricci-Vitiani, L. *et al.* Tumour vascularization via endothelial differentiation of glioblastoma stem-like cells. *Nature* **468**, 824-828, doi:10.1038/nature09557 (2010).

14 Wang, R. *et al.* Glioblastoma stem-like cells give rise to tumour endothelium. *Nature* **468**, 829-833, doi:10.1038/nature09624 (2010).

15 Cheng, L. *et al.* Glioblastoma stem cells generate vascular pericytes to support vessel function and tumor growth. *Cell* **153**, 139-152, doi:10.1016/j.cell.2013.02.021 (2013).

16 Zhou, W. *et al.* Targeting Glioma Stem Cell-Derived Pericytes Disrupts the Blood-Tumor Barrier and Improves Chemotherapeutic Efficacy. *Cell stem cell* **21**, 591-603.e594, doi:10.1016/j.stem.2017.10.002 (2017).

17 Coelho-Santos, V. & Shih, A. Y. Postnatal development of cerebrovascular structure and the neurogliovascular unit. *Wiley Interdiscip Rev Dev Biol* **9**, e363-e363, doi:10.1002/wdev.363 (2020).

18 Mink, J. W., Blumenschine, R. J. & Adams, D. B. Ratio of central nervous system to body metabolism in vertebrates: its constancy and functional basis. *American Journal of Physiology-Regulatory, Integrative and Comparative Physiology* **241**, R203-R212, doi:10.1152/ajpregu.1981.241.3.R203 (1981).

19 Begley, D. J. & Brightman, M. W. Structural and functional aspects of the blood-brain barrier. *Prog Drug Res* **61**, 39-78, doi:10.1007/978-3-0348-8049-7_2 (2003).

20 Zlokovic, B. V. & Apuzzo, M. L. Strategies to circumvent vascular barriers of the central nervous system. *Neurosurgery* **43**, 877-878, doi:10.1097/00006123-199810000-00089 (1998).
21 Cassot, F., Lauwers, F., Lorthois, S., Puwanarajah, P. & Duvernoy, H. Scaling laws for branching vessels of human cerebral cortex. *Microcirculation* **16**, 331-344, 332 p following 344, doi:10.1080/10739680802662607 (2009).
22 Tsai, P. S. *et al.* Correlations of neuronal and microvascular densities in murine cortex revealed by direct counting and colocalization of nuclei and vessels. *J Neurosci* **29**, 14553-14570, doi:10.1523/jneurosci.3287-09.2009 (2009).
23 Blinder, P. *et al.* The cortical angiome: an interconnected vascular network with noncolumnar patterns of blood flow. *Nat Neurosci* **16**, 889-897, doi:10.1038/nn.3426 (2013).
24 Shih, A. Y. *et al.* Robust and fragile aspects of cortical blood flow in relation to the underlying angioarchitecture. *Microcirculation (New York, N.Y. : 1994)* **22**, 204-218, doi:10.1111/micc.12195 (2015).
25 Harb, R., Whiteus, C., Freitas, C. & Grutzendler, J. In vivo imaging of cerebral microvascular plasticity from birth to death. *J Cereb Blood Flow Metab* **33**, 146-156, doi:10.1038/jcbfm.2012.152 (2013).
26 Iadecola, C. The Neurovascular Unit Coming of Age: A Journey through Neurovascular Coupling in Health and Disease. *Neuron* **96**, 17-42, doi:10.1016/j.neuron.2017.07.030 (2017).
27 Vallon, M., Chang, J., Zhang, H. & Kuo, C. J. Developmental and pathological angiogenesis in the central nervous system. *Cellular and molecular life sciences : CMLS* **71**, 3489-3506, doi:10.1007/s00018-014-1625-0 (2014).
28 Walchli, T. *et al.* Quantitative assessment of angiogenesis, perfused blood vessels and endothelial tip cells in the postnatal mouse brain. *Nature protocols* **10**, 53-74, doi:10.1038/nprot.2015.002 (2015).
29 Weller, R. O., Sharp, M. M., Christodoulides, M., Carare, R. O. & Møllgård, K. The meninges as barriers and facilitators for the movement of fluid, cells and pathogens related to the rodent and human CNS. *Acta Neuropathologica* **135**, 363-385, doi:10.1007/s00401-018-1809-z (2018).
30 Hogan, K. A., Ambler, C. A., Chapman, D. L. & Bautch, V. L. The neural tube patterns vessels developmentally using the VEGF signaling pathway. *Development* **131**, 1503-1513, doi:10.1242/dev.01039 (2004).
31 Paredes, I., Himmels, P. & Ruiz de Almodovar, C. Neurovascular Communication during CNS Development. *Dev Cell* **45**, 10-32, doi:10.1016/j.devcel.2018.01.023 (2018).
32 Mancuso, M. R., Kuhnert, F. & Kuo, C. J. Developmental angiogenesis of the central nervous system. *Lymphat Res Biol* **6**, 173-180, doi:10.1089/lrb.2008.1014 (2008).
33 Fantin, A., Vieira, J. M., Plein, A., Maden, C. H. & Ruhrberg, C. The embryonic mouse hindbrain as a qualitative and quantitative model for studying the molecular and cellular mechanisms of angiogenesis. *Nature protocols* **8**, 418-429 (2013).
34 Vasudevan, A., Long, J. E., Crandall, J. E., Rubenstein, J. L. & Bhide, P. G. Compartment-specific transcription factors orchestrate angiogenesis gradients in the embryonic brain. *Nat Neurosci* **11**, 429-439, doi:10.1038/nn2074 (2008).
35 Fantin, A. *et al.* NRP1 acts cell autonomously in endothelium to promote tip cell function during sprouting angiogenesis. *Blood* **121**, 2352-2362, doi:10.1182/blood-2012-05-424713 (2013).
36 Daneman, R., Zhou, L., Kebede, A. A. & Barres, B. A. Pericytes are required for blood-brain barrier integrity during embryogenesis. *Nature* **468**, 562-566, doi:10.1038/nature09513 (2010).

37 Zeller, K., Vogel, J. & Kuschinsky, W. Postnatal distribution of Glut1 glucose transporter and relative capillary density in blood-brain barrier structures and circumventricular organs during development. *Brain research. Developmental brain research* **91**, 200-208 (1996).
38 Walchli, T. *et al.* Nogo-A is a negative regulator of CNS angiogenesis. *Proc Natl Acad Sci U S A* **110**, E1943-1952, doi:10.1073/pnas.1216203110 (2013).
39 Wälchli, T. *et al.* Nogo-A regulates vascular network architecture in the postnatal brain. *J Cereb Blood Flow Metab* **37**, 614-631 (2017).
40 Whiteus, C., Freitas, C. & Grutzendler, J. Perturbed neural activity disrupts cerebral angiogenesis during a postnatal critical period. *Nature* **505**, 407-411, doi:10.1038/nature12821 (2014).
41 Sweeney, M. D., Ayyadurai, S. & Zlokovic, B. V. Pericytes of the neurovascular unit: key functions and signaling pathways. *Nat Neurosci* **19**, 771-783, doi:10.1038/nn.4288 (2016).
42 Muoio, V., Persson, P. B. & Sendeski, M. M. The neurovascular unit - concept review. *Acta Physiol (Oxf)* **210**, 790-798, doi:10.1111/apha.12250 (2014).
43 Eichmann, A. & Thomas, J. L. Molecular parallels between neural and vascular development. *Cold Spring Harb Perspect Med* **3**, a006551, doi:10.1101/cshperspect.a006551 (2013).
44 Sweeney, M. D., Ayyadurai, S. & Zlokovic, B. V. Pericytes of the neurovascular unit: key functions and signaling pathways. *Nature neuroscience* **19**, 771-783, doi:10.1038/nn.4288 (2016).
45 Yu, P. *et al.* FGF-dependent metabolic control of vascular development. *Nature* **545**, 224-228, doi:10.1038/nature22322 (2017).
46 Li, X., Sun, X. & Carmeliet, P. Hallmarks of Endothelial Cell Metabolism in Health and Disease. *Cell metabolism* **30**, 414-433, doi:10.1016/j.cmet.2019.08.011 (2019).
47 Andrae, J., Gallini, R. & Betsholtz, C. Role of platelet-derived growth factors in physiology and medicine. *Genes Dev* **22**, 1276-1312, doi:10.1101/gad.1653708 (2008).
48 Jih, Y. J. *et al.* Distinct regulation of genes by bFGF and VEGF-A in endothelial cells. *Angiogenesis* **4**, 313-321 (2001).
49 Dong, J. *et al.* Glioma stem cells involved in tumor tissue remodeling in a xenograft model. *J Neurosurg* **113**, 249-260, doi:10.3171/2010.2.Jns09335 (2010).
50 Lawler, J. Thrombospondin-1 as an endogenous inhibitor of angiogenesis and tumor growth. *J Cell Mol Med* **6**, 1-12, doi:10.1111/j.1582-4934.2002.tb00307.x (2002).
51 Lawler, P. R. & Lawler, J. Molecular basis for the regulation of angiogenesis by thrombospondin-1 and -2. *Cold Spring Harb Perspect Med* **2**, a006627, doi:10.1101/cshperspect.a006627 (2012).
52 O'Reilly, M. S. *et al.* Endostatin: an endogenous inhibitor of angiogenesis and tumor growth. *Cell* **88**, 277-285, doi:10.1016/s0092-8674(00)81848-6 (1997).
53 Dhanabal, M. *et al.* Angioarrestin: an antiangiogenic protein with tumor-inhibiting properties. *Cancer Res* **62**, 3834-3841 (2002).
54 Lu, X. *et al.* The netrin receptor UNC5B mediates guidance events controlling morphogenesis of the vascular system. *Nature* **432**, 179-186, doi:10.1038/nature03080 (2004).
55 Sakurai, A., Doçi, C. L. & Gutkind, J. S. Semaphorin signaling in angiogenesis, lymphangiogenesis and cancer. *Cell Res* **22**, 23-32, doi:10.1038/cr.2011.198 (2012).
56 Eilken, H. M. & Adams, R. H. Dynamics of endothelial cell behavior in sprouting angiogenesis. *Curr Opin Cell Biol* **22**, 617-625, doi:10.1016/j.ceb.2010.08.010 (2010).
57 Strilic, B. *et al.* The molecular basis of vascular lumen formation in the developing mouse aorta. *Dev Cell* **17**, 505-515, doi:10.1016/j.devcel.2009.08.011 (2009).

58 Pitulescu, M. E. *et al.* Dll4 and Notch signalling couples sprouting angiogenesis and artery formation. *Nat Cell Biol* **19**, 915-927, doi:10.1038/ncb3555 (2017).
59 Lammert, E. & Axnick, J. Vascular lumen formation. *Cold Spring Harb Perspect Med* **2**, a006619, doi:10.1101/cshperspect.a006619 (2012).
60 Tung, J. J., Tattersall, I. W. & Kitajewski, J. Tips, Stalks, Tubes: Notch-Mediated Cell Fate Determination and Mechanisms of Tubulogenesis during Angiogenesis. *Cold Spring Harb Perspect Med* **2**, a006601, doi:10.1101/cshperspect.a006601 (2012).
61 Wacker, A. & Gerhardt, H. Endothelial development taking shape. *Curr Opin Cell Biol* **23**, 676-685, doi:10.1016/j.ceb.2011.10.002 (2011).
62 Mazzone, M. *et al.* Heterozygous deficiency of PHD2 restores tumor oxygenation and inhibits metastasis via endothelial normalization. *Cell* **136**, 839-851, doi:10.1016/j.cell.2009.01.020 (2009).
63 Dela Paz, N. G., Melchior, B. & Frangos, J. A. Shear stress induces Gα(q/11) activation independently of G protein-coupled receptor activation in endothelial cells. *American journal of physiology. Cell physiology* **312**, C428-C437, doi:10.1152/ajpcell.00148.2016 (2017).
64 Takuwa, N. *et al.* Tumor-suppressive sphingosine-1-phosphate receptor-2 counteracting tumor-promoting sphingosine-1-phosphate receptor-1 and sphingosine kinase 1 - Jekyll Hidden behind Hyde. *Am J Cancer Res* **1**, 460-481 (2011).
65 Mendelson, K., Evans, T. & Hla, T. Sphingosine 1-phosphate signalling. *Development* **141**, 5-9, doi:10.1242/dev.094805 (2014).
66 Gaengel, K. *et al.* The sphingosine-1-phosphate receptor S1PR1 restricts sprouting angiogenesis by regulating the interplay between VE-cadherin and VEGFR2. *Dev Cell* **23**, 587-599, doi:10.1016/j.devcel.2012.08.005 (2012).
67 Jin, Z. G. *et al.* Ligand-independent activation of vascular endothelial growth factor receptor 2 by fluid shear stress regulates activation of endothelial nitric oxide synthase. *Circ Res* **93**, 354-363, doi:10.1161/01.Res.0000089257.94002.96 (2003).
68 Nigro, P., Abe, J. & Berk, B. C. Flow shear stress and atherosclerosis: a matter of site specificity. *Antioxid Redox Signal* **15**, 1405-1414, doi:10.1089/ars.2010.3679 (2011).
69 Baeyens, N. *et al.* Defective fluid shear stress mechanotransduction mediates hereditary hemorrhagic telangiectasia. *Journal of Cell Biology* **214**, 807-816, doi:10.1083/jcb.201603106 (2016).
70 Franco, C. A. *et al.* Non-canonical Wnt signalling modulates the endothelial shear stress flow sensor in vascular remodelling. *Elife* **5**, e07727-e07727, doi:10.7554/eLife.07727 (2016).
71 Pries, A. R. & Secomb, T. W. Modeling structural adaptation of microcirculation. *Microcirculation* **15**, 753-764, doi:10.1080/10739680802229076 (2008).
72 Pries, A. R., Secomb, T. W. & Gaehtgens, P. Structural adaptation and stability of microvascular networks: theory and simulations. *Am J Physiol* **275**, H349-360, doi:10.1152/ajpheart.1998.275.2.H349 (1998).
73 Hjelmeland, A. B., Lathia, J. D., Sathornsumetee, S. & Rich, J. N. Twisted tango: brain tumor neurovascular interactions. *Nat Neurosci* **14**, 1375-1381, doi:10.1038/nn.2955 (2011).
74 Carmeliet, P., De Smet, F., Loges, S. & Mazzone, M. Branching morphogenesis and antiangiogenesis candidates: tip cells lead the way. *Nat Rev Clin Oncol* **6**, 315-326, doi:10.1038/nrclinonc.2009.64 (2009).
75 Frahm, K. A., Nash, C. P. & Tobet, S. A. Endocan immunoreactivity in the mouse brain: method for identifying nonfunctional blood vessels. *J Immunol Methods* **398-399**, 27-32, doi:10.1016/j.jim.2013.09.005 (2013).
76 Geudens, I. & Gerhardt, H. Coordinating cell behaviour during blood vessel formation. *Development* **138**, 4569-4583, doi:10.1242/dev.062323 (2011).

77 Blanco, R. & Gerhardt, H. VEGF and Notch in tip and stalk cell selection. *Cold Spring Harb Perspect Med* **3**, a006569, doi:10.1101/cshperspect.a006569 (2013).
78 Phng, L. K. & Gerhardt, H. Angiogenesis: a team effort coordinated by notch. *Dev Cell* **16**, 196-208, doi:10.1016/j.devcel.2009.01.015 (2009).
79 Noguera-Troise, I. *et al.* Blockade of Dll4 inhibits tumour growth by promoting non-productive angiogenesis. *Nature* **444**, 1032-1037, doi:10.1038/nature05355 (2006).
80 Thurston, G., Noguera-Troise, I. & Yancopoulos, G. D. The Delta paradox: DLL4 blockade leads to more tumour vessels but less tumour growth. *Nat Rev Cancer* **7**, 327-331, doi:10.1038/nrc2130 (2007).
81 Yan, M. *et al.* Chronic DLL4 blockade induces vascular neoplasms. *Nature* **463**, E6-7, doi:10.1038/nature08751 (2010).
82 Lobov, I. B. *et al.* Delta-like ligand 4 (Dll4) is induced by VEGF as a negative regulator of angiogenic sprouting. *Proc Natl Acad Sci U S A* **104**, 3219-3224, doi:10.1073/pnas.0611206104 (2007).
83 Ridgway, J. *et al.* Inhibition of Dll4 signalling inhibits tumour growth by deregulating angiogenesis. *Nature* **444**, 1083-1087, doi:10.1038/nature05313 (2006).
84 Adamson, S. L. *et al.* Interactions between trophoblast cells and the maternal and fetal circulation in the mouse placenta. *Dev Biol* **250**, 358-373, doi:10.1016/s0012-1606(02)90773-6 (2002).
85 Gest, T. R. & Carron, M. A. Embryonic origin of the caudal mesenteric artery in the mouse. *Anat Rec A Discov Mol Cell Evol Biol* **271**, 192-201, doi:10.1002/ar.a.10022 (2003).
86 Iwagaki, T., Suzuki, T. & Nakashima, T. Development and regression of cochlear blood vessels in fetal and newborn mice. *Hear Res* **145**, 75-81, doi:10.1016/s0378-5955(00)00075-7 (2000).
87 Carraro, M. & Harrison, R. V. Degeneration of stria vascularis in age-related hearing loss; a corrosion cast study in a mouse model. *Acta Otolaryngol* **136**, 385-390, doi:10.3109/00016489.2015.1123291 (2016).
88 Carraro, M., Park, A. H. & Harrison, R. V. Partial corrosion casting to assess cochlear vasculature in mouse models of presbycusis and CMV infection. *Hear Res* **332**, 95-103, doi:10.1016/j.heares.2015.11.010 (2016).
89 Carraro, M. *et al.* Cytomegalovirus (CMV) Infection Causes Degeneration of Cochlear Vasculature and Hearing Loss in a Mouse Model. *J Assoc Res Otolaryngol* **18**, 263-273, doi:10.1007/s10162-016-0606-4 (2017).
90 Hossler, F. E., Lametschwandtner, A., Kao, R. & Finsterbusch, F. Microvascular architecture of mouse urinary bladder described with vascular corrosion casting, light microscopy, SEM, and TEM. *Microsc Microanal* **19**, 1428-1435, doi:10.1017/S143192761301341X (2013).
91 Peão, M. N., Aguas, A. P., de Sá, C. M. & Grande, N. R. Neoformation of blood vessels in association with rat lung fibrosis induced by bleomycin. *Anat Rec* **238**, 57-67, doi:10.1002/ar.1092380108 (1994).
92 Peáo, M. N., Aguas, A. P., de Sá, C. M. & Grande, N. R. Identification of vascular sphincters at the junction between alveolar capillaries and pulmonary venules of the mouse lung. *Anat Rec* **241**, 383-390, doi:10.1002/ar.1092410313 (1995).
93 Ackermann, M. *et al.* Effects of nintedanib on the microvascular architecture in a lung fibrosis model. *Angiogenesis* **20**, 359-372, doi:10.1007/s10456-017-9543-z (2017).
94 Gibney, B. C. *et al.* Structural and functional evidence for the scaffolding effect of alveolar blood vessels. *Exp Lung Res* **43**, 337-346, doi:10.1080/01902148.2017.1368739 (2017).
95 Dahl, E. The fine structure of intracerebral vessels. *Z Zellforsch Mikrosk Anat* **145**, 577-586, doi:10.1007/bf00306725 (1973).

96 Levesque, M. J., Cornhill, J. F. & Nerem, R. M. Vascular casting. A new method for the study of the arterial endothelium. *Atherosclerosis* **34**, 457-467, doi:10.1016/0021-9150(79)90070-4 (1979).
97 Duvernoy, H. M., Delon, S. & Vannson, J. L. Cortical blood vessels of the human brain. *Brain Res Bull* **7**, 519-579, doi:10.1016/0361-9230(81)90007-1 (1981).
98 Reina-De La Torre, F., Rodriguez-Baeza, A. & Sahuquillo-Barris, J. Morphological characteristics and distribution pattern of the arterial vessels in human cerebral cortex: a scanning electron microscope study. *Anat Rec* **251**, 87-96, doi:10.1002/(SICI)1097-0185(199805)251:1<87::AID-AR14>3.0.CO;2-7 (1998).
99 Zagórska-Swiezy, K., Litwin, J. A., Gorczyca, J., Pityński, K. & Miodoński, A. J. Arterial supply and venous drainage of the choroid plexus of the human lateral ventricle in the prenatal period as revealed by vascular corrosion casts and SEM. *Folia Morphol (Warsz)* **67**, 209-213 (2008).
100 Heinzer, S. *et al.* Hierarchical microimaging for multiscale analysis of large vascular networks. *Neuroimage* **32**, 626-636, doi:10.1016/j.neuroimage.2006.03.043 (2006).
101 Krucker, T., Lang, A. & Meyer, E. P. New polyurethane-based material for vascular corrosion casting with improved physical and imaging characteristics. *Microsc Res Tech* **69**, 138-147, doi:10.1002/jemt.20263 (2006).
102 Sangiorgi, S. *et al.* Arterial and microvascular supply of cerebral hemispheres in the nude mouse revealed using corrosion casting and scanning electron microscopy. *Journal of anatomy* **232**, 739-746, doi:10.1111/joa.12791 (2018).
103 Quintana, D. D. *et al.* The cerebral angiome: High resolution MicroCT imaging of the whole brain cerebrovasculature in female and male mice. *NeuroImage* **202**, 116109, doi:10.1016/j.neuroimage.2019.116109 (2019).
104 Heinzer, S. *et al.* Novel three-dimensional analysis tool for vascular trees indicates complete micro-networks, not single capillaries, as the angiogenic endpoint in mice overexpressing human VEGF(165) in the brain. *Neuroimage* **39**, 1549-1558, doi:10.1016/j.neuroimage.2007.10.054 (2008).
105 Krucker, T., Schuler, A., Meyer, E. P., Staufenbiel, M. & Beckmann, N. Magnetic resonance angiography and vascular corrosion casting as tools in biomedical research: application to transgenic mice modeling Alzheimer's disease. *Neurol Res* **26**, 507-516, doi:10.1179/016164104225016281 (2004).
106 Meyer, E. P., Ulmann-Schuler, A., Staufenbiel, M. & Krucker, T. Altered morphology and 3D architecture of brain vasculature in a mouse model for Alzheimer's disease. *Proc Natl Acad Sci U S A* **105**, 3587-3592, doi:10.1073/pnas.0709788105 (2008).
107 Walker, E. J., Shen, F., Young, W. L. & Su, H. Cerebrovascular casting of the adult mouse for 3D imaging and morphological analysis. *J Vis Exp*, e2958-e2958, doi:10.3791/2958 (2011).
108 Walker, E. J. *et al.* Arteriovenous malformation in the adult mouse brain resembling the human disease. *Ann Neurol* **69**, 954-962, doi:10.1002/ana.22348 (2011).
109 Risser, L. *et al.* From homogeneous to fractal normal and tumorous microvascular networks in the brain. *Journal of cerebral blood flow and metabolism : official journal of the International Society of Cerebral Blood Flow and Metabolism* **27**, 293-303, doi:10.1038/sj.jcbfm.9600332 (2007).
110 Sangiorgi, S. *et al.* Early-stage microvascular alterations of a new model of controlled cortical traumatic brain injury: 3D morphological analysis using scanning electron microscopy and corrosion casting. **118**, 763, doi:10.3171/2012.11.Jns12627 (2013).
111 Ohtake, M., Morino, S., Kaidoh, T. & Inoué, T. Three-dimensional structural changes in cerebral microvessels after transient focal cerebral ischemia in rats: scanning electron microscopic study of corrosion casts. *Neuropathology* **24**, 219-227, doi:10.1111/j.1440-1789.2004.00560.x (2004).

112 Rodríguez-Baeza, A., Reina-de la Torre, F., Poca, A., Martí, M. & Garnacho, A. Morphological features in human cortical brain microvessels after head injury: a three-dimensional and immunocytochemical study. *Anat Rec A Discov Mol Cell Evol Biol* **273**, 583-593, doi:10.1002/ar.a.10069 (2003).
113 Zhang, F., Wen, Y. & Guo, X. CRISPR/Cas9 for genome editing: progress, implications and challenges. *Hum Mol Genet* **23**, R40-46, doi:10.1093/hmg/ddu125 (2014).
114 Gerhardt, H. *et al.* Neuropilin-1 is required for endothelial tip cell guidance in the developing central nervous system. *Dev Dyn* **231**, 503-509, doi:10.1002/dvdy.20148 (2004).
115 Gerhardt, H. *et al.* VEGF guides angiogenic sprouting utilizing endothelial tip cell filopodia. *J Cell Biol* **161**, 1163-1177, doi:10.1083/jcb.200302047 (2003).
116 Provost, J. *et al.* 3-D ultrafast Doppler imaging applied to the noninvasive mapping of blood vessels in vivo. *IEEE Trans Ultrason Ferroelectr Freq Control* **62**, 1467-1472, doi:10.1109/TUFFC.2015.007032 (2015).
117 Demene, C. *et al.* 4D microvascular imaging based on ultrafast Doppler tomography. *Neuroimage* **127**, 472-483, doi:10.1016/j.neuroimage.2015.11.014 (2016).
118 Pathak, A. P., Kim, E., Zhang, J. & Jones, M. V. Three-dimensional imaging of the mouse neurovasculature with magnetic resonance microscopy. *PLoS One* **6**, e22643-e22643, doi:10.1371/journal.pone.0022643 (2011).
119 Hartung, M. P., Grist, T. M. & François, C. J. Magnetic resonance angiography: current status and future directions. *J Cardiovasc Magn Reson* **13**, 19-19, doi:10.1186/1532-429X-13-19 (2011).
120 Kelch, I. D. *et al.* Organ-wide 3D-imaging and topological analysis of the continuous microvascular network in a murine lymph node. *Sci Rep* **5**, 16534, doi:10.1038/srep16534 (2015).
121 Marien, K. M. *et al.* Development and Validation of a Histological Method to Measure Microvessel Density in Whole-Slide Images of Cancer Tissue. *PLoS One* **11**, e0161496-e0161496, doi:10.1371/journal.pone.0161496 (2016).
122 Bukenya, F., Nerissa, C., Serres, S., Pardon, M. C. & Bai, L. An automated method for segmentation and quantification of blood vessels in histology images. *Microvasc Res* **128**, 103928, doi:10.1016/j.mvr.2019.103928 (2020).
123 Oren, R. *et al.* Whole Organ Blood and Lymphatic Vessels Imaging (WOBLI). *Scientific reports* **8**, 1412-1412, doi:10.1038/s41598-018-19663-w (2018).
124 Kennel, P., Teyssedre, L., Colombelli, J. & Plouraboué, F. Toward quantitative three-dimensional microvascular networks segmentation with multiview light-sheet fluorescence microscopy. *J Biomed Opt* **23**, 1-14, doi:10.1117/1.Jbo.23.8.086002 (2018).
125 Di Giovanna, A. P. *et al.* Tailored Sample Mounting for Light-Sheet Fluorescence Microscopy of Clarified Specimens by Polydimethylsiloxane Casting. *Frontiers in neuroanatomy* **13**, 35-35, doi:10.3389/fnana.2019.00035 (2019).
126 Lugo-Hernandez, E. *et al.* 3D visualization and quantification of microvessels in the whole ischemic mouse brain using solvent-based clearing and light sheet microscopy. *J Cereb Blood Flow Metab* **37**, 3355-3367, doi:10.1177/0271678x17698970 (2017).
127 Todorov, M. I. *et al.* Machine learning analysis of whole mouse brain vasculature. *Nat Methods* **17**, 442-449, doi:10.1038/s41592-020-0792-1 (2020).
128 Kirst, C. *et al.* Mapping the Fine-Scale Organization and Plasticity of the Brain Vasculature. *Cell* **180**, 780-795.e725, doi:10.1016/j.cell.2020.01.028 (2020).
129 Susaki, E. A. & Ueda, H. R. Whole-body and Whole-Organ Clearing and Imaging Techniques with Single-Cell Resolution: Toward Organism-Level Systems Biology in Mammals. *Cell Chem Biol* **23**, 137-157, doi:10.1016/j.chembiol.2015.11.009 (2016).

130 Zagorchev, L. *et al.* Micro computed tomography for vascular exploration. *J Angiogenes Res* **2**, 7, doi:10.1186/2040-2384-2-7 (2010).
131 Blery, P. *et al.* Vascular imaging with contrast agent in hard and soft tissues using microcomputed-tomography. *Journal of Microscopy* **262**, 40-49, doi:10.1111/jmi.12339 (2016).
132 Starosolski, Z. *et al.* Ultra High-Resolution In vivo Computed Tomography Imaging of Mouse Cerebrovasculature Using a Long Circulating Blood Pool Contrast Agent. *Scientific Reports* **5**, 10178, doi:10.1038/srep10178 (2015).
133 Beckmann, N. *et al.* Age-dependent cerebrovascular abnormalities and blood flow disturbances in APP23 mice modeling Alzheimer's disease. *J Neurosci* **23**, 8453-8459 (2003).
134 Gore, A. V., Monzo, K., Cha, Y. R., Pan, W. & Weinstein, B. M. Vascular development in the zebrafish. *Cold Spring Harb Perspect Med* **2**, a006684, doi:10.1101/cshperspect.a006684 (2012).
135 Dorr, A., Sled, J. G. & Kabani, N. Three-dimensional cerebral vasculature of the CBA mouse brain: a magnetic resonance imaging and micro computed tomography study. *Neuroimage* **35**, 1409-1423, doi:10.1016/j.neuroimage.2006.12.040 (2007).
136 Figueiredo, G., Boll, H., Kramer, M., Groden, C. & Brockmann, M. A. In Vivo X-Ray Digital Subtraction and CT Angiography of the Murine Cerebrovasculature Using an Intra-Arterial Route of Contrast Injection. *American Journal of Neuroradiology* **33**, 1702, doi:10.3174/ajnr.A3071 (2012).
137 Ben-Zvi, A. *et al.* Mfsd2a is critical for the formation and function of the blood-brain barrier. *Nature* **509**, 507-511, doi:10.1038/nature13324 (2014).
138 Vanlandewijck, M. *et al.* A molecular atlas of cell types and zonation in the brain vasculature. *Nature* **554**, 475-480, doi:10.1038/nature25739 (2018).
139 Kalucka, J. *et al.* Single-Cell Transcriptome Atlas of Murine Endothelial Cells. *Cell* **180**, 764-779.e720, doi:10.1016/j.cell.2020.01.015 (2020).
140 Goveia, J. *et al.* An Integrated Gene Expression Landscape Profiling Approach to Identify Lung Tumor Endothelial Cell Heterogeneity and Angiogenic Candidates. *Cancer Cell* **37**, 21-36.e13, doi:10.1016/j.ccell.2019.12.001 (2020).
141 Pitulescu, M. E., Schmidt, I., Benedito, R. & Adams, R. H. Inducible gene targeting in the neonatal vasculature and analysis of retinal angiogenesis in mice. *Nature protocols* **5**, 1518-1534, doi:10.1038/nprot.2010.113 (2010).
142 Sawamiphak, S., Ritter, M. & Acker-Palmer, A. Preparation of retinal explant cultures to study ex vivo tip endothelial cell responses. *Nature protocols* **5**, 1659-1665, doi:10.1038/nprot.2010.130 (2010).
143 Willner, M. *et al.* Quantitative Three-Dimensional Imaging of Lipid, Protein, and Water Contents via X-Ray Phase-Contrast Tomography. *PLOS ONE* **11**, e0151889, doi:10.1371/journal.pone.0151889 (2016).
144 Moyon, D., Pardanaud, L., Yuan, L., Bréant, C. & Eichmann, A. Plasticity of endothelial cells during arterial-venous differentiation in the avian embryo. *Development* **128**, 3359-3370 (2001).
145 Villa, N. *et al.* Vascular expression of Notch pathway receptors and ligands is restricted to arterial vessels. *Mech Dev* **108**, 161-164, doi:10.1016/s0925-4773(01)00469-5 (2001).
146 Seki, T., Yun, J. & Oh, S. P. Arterial endothelium-specific activin receptor-like kinase 1 expression suggests its role in arterialization and vascular remodeling. *Circ Res* **93**, 682-689, doi:10.1161/01.Res.0000095246.40391.3b (2003).
147 Cui, X. *et al.* Venous Endothelial Marker COUP-TFII Regulates the Distinct Pathologic Potentials of Adult Arteries and Veins. *Scientific Reports* **5**, 16193, doi:10.1038/srep16193 (2015).

148 You, L. R. *et al.* Suppression of Notch signalling by the COUP-TFII transcription factor regulates vein identity. *Nature* **435**, 98-104, doi:10.1038/nature03511 (2005).
149 Wang, H. U., Chen, Z. F. & Anderson, D. J. Molecular distinction and angiogenic interaction between embryonic arteries and veins revealed by ephrin-B2 and its receptor Eph-B4. *Cell* **93**, 741-753 (1998).
150 Malcontenti-Wilson, C., Chan, L., Nikfarjam, M., Muralidharan, V. & Christophi, C. Vascular targeting agent Oxi4503 inhibits tumor growth in a colorectal liver metastases model. *J Gastroenterol Hepatol* **23**, e96-e104, doi:10.1111/j.1440-1746.2007.04899.x (2008).
151 Kaidoh, T., Yasugi, T. & Uehara, Y. The microvasculature of the 7,12-dimethylbenz(a)anthracene (DMBA)-induced rat mammary tumour. *Virchows Archiv A* **418**, 111-117, doi:10.1007/BF01600286 (1991).
152 Chakhoyan, A. *et al.* Validation of vessel size imaging (VSI) in high-grade human gliomas using magnetic resonance imaging, image-guided biopsies, and quantitative immunohistochemistry. *Scientific Reports* **9**, 2846, doi:10.1038/s41598-018-37564-w (2019).
153 Burrell, J. S. *et al.* MRI measurements of vessel calibre in tumour xenografts: Comparison with vascular corrosion casting. *Microvascular Research* **84**, 323-329, doi:https://doi.org/10.1016/j.mvr.2012.08.001 (2012).
154 O'Connor, J. P. *et al.* Quantifying antivascular effects of monoclonal antibodies to vascular endothelial growth factor: insights from imaging. *Clin Cancer Res* **15**, 6674-6682, doi:10.1158/1078-0432.Ccr-09-0731 (2009).
155 Miyake, T., Murakami, T. & Ohtsuka, A. Incomplete vascular casting for a scanning electron microscope study of the microcirculatory patterns in the rat pancreas. *Arch Histol Cytol* **55**, 397-406, doi:10.1679/aohc.55.397 (1992).
156 Christoffersonm, R. H. & Nilsson, B. O. Microvascular corrosion casting with analysis in the scanning electron microscope. *Scanning* **10**, 43-63, doi:10.1002/sca.4950100202 (1988).
157 Paganin, D., Mayo, S. C., Gureyev, T. E., Miller, P. R. & Wilkins, S. W. Simultaneous phase and amplitude extraction from a single defocused image of a homogeneous object. *Journal of Microscopy* **206**, 33-40, doi:10.1046/j.1365-2818.2002.01010.x (2002).
158 Marone, F. & Stampanoni, M. Regridding reconstruction algorithm for real-time tomographic imaging. *J Synchrotron Radiat* **19**, 1029-1037, doi:10.1107/s0909049512032864 (2012).
159 Miettinen, A., Oikonomidis, I. V., Bonnin, A. & Stampanoni, M. NRStitcher: non-rigid stitching of terapixel-scale volumetric images. *Bioinformatics* **35**, 5290-5297, doi:10.1093/bioinformatics/btz423 (2019).
160 Otsu, N. A Threshold Selection Method from Gray-Level Histograms. *IEEE Transactions on Systems, Man, and Cybernetics* **9**, 62-66, doi:10.1109/TSMC.1979.4310076 (1979).
161 Huang, L.-K. & Wang, M.-J. J. Image thresholding by minimizing the measures of fuzziness. *Pattern Recognition* **28**, 41-51, doi:https://doi.org/10.1016/0031-3203(94)E0043-K (1995).
162 Prewitt, J. M. S. & Mendelsohn, M. L. THE ANALYSIS OF CELL IMAGES*. *Annals of the New York Academy of Sciences* **128**, 1035-1053, doi:10.1111/j.1749-6632.1965.tb11715.x (1966).
163 Li, C. H. & Tam, P. K. S. An iterative algorithm for minimum cross entropy thresholding. *Pattern Recogn. Lett.* **19**, 771–776, doi:10.1016/s0167-8655(98)00057-9 (1998).

164 Lee, T. C., Kashyap, R. L. & Chu, C. N. Building Skeleton Models via 3-D Medial Surface Axis Thinning Algorithms. *CVGIP: Graphical Models and Image Processing* **56**, 462-478, doi:https://doi.org/10.1006/cgip.1994.1042 (1994).
165 Calvin R. Maurer, J., Qi, R. & Raghavan, V. A Linear Time Algorithm for Computing Exact Euclidean Distance Transforms of Binary Images in Arbitrary Dimensions. *IEEE Trans. Pattern Anal. Mach. Intell.* **25**, 265-270, doi:10.1109/tpami.2003.1177156 (2003).
166 Suhadolnik, A., Petrišič, J. & Kosel, F. An anchored discrete convolution algorithm for measuring length in digital images. *Measurement* **42**, 1112-1117, doi:https://doi.org/10.1016/j.measurement.2009.04.005 (2009).
167 Tukey, J. W. *Exploratory data analysis*. (Addison-Wesley Pub. Co., 1977).
168 ACSF for LSPS. *Cold Spring Harbor Protocols* **2012**, pdb.rec071944, doi:10.1101/pdb.rec071944 (2012).
169 Heinzer, S. *et al. Computer-based analysis of microvascular alterations in a mouse model for Alzheimer's disease*. Vol. 6511 (Proc. SPIE 6511, Medical Imaging 2007: Physiology, Function, and Structure from Medical Images, 651104, 2007).
170 Rust, R. *et al.* Nogo-A targeted therapy promotes vascular repair and functional recovery following stroke. *Proceedings of the National Academy of Sciences* **116**, 14270, doi:10.1073/pnas.1905309116 (2019).
171 Joly, S., Dejda, A., Rodriguez, L., Sapieha, P. & Pernet, V. Nogo-A inhibits vascular regeneration in ischemic retinopathy. *Glia* **66**, 2079-2093, doi:10.1002/glia.23462 (2018).
172 Seiler, S., Di Santo, S. & Widmer, H. R. Nogo-A Neutralization Improves Graft Function in a Rat Model of Parkinson's Disease. *Front Cell Neurosci* **10**, 87, doi:10.3389/fncel.2016.00087 (2016).
173 Weber, B., Keller, A. L., Reichold, J. & Logothetis, N. K. The microvascular system of the striate and extrastriate visual cortex of the macaque. *Cerebral cortex* **18**, 2318-2330, doi:10.1093/cercor/bhm259 (2008).
174 Fenrich, K. K., Zhao, E. Y., Wei, Y., Garg, A. & Rose, P. K. Isolating specific cell and tissue compartments from 3D images for quantitative regional distribution analysis using novel computer algorithms. *J Neurosci Methods* **226**, 42-56, doi:10.1016/j.jneumeth.2014.01.011 (2014).
175 Simonen, M. *et al.* Systemic deletion of the myelin-associated outgrowth inhibitor Nogo-A improves regenerative and plastic responses after spinal cord injury. *Neuron* **38**, 201-211 (2003).
176 Marinkovic, S., Milisavljevic, M. & Puskas, L. Microvascular anatomy of the hippocampal formation. *Surg Neurol* **37**, 339-349, doi:10.1016/0090-3019(92)90001-4 (1992).
177 Tatu, L. & Vuillier, F. Structure and vascularization of the human hippocampus. *Front Neurol Neurosci* **34**, 18-25, doi:10.1159/000356440 (2014).

Figure 1

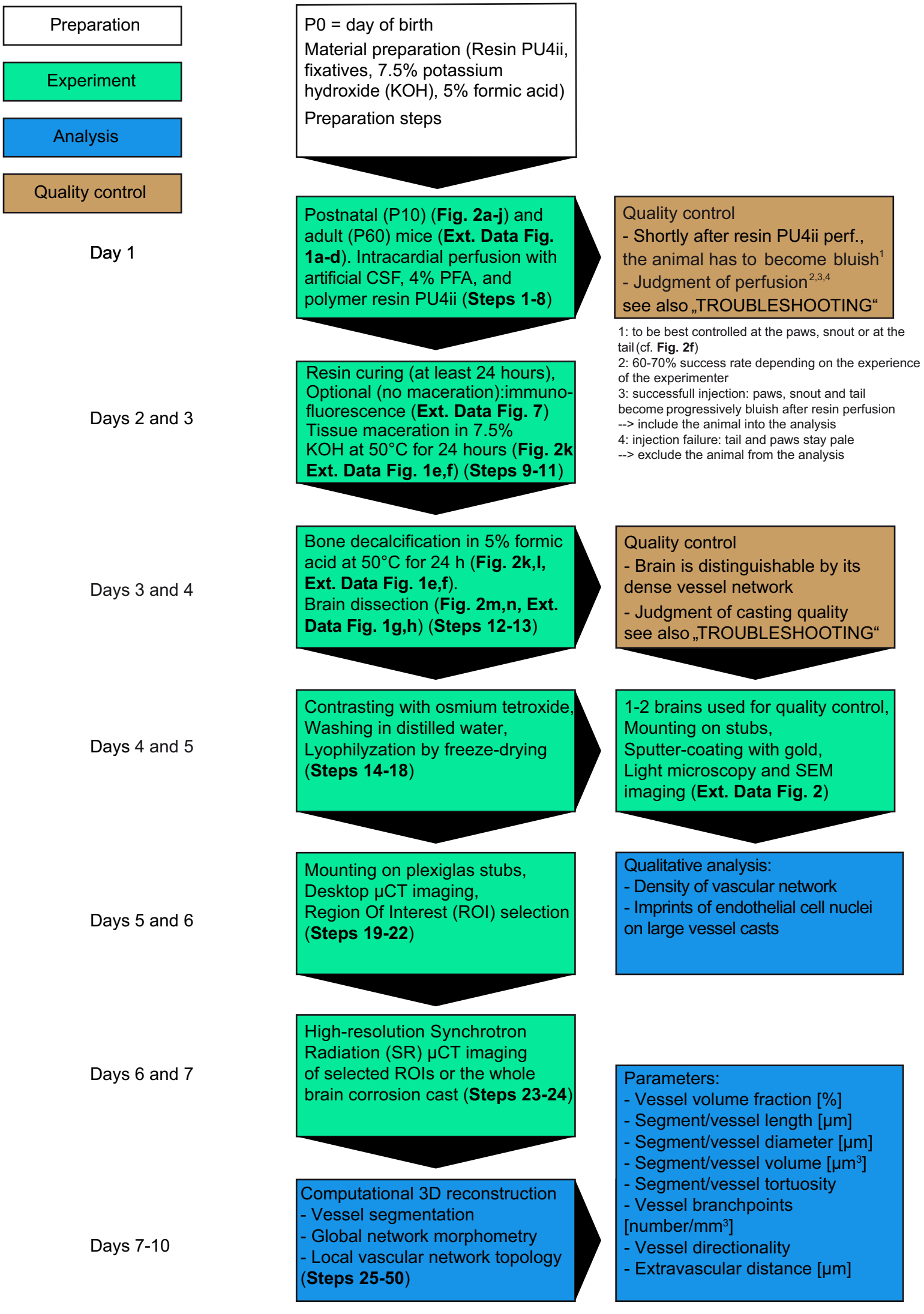
Preparation
Experiment
Analysis
Quality control
P0 = day of birth
Material preparation (Resin PU4ii, fixatives, 7.5% potassium hydroxide (KOH), 5% formic acid)
Preparation steps
Day 1
Postnatal (P10) (Fig. 2a-j) and adult (P60) mice (Ext. Data Fig. 1a-d). Intracardial perfusion with artificial CSF, 4% PFA, and polymer resin PU4ii (Steps 1-8)
Quality control
- Shortly after resin PU4ii perf., the animal has to become bluish[1]
- Judgment of perfusion[2,3,4]
see also „TROUBLESHOOTING“
1: to be best controlled at the paws, snout or at the tail (cf. Fig. 2f)
2: 60-70% success rate depending on the experience of the experimenter
3: successfull injection: paws, snout and tail become progressively bluish after resin perfusion
--> include the animal into the analysis
4: injection failure: tail and paws stay pale
--> exclude the animal from the analysis
Days 2 and 3
Resin curing (at least 24 hours), Optional (no maceration):immuno-fluorescence (Ext. Data Fig. 7)
Tissue maceration in 7.5% KOH at 50°C for 24 hours (Fig. 2k Ext. Data Fig. 1e,f) (Steps 9-11)
Days 3 and 4
Bone decalcification in 5% formic acid at 50°C for 24 h (Fig. 2k,l, Ext. Data Fig. 1e,f).
Brain dissection (Fig. 2m,n, Ext. Data Fig. 1g,h) (Steps 12-13)
Quality control
- Brain is distinguishable by its dense vessel network
- Judgment of casting quality
see also „TROUBLESHOOTING“
Days 4 and 5
Contrasting with osmium tetroxide,
Washing in distilled water,
Lyophilyzation by freeze-drying (Steps 14-18)
1-2 brains used for quality control,
Mounting on stubs,
Sputter-coating with gold,
Light microscopy and SEM imaging (Ext. Data Fig. 2)
Days 5 and 6
Mounting on plexiglas stubs,
Desktop µCT imaging,
Region Of Interest (ROI) selection (Steps 19-22)
Qualitative analysis:
- Density of vascular network
- Imprints of endothelial cell nuclei on large vessel casts
Days 6 and 7
High-resolution Synchrotron Radiation (SR) µCT imaging of selected ROIs or the whole brain corrosion cast (Steps 23-24)
Days 7-10
Computational 3D reconstruction
- Vessel segmentation
- Global network morphometry
- Local vascular network topology
(Steps 25-50)
Parameters:
- Vessel volume fraction [%]
- Segment/vessel length [µm]
- Segment/vessel diameter [µm]
- Segment/vessel volume [µm³]
- Segment/vessel tortuosity
- Vessel branchpoints [number/mm³]
- Vessel directionality
- Extravascular distance [µm]

Figure 2

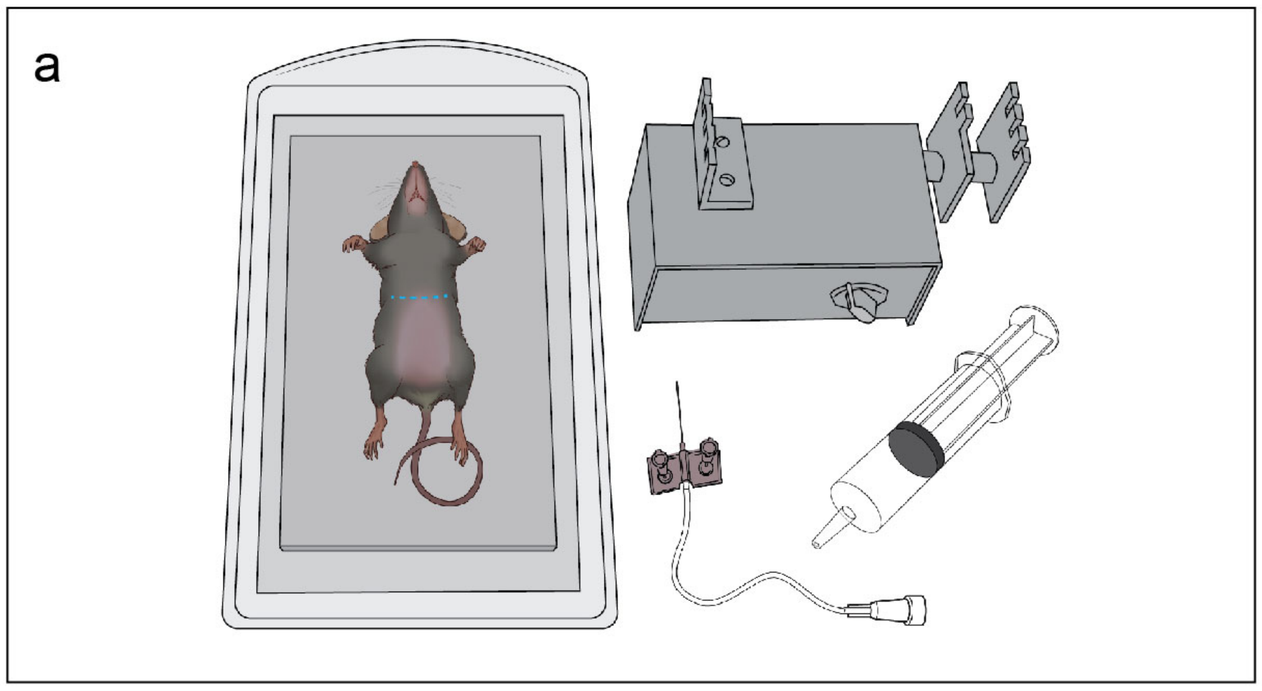

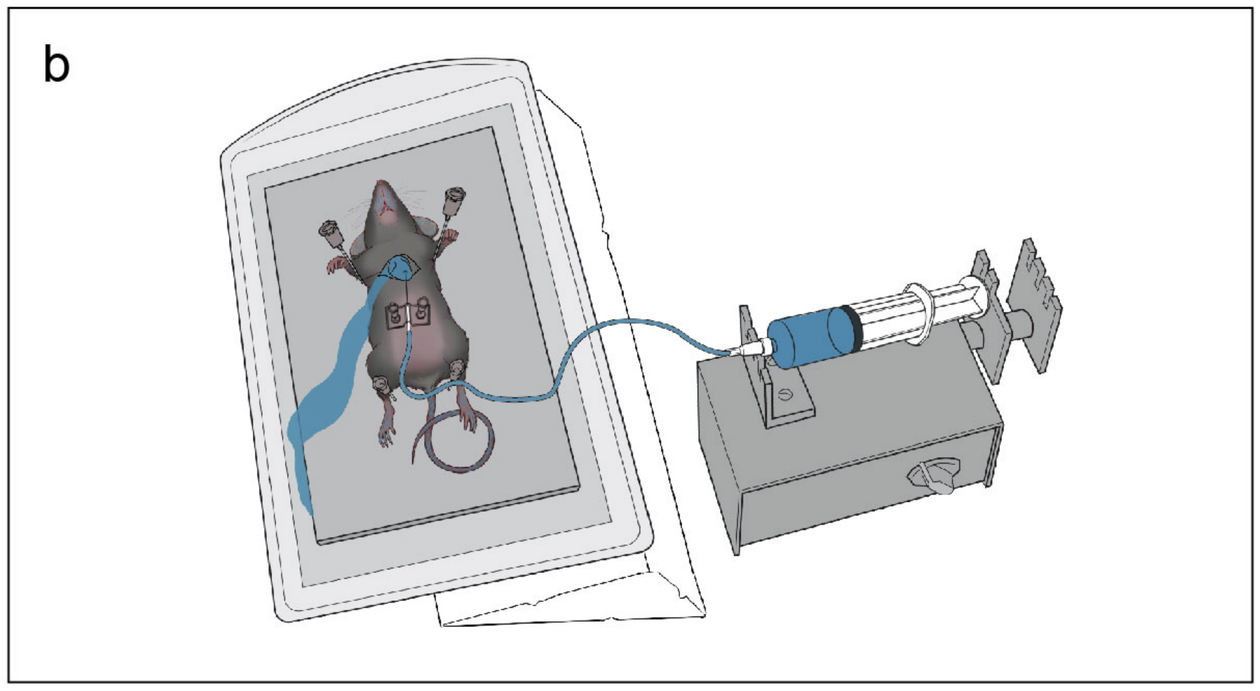

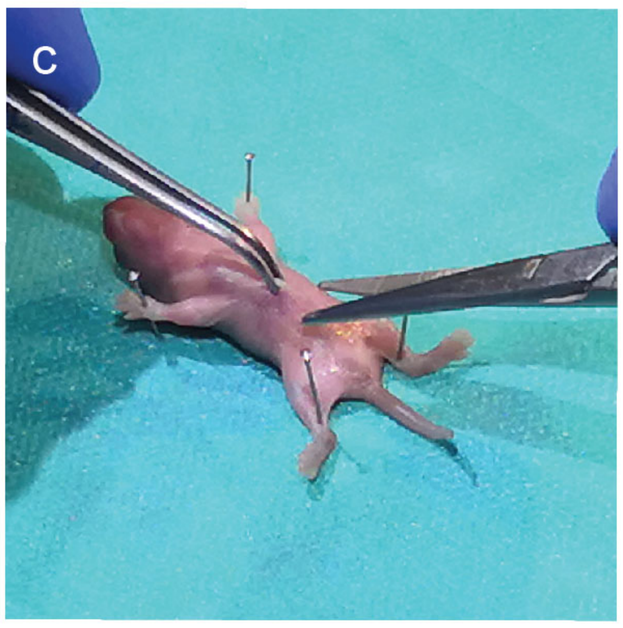

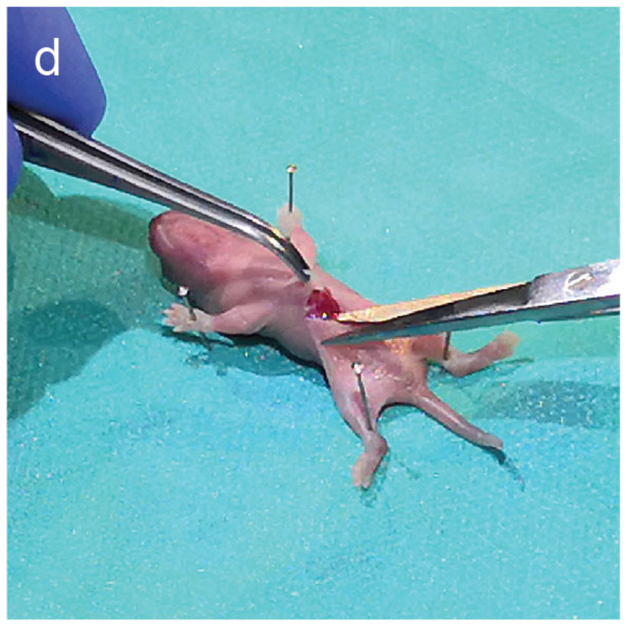

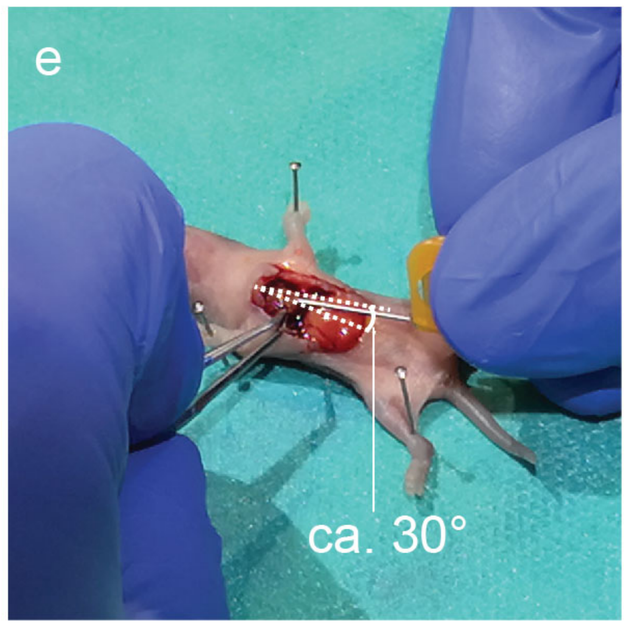

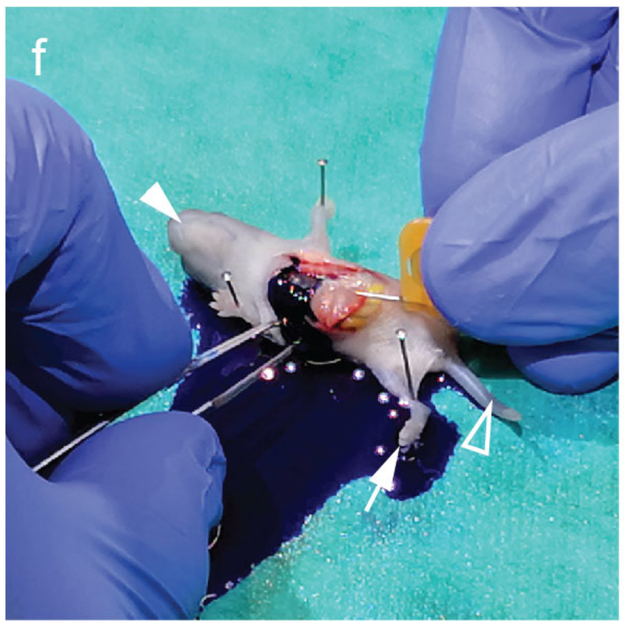

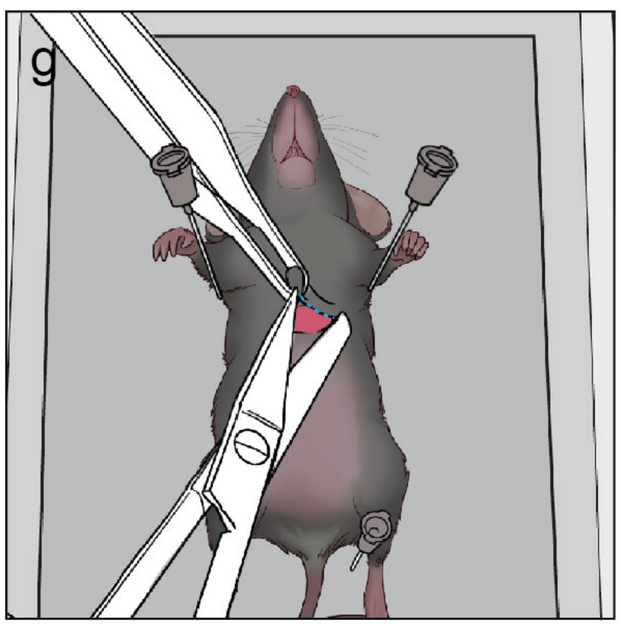

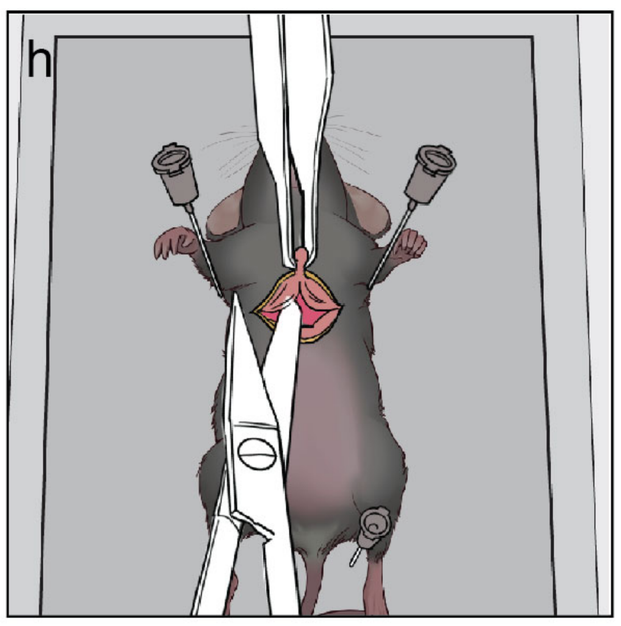

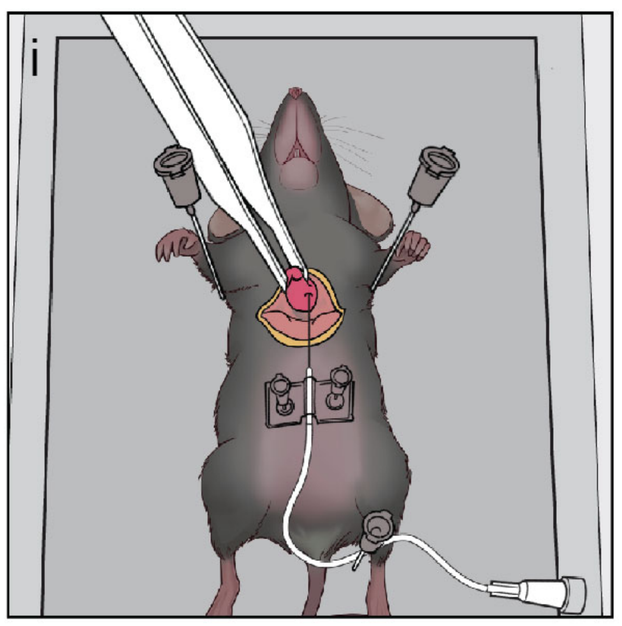

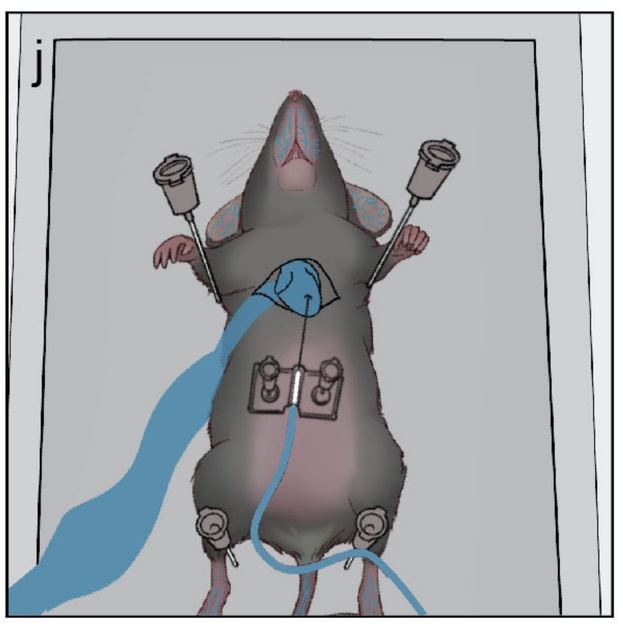

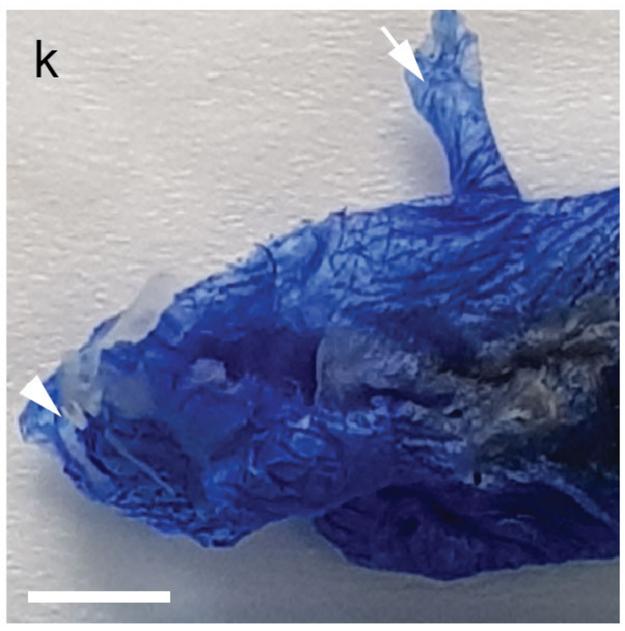

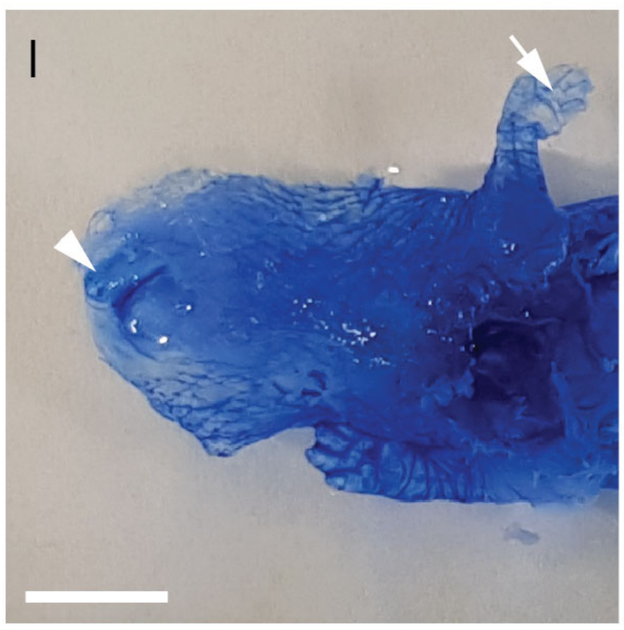

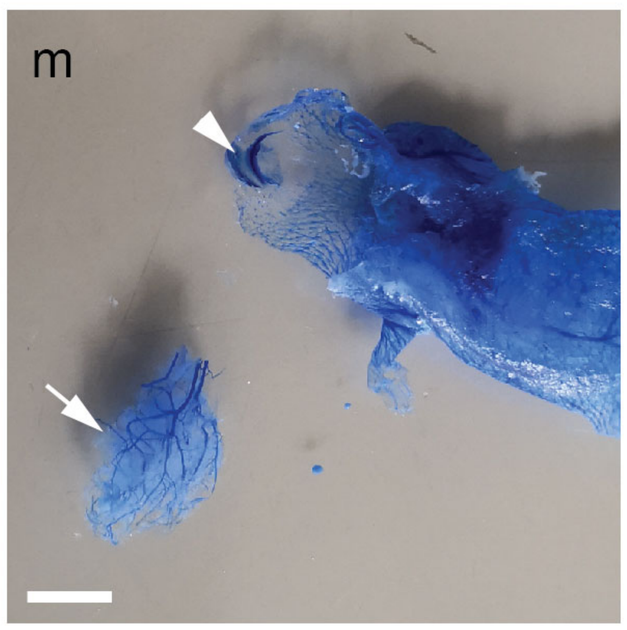

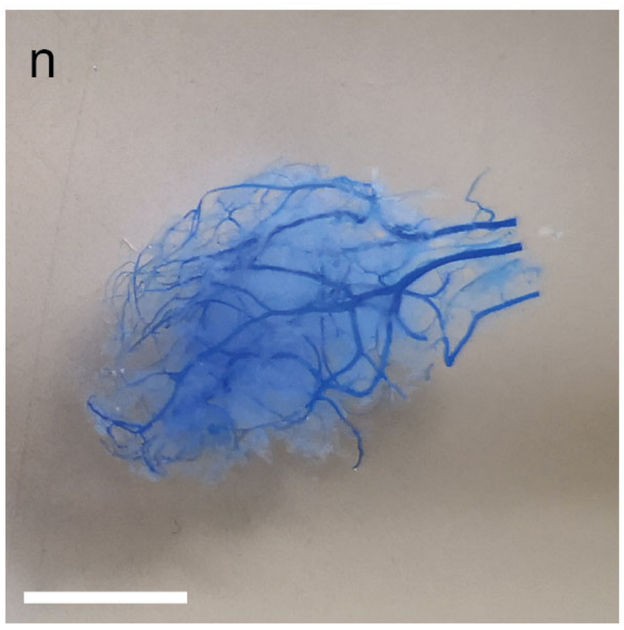

Figure 3

Resin perfused mouse

a



Resin perfused mouse (P60)
(resin and surrounding soft- and bony tissues)

b

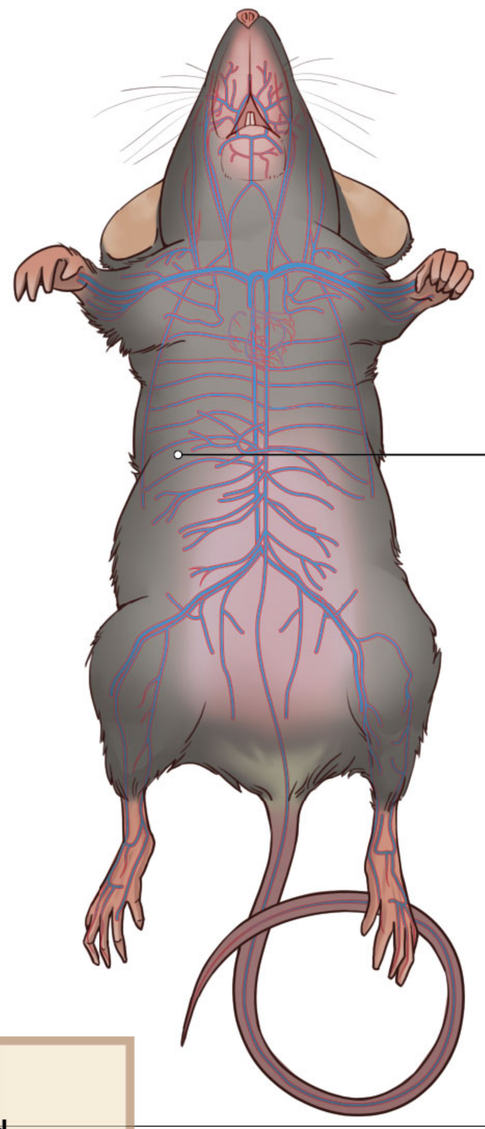

c

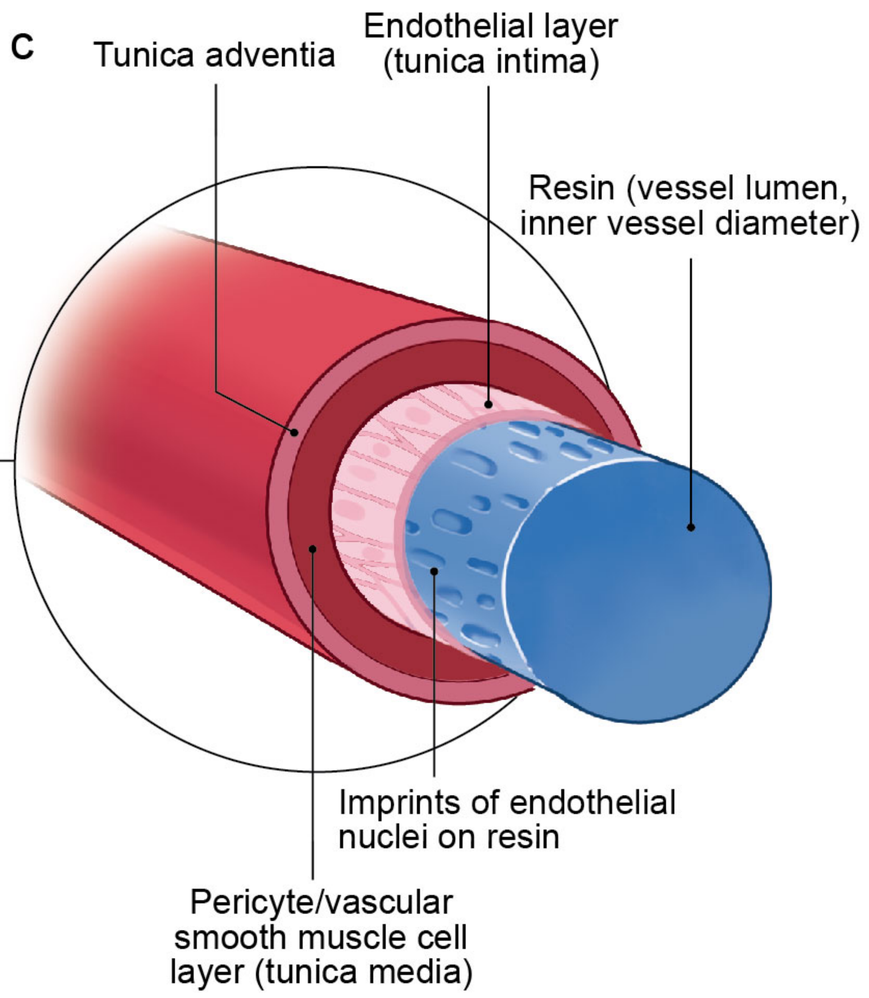

d

Resin and surrounding soft- and bony tissues digested away

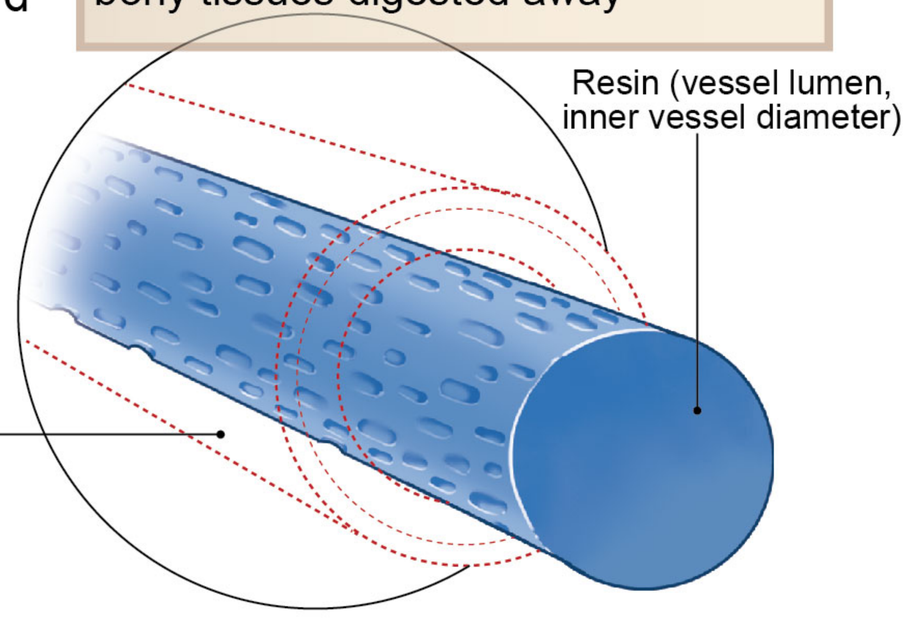

Resin vascular corrosion cast

e



f

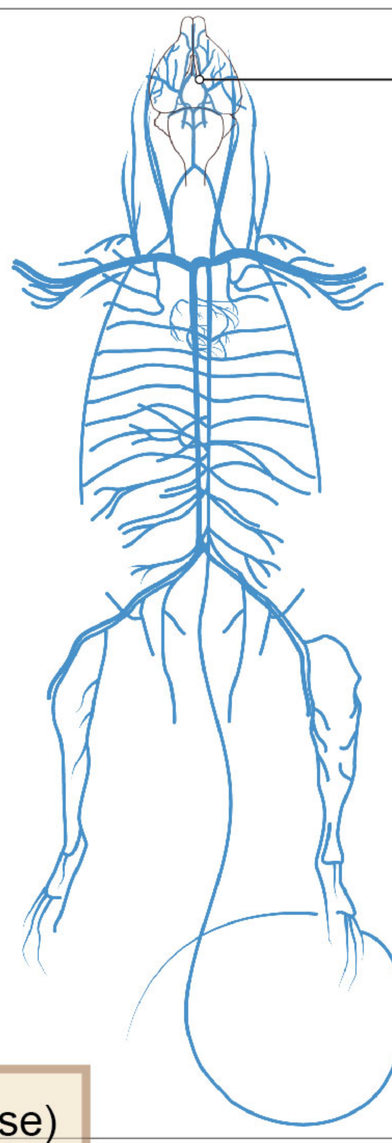

g

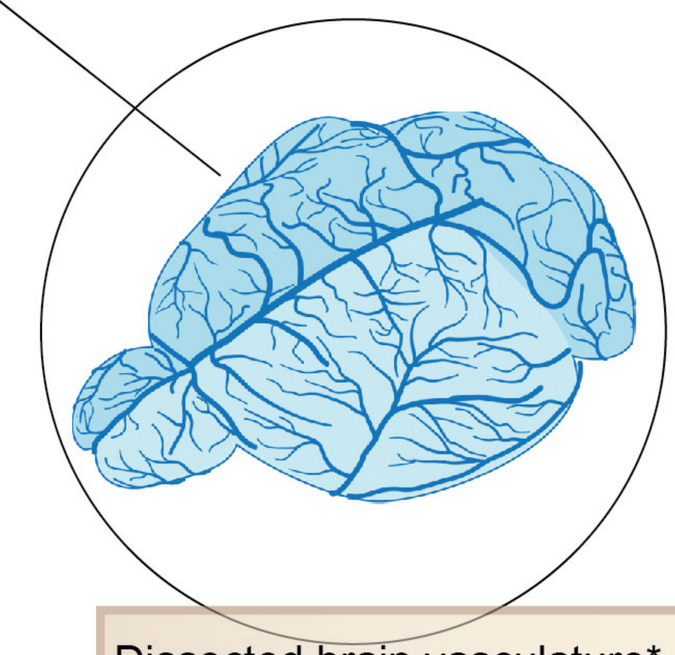

Vascular corrosion cast (P60 mouse)
(resin only, surrounding soft- and bony tissues digested away)

Dissected brain vasculature*
*Any organ of interest can be addressed

Figure 4

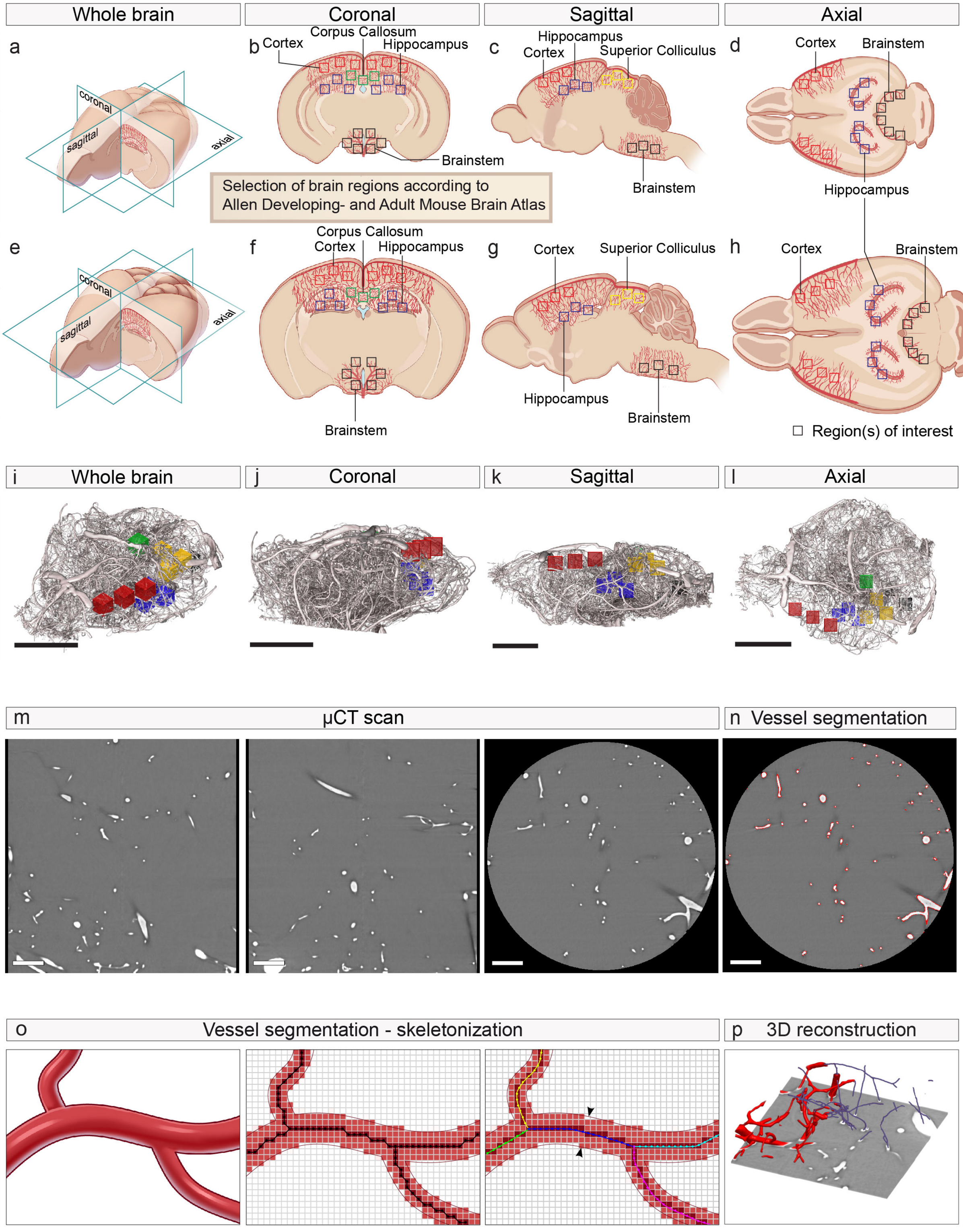
Whole brain
Coronal
Sagittal
Axial
Postnatal (P10)
a
b
c
d
Cortex
Corpus Callosum
Hippocampus
Brainstem
Superior Colliculus
coronal
sagittal
axial
Selection of brain regions according to
Allen Developing- and Adult Mouse Brain Atlas
Adult (P60)
e
f
g
h
i Whole brain
j Coronal
k Sagittal
l Axial
P10 WT
m µCT scan
n Vessel segmentation
P10 WT - Cortex
o Vessel segmentation - skeletonization
p 3D reconstruction
Region(s) of interest

Figure 5

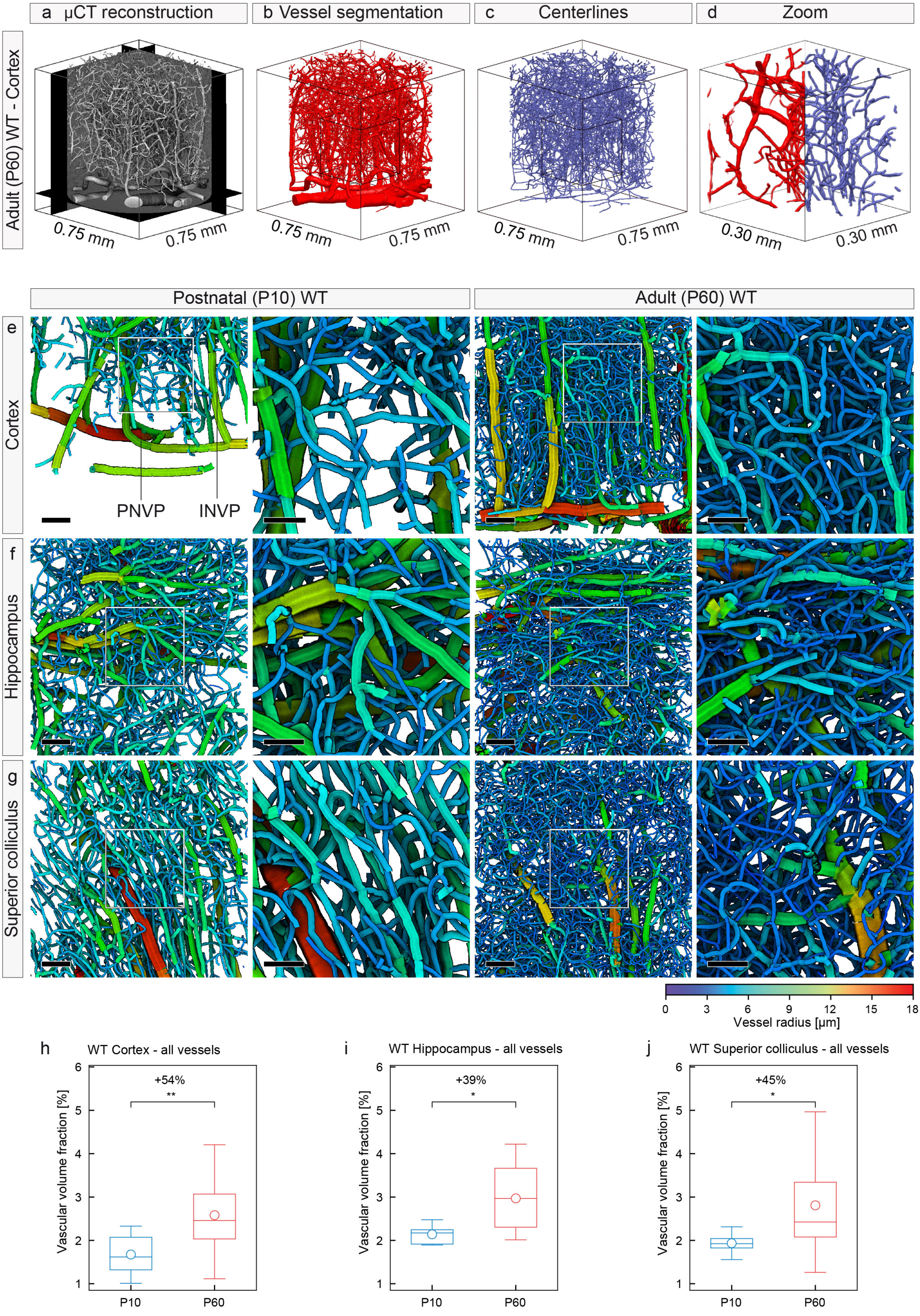
a µCT reconstruction
b Vessel segmentation
c Centerlines
d Zoom
Adult (P60) WT - Cortex
0.75 mm
0.75 mm
0.75 mm
0.75 mm
0.75 mm
0.75 mm
0.30 mm
0.30 mm
Postnatal (P10) WT
Adult (P60) WT
e
Cortex
PNVP
INVP
f
Hippocampus
g
Superior colliculus
0
3
6
9
12
15
18
Vessel radius [µm]
h
WT Cortex - all vessels
+54%
**
Vascular volume fraction [%]
P10
P60
i
WT Hippocampus - all vessels
+39%
*
Vascular volume fraction [%]
P10
P60
j
WT Superior colliculus - all vessels
+45%
*
Vascular volume fraction [%]
P10
P60

Figure 6

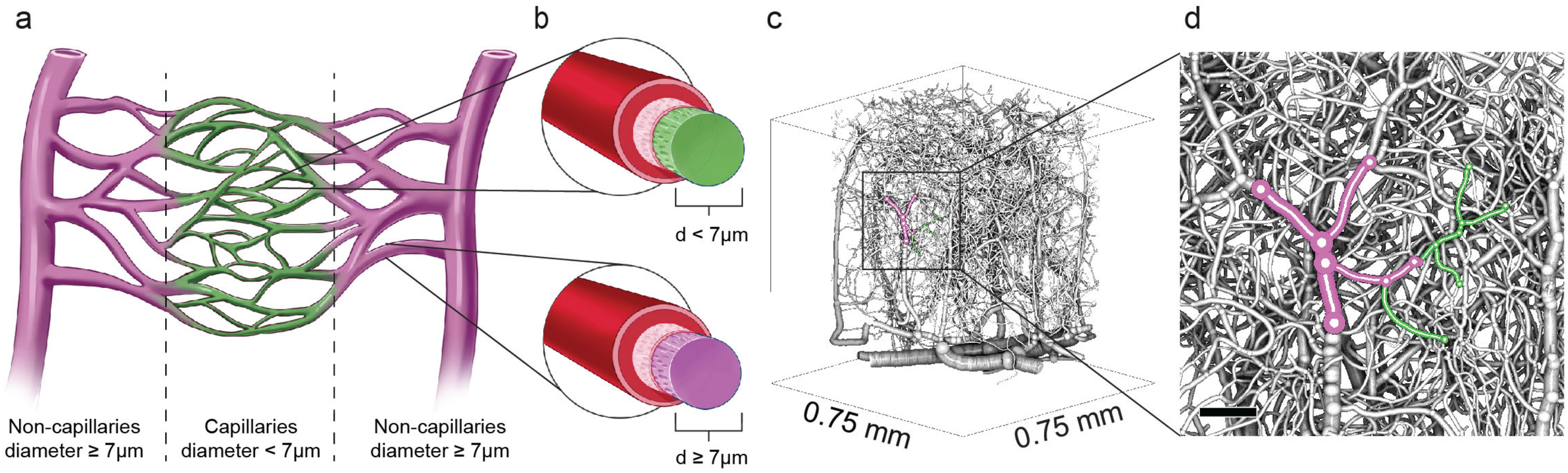
a
b
c
d
Non-capillaries
diameter ≥ 7μm
Capillaries
diameter < 7μm
Non-capillaries
diameter ≥ 7μm
d < 7μm
d ≥ 7μm
0.75 mm
0.75 mm

Figure 7

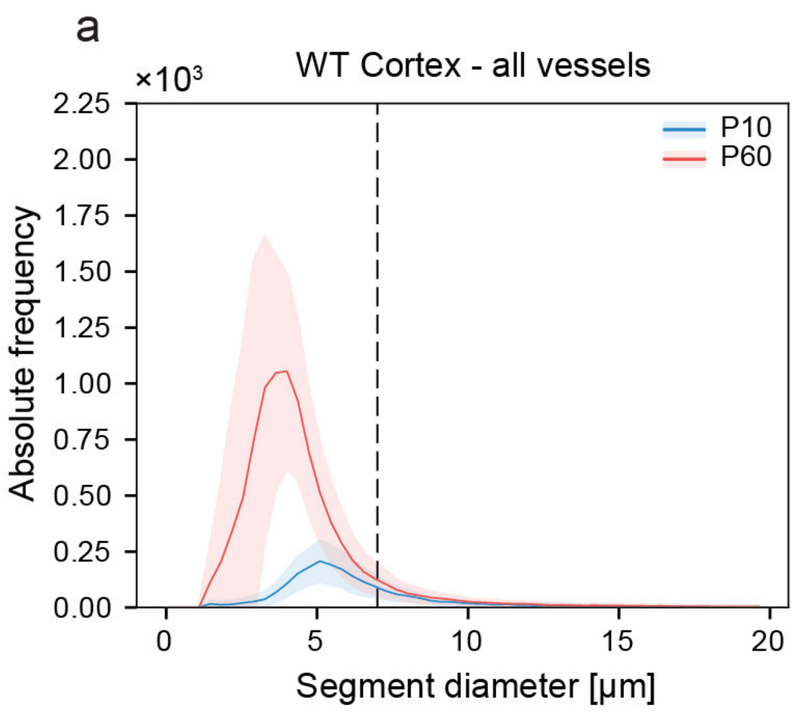
a
WT Cortex - all vessels
×10³
Absolute frequency
Segment diameter [µm]
P10
P60

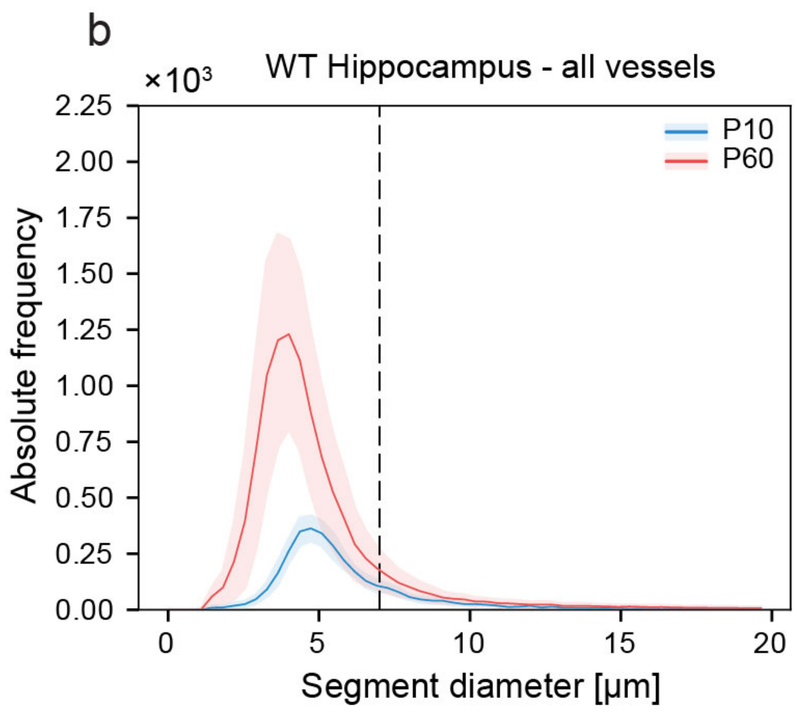
b
WT Hippocampus - all vessels
×10³
Absolute frequency
Segment diameter [µm]
P10
P60

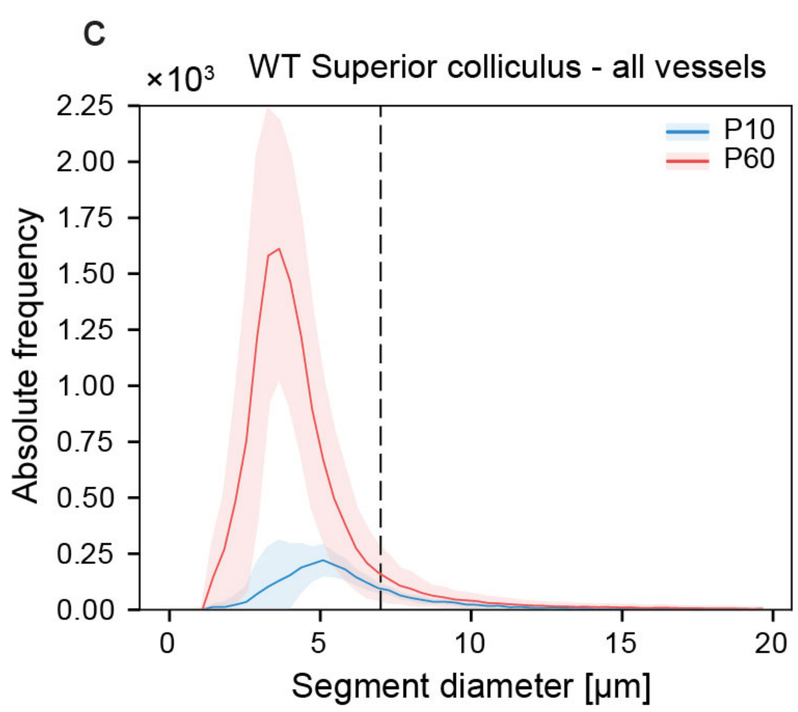
c
WT Superior colliculus - all vessels
×10³
Absolute frequency
Segment diameter [µm]
P10
P60

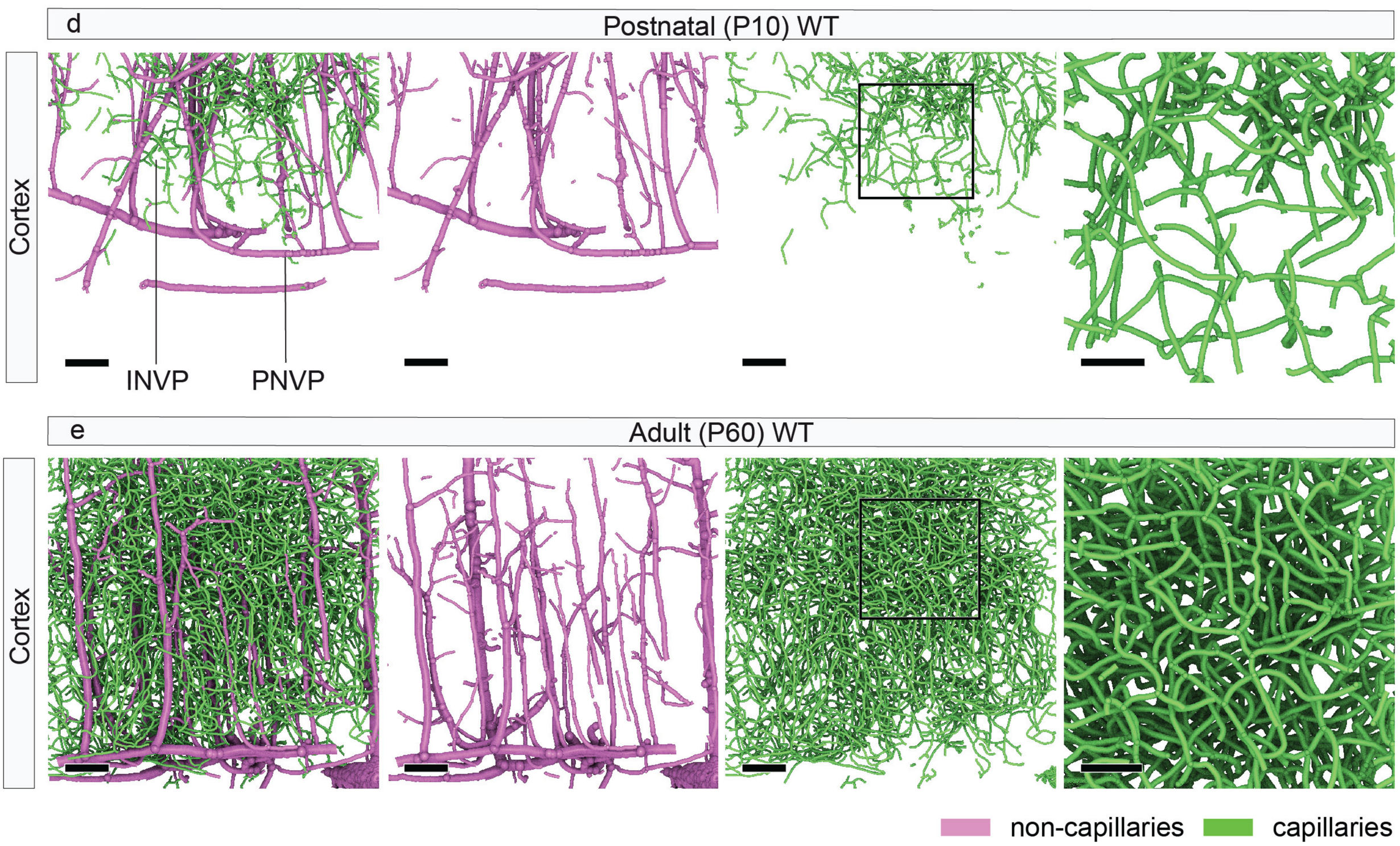
d
Postnatal (P10) WT
Cortex
INVP
PNVP
e
Adult (P60) WT
Cortex
non-capillaries
capillaries

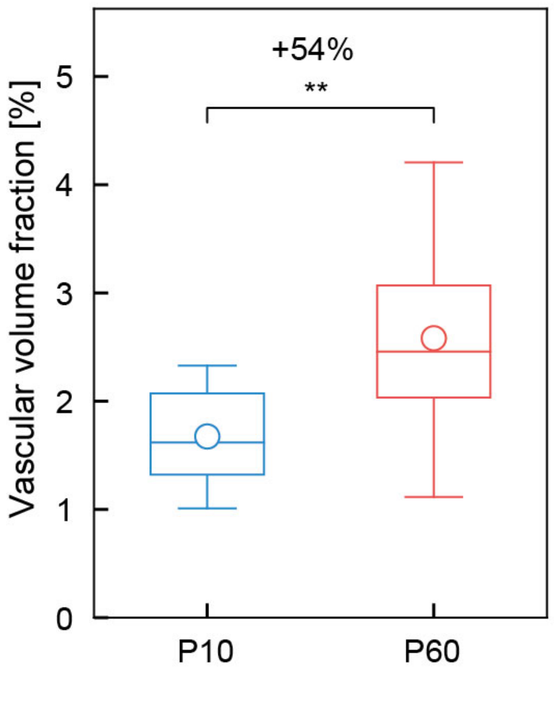
f
WT Cortex - all vessels
Vascular volume fraction [%]
+54%
**
P10
P60

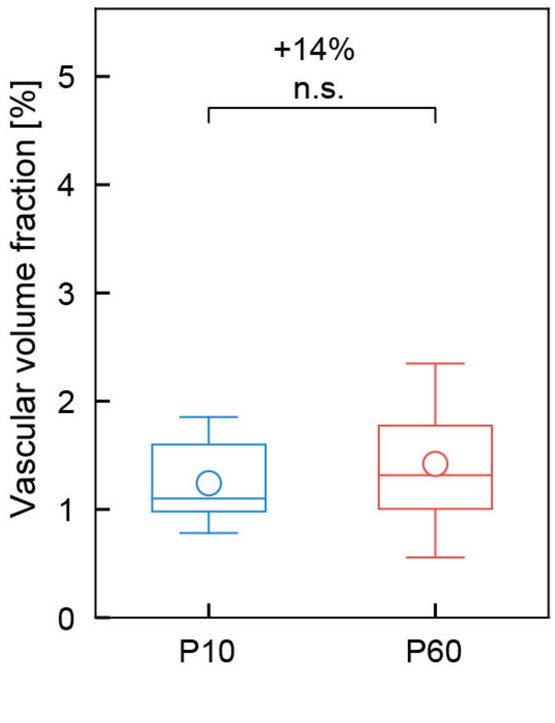
g
WT Cortex - non-capillaries
Vascular volume fraction [%]
+14%
n.s.
P10
P60

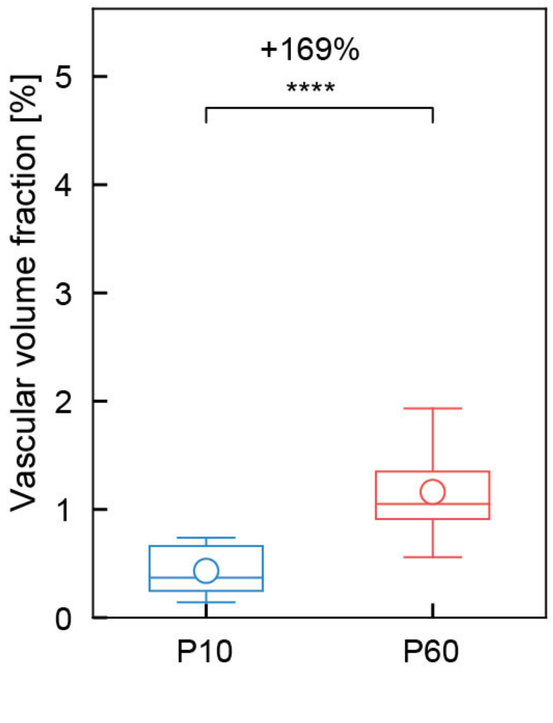
h
WT Cortex - capillaries
Vascular volume fraction [%]
+169%
****
P10
P60

Figure 8

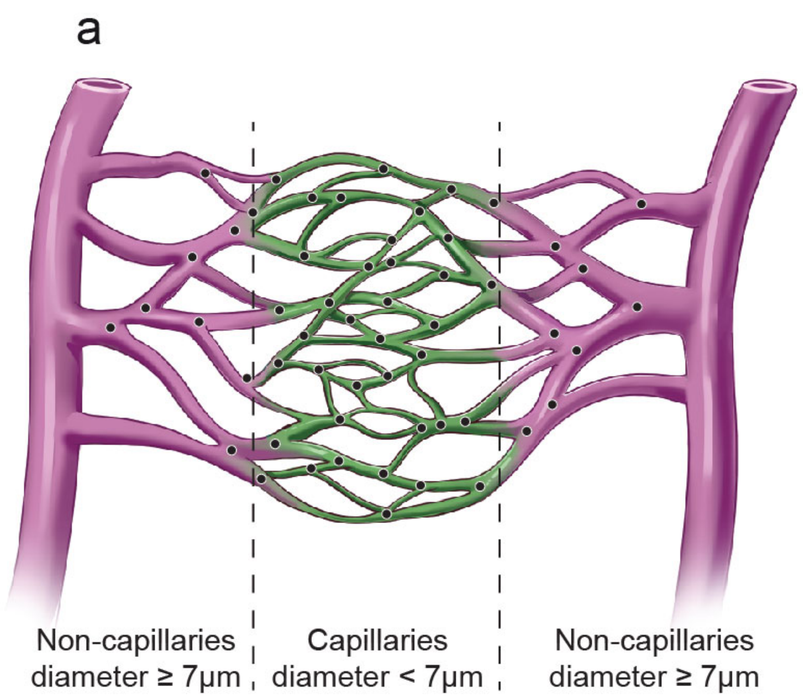
a
Non-capillaries
diameter ≥ 7µm
Capillaries
diameter < 7µm
Non-capillaries
diameter ≥ 7µm
Branchpoint

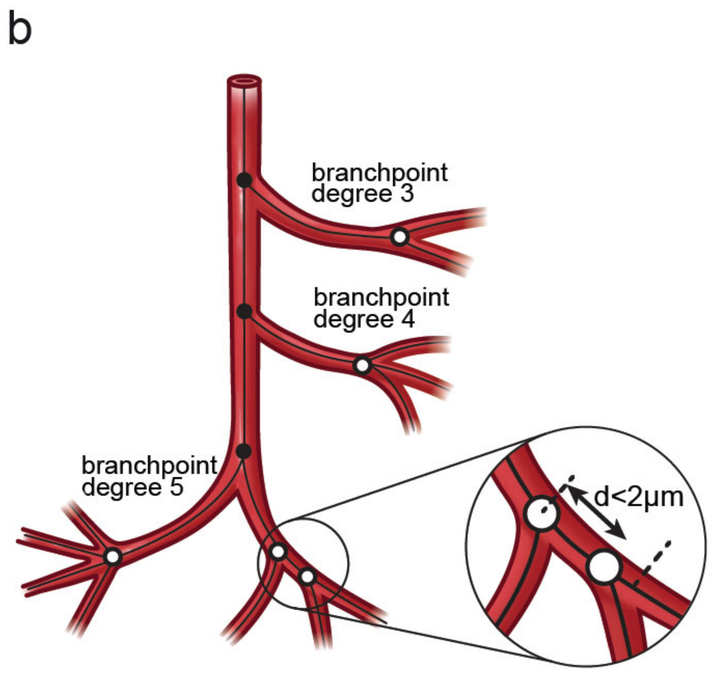
b
branchpoint
degree 3
branchpoint
degree 4
branchpoint
degree 5
d<2µm

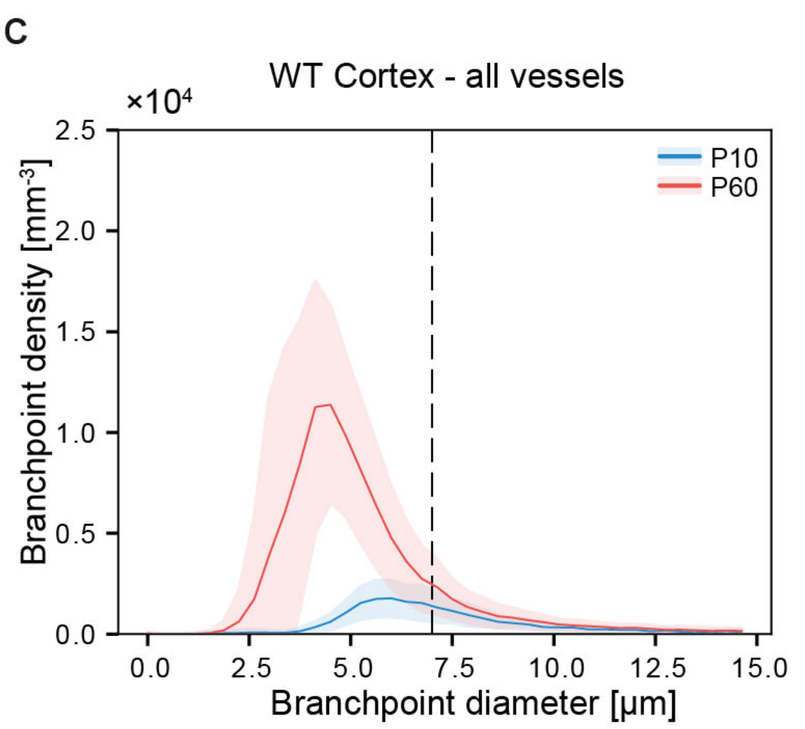
c
WT Cortex - all vessels
×10⁴
Branchpoint density [mm⁻³]
P10
P60
Branchpoint diameter [µm]

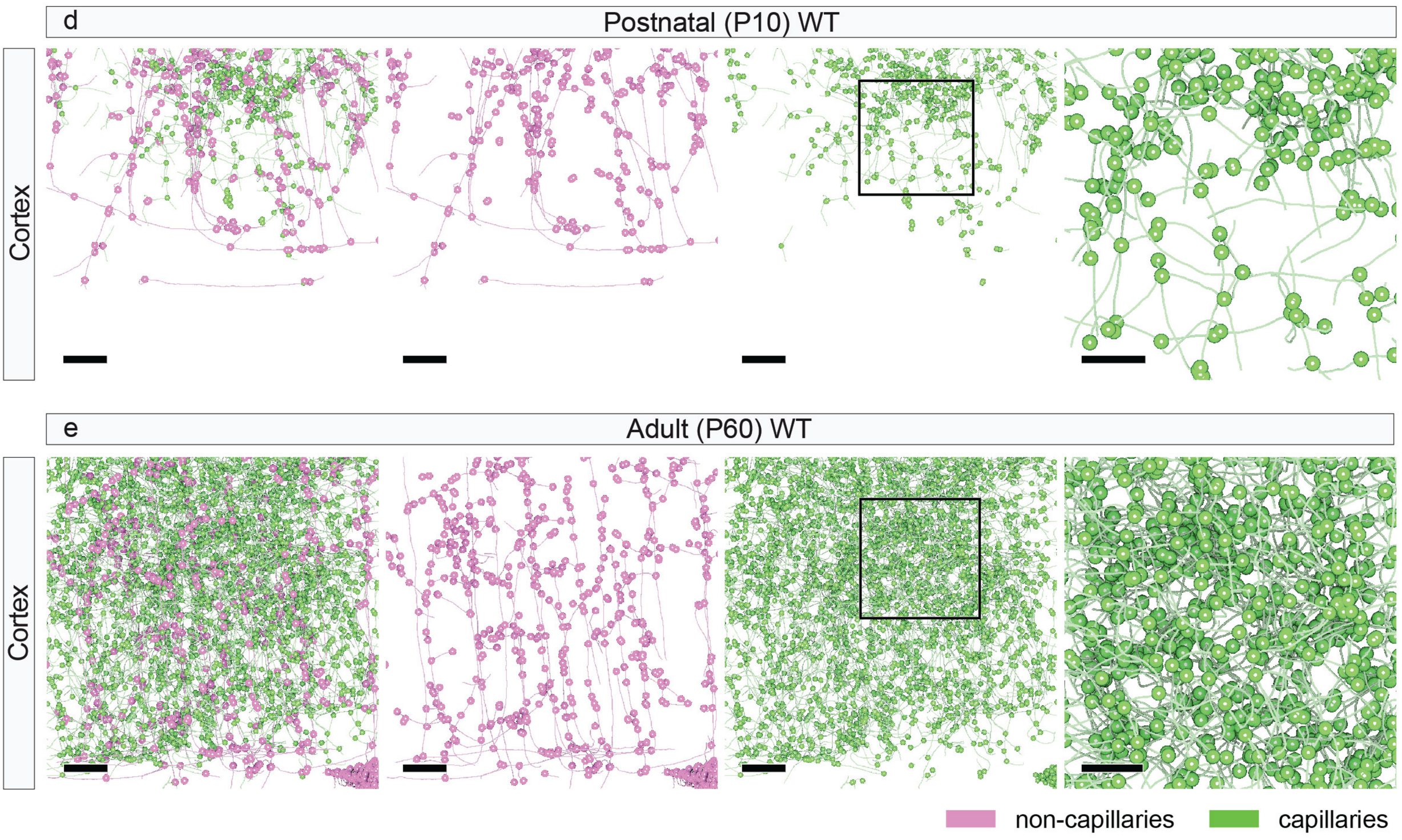
d
Postnatal (P10) WT
Cortex
e
Adult (P60) WT
Cortex
non-capillaries
capillaries

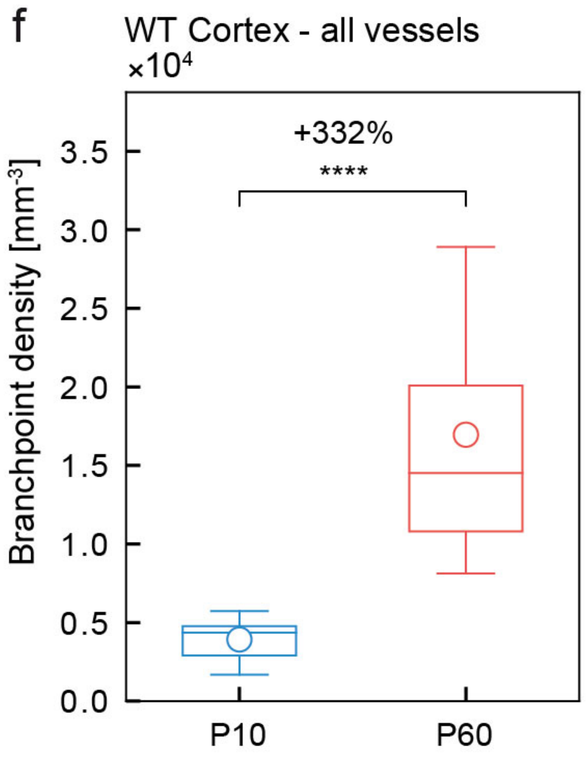
f
WT Cortex - all vessels
×10⁴
+332%
****
Branchpoint density [mm⁻³]
P10
P60

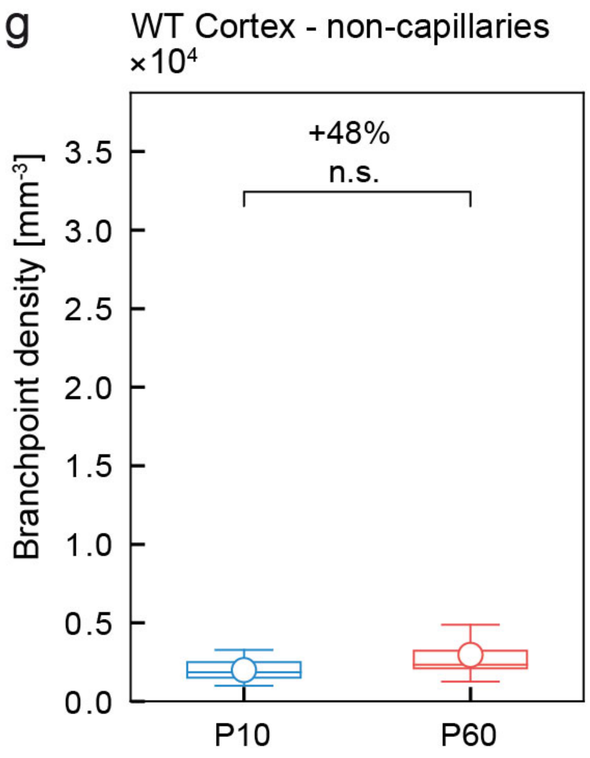
g
WT Cortex - non-capillaries
×10⁴
+48%
n.s.
Branchpoint density [mm⁻³]
P10
P60

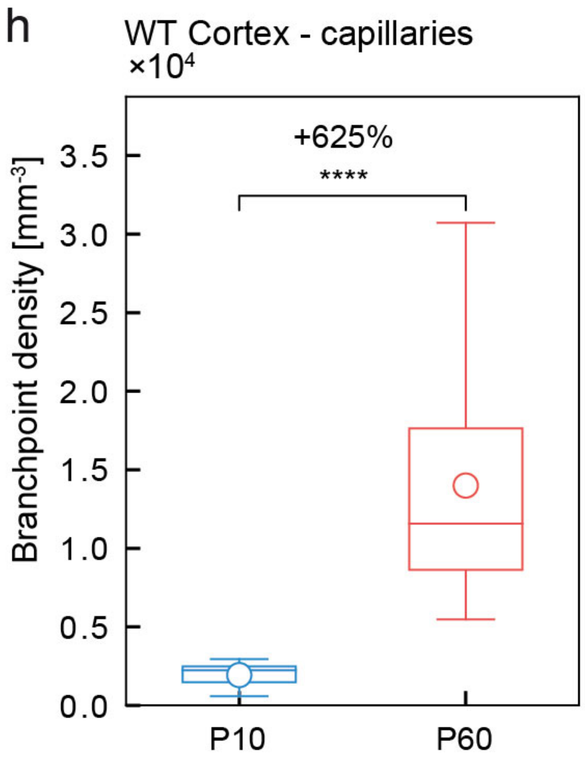
h
WT Cortex - capillaries
×10⁴
+625%
****
Branchpoint density [mm⁻³]
P10
P60

Figure 9

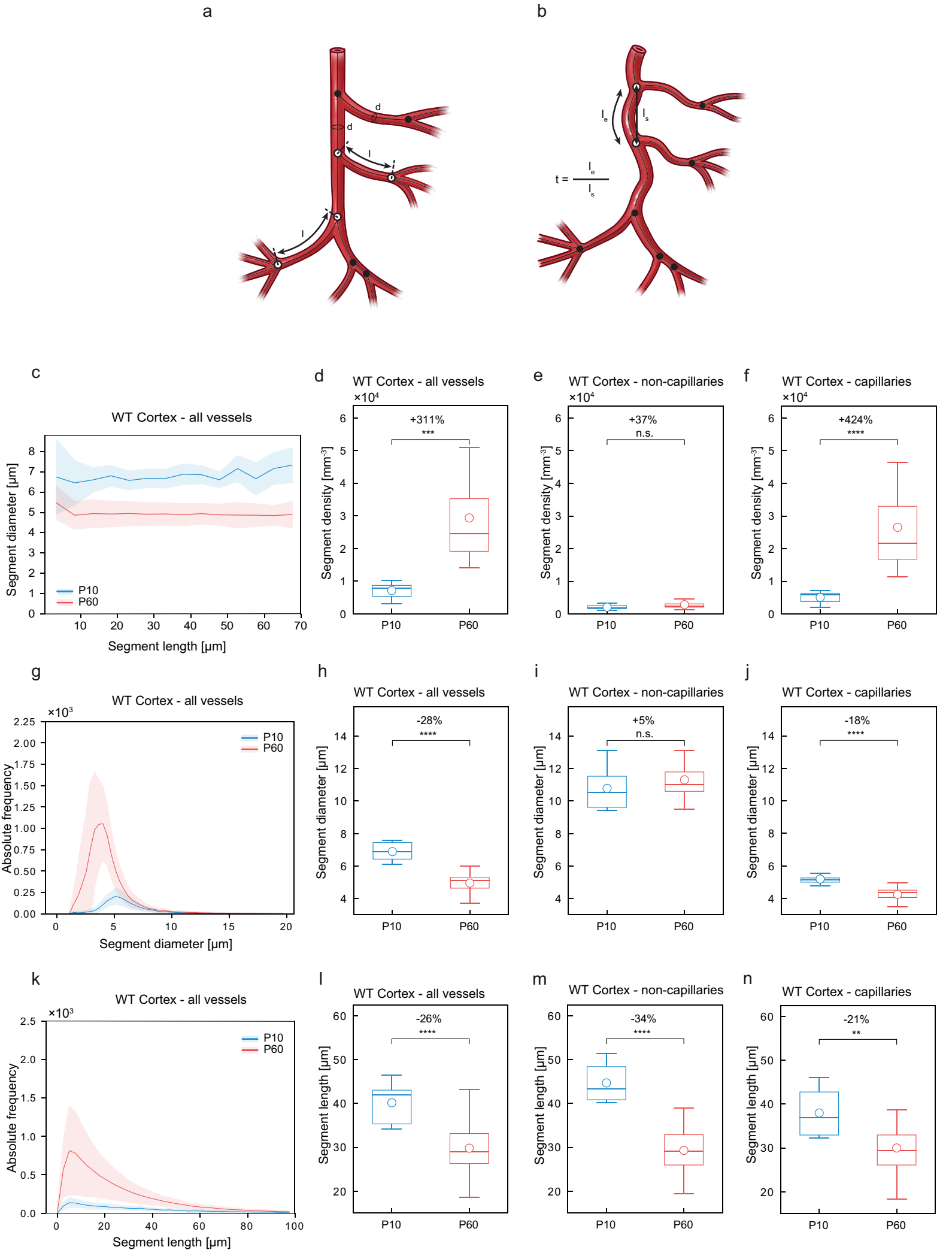
a
b
d
d
l
l
l_e
l_s
t = $\frac{l_e}{l_s}$
c
WT Cortex - all vessels
Segment diameter [µm]
Segment length [µm]
P10
P60
d
WT Cortex - all vessels
×10⁴
Segment density [mm⁻³]
+311%
***
P10
P60
e
WT Cortex - non-capillaries
×10⁴
Segment density [mm⁻³]
+37%
n.s.
P10
P60
f
WT Cortex - capillaries
×10⁴
Segment density [mm⁻³]
+424%
****
P10
P60
g
WT Cortex - all vessels
×10³
Absolute frequency
Segment diameter [µm]
P10
P60
h
WT Cortex - all vessels
Segment diameter [µm]
-28%
****
P10
P60
i
WT Cortex - non-capillaries
Segment diameter [µm]
+5%
n.s.
P10
P60
j
WT Cortex - capillaries
Segment diameter [µm]
-18%
****
P10
P60
k
WT Cortex - all vessels
×10³
Absolute frequency
Segment length [µm]
P10
P60
l
WT Cortex - all vessels
Segment length [µm]
-26%
****
P10
P60
m
WT Cortex - non-capillaries
Segment length [µm]
-34%
****
P10
P60
n
WT Cortex - capillaries
Segment length [µm]
-21%
**
P10
P60

Figure 10

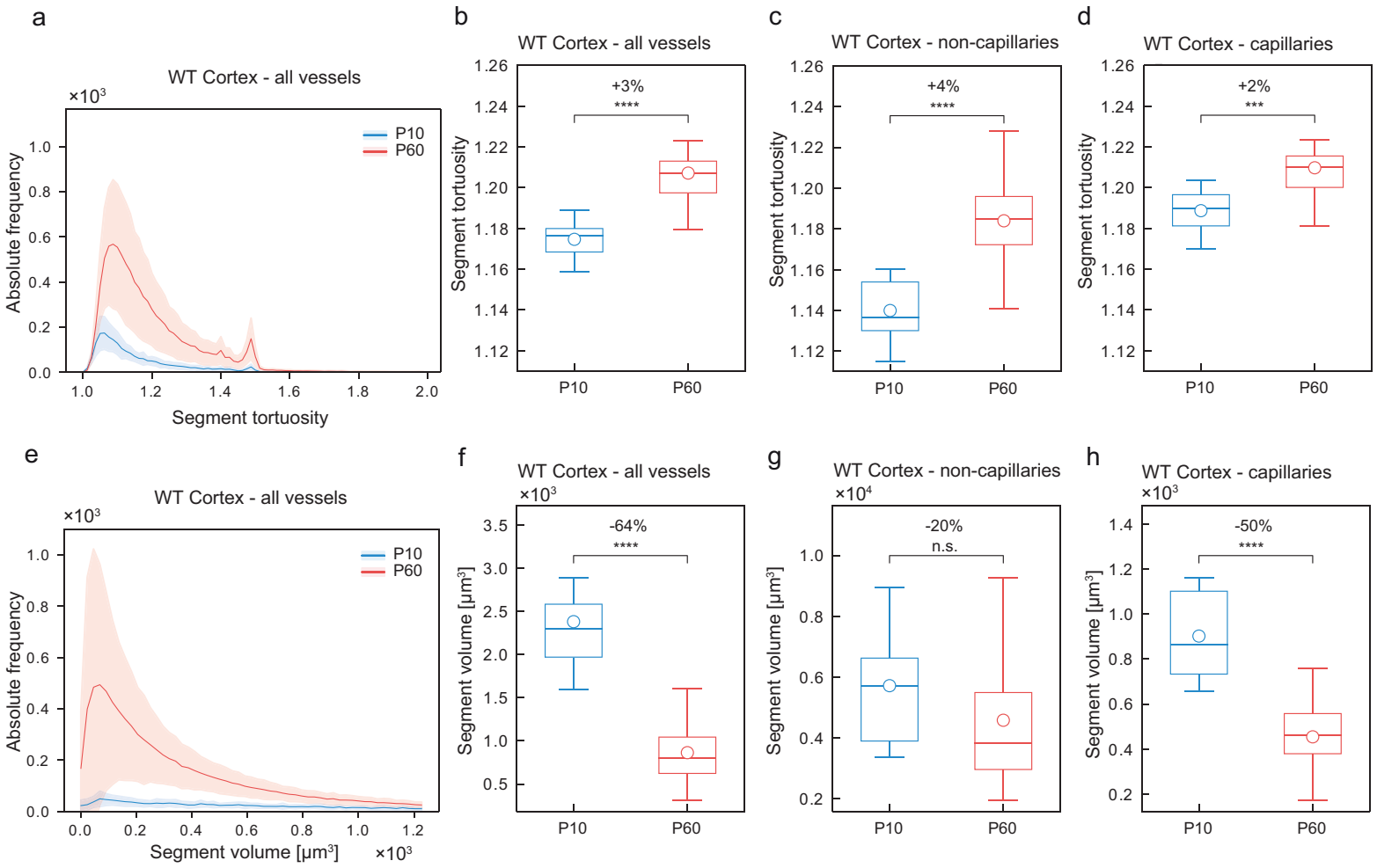
a
WT Cortex - all vessels
×10³
P10
P60
Absolute frequency
Segment tortuosity
b
WT Cortex - all vessels
+3%
****
Segment tortuosity
P10
P60
c
WT Cortex - non-capillaries
+4%
****
Segment tortuosity
P10
P60
d
WT Cortex - capillaries
+2%
***
Segment tortuosity
P10
P60
e
WT Cortex - all vessels
×10³
P10
P60
Absolute frequency
Segment volume [µm³]
×10³
f
WT Cortex - all vessels
×10³
-64%
****
Segment volume [µm³]
P10
P60
g
WT Cortex - non-capillaries
×10⁴
-20%
n.s.
Segment volume [µm³]
P10
P60
h
WT Cortex - capillaries
×10³
-50%
****
Segment volume [µm³]
P10
P60

Figure 11

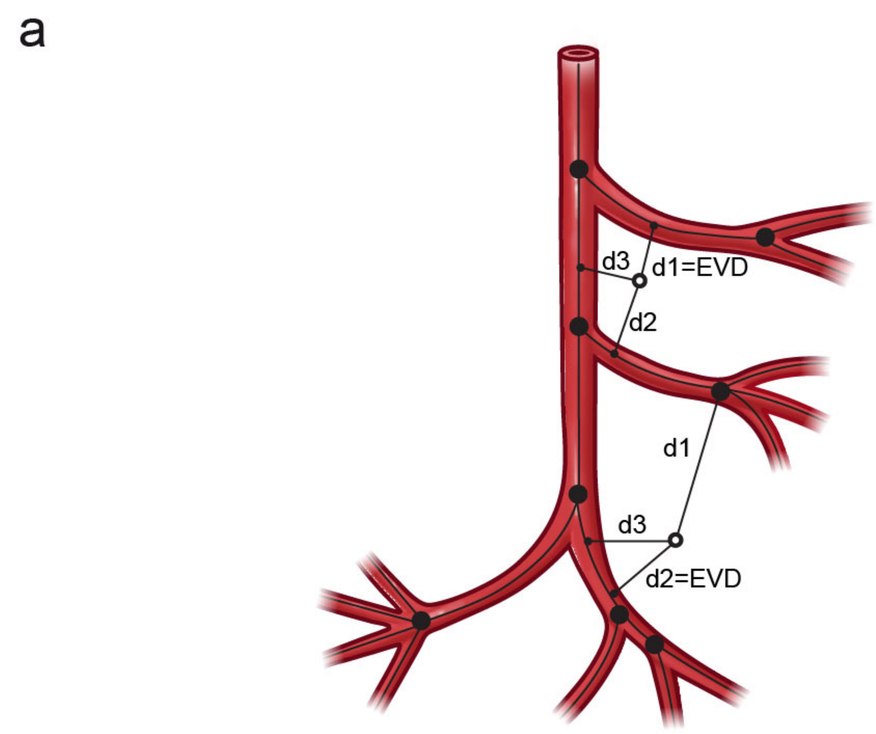
a
d3
d1=EVD
d2
d1
d3
d2=EVD

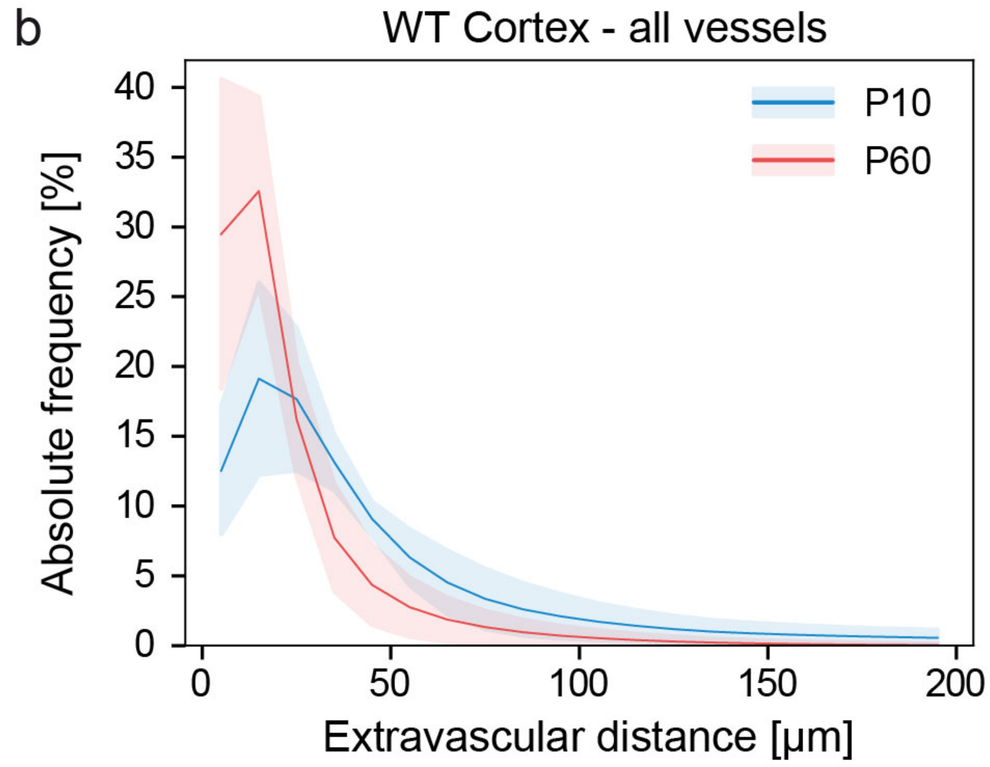
b
WT Cortex - all vessels
P10
P60
Absolute frequency [%]
Extravascular distance [µm]

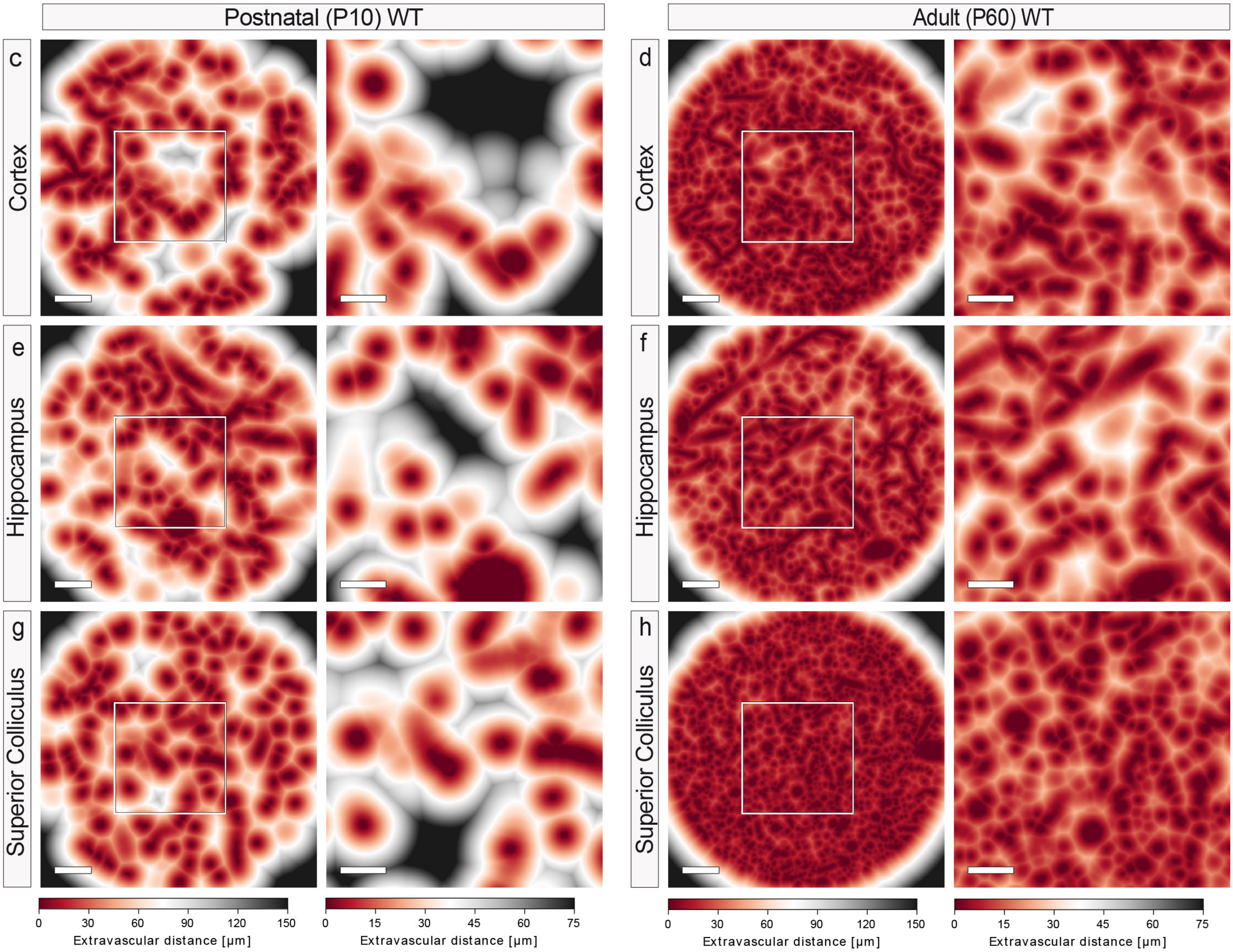
Postnatal (P10) WT
Adult (P60) WT
c
d
e
f
g
h
Cortex
Hippocampus
Superior Colliculus
0 30 60 90 120 150
Extravascular distance [µm]
0 15 30 45 60 75
Extravascular distance [µm]

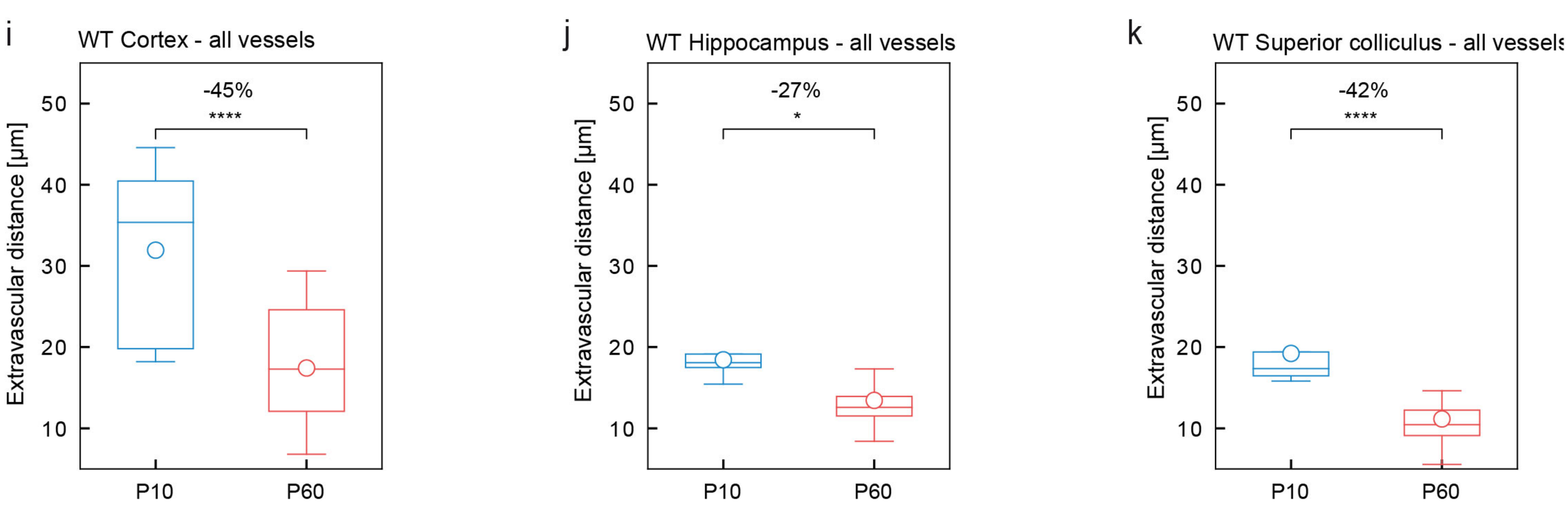
i
WT Cortex - all vessels
-45%
****
j
WT Hippocampus - all vessels
-27%
*
k
WT Superior colliculus - all vessels
-42%
****
Extravascular distance [µm]
P10
P60

Figure 12

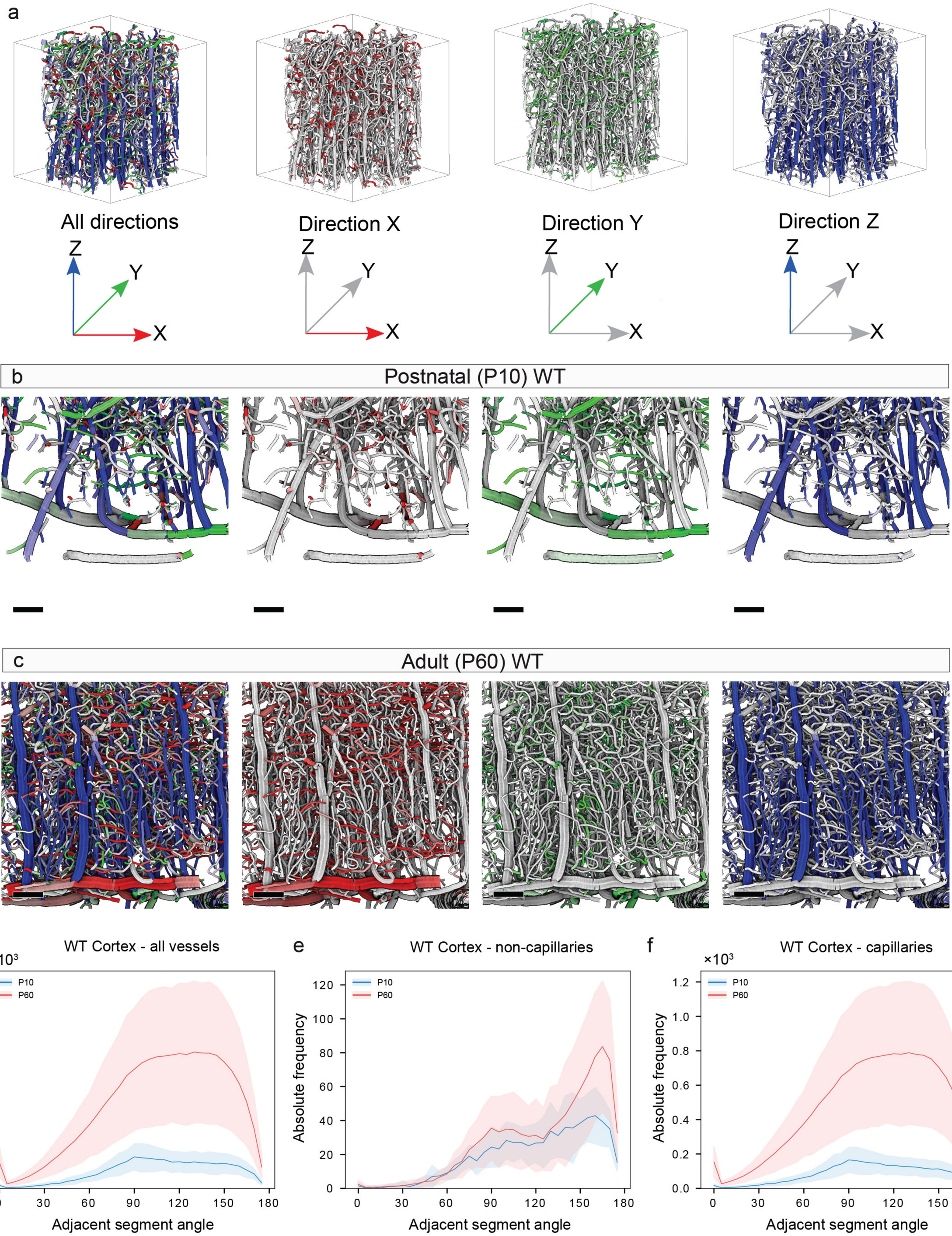
a
All directions
Direction X
Direction Y
Direction Z
Z
Y
X
b
Postnatal (P10) WT
Cortex
c
Adult (P60) WT
Cortex
d
WT Cortex - all vessels
e
WT Cortex - non-capillaries
f
WT Cortex - capillaries
×10³
P10
P60
Absolute frequency
Adjacent segment angle
0
30
60
90
120
150
180
0.0
0.2
0.4
0.6
0.8
1.0
1.2
20
40
80
100
120

Figure 13

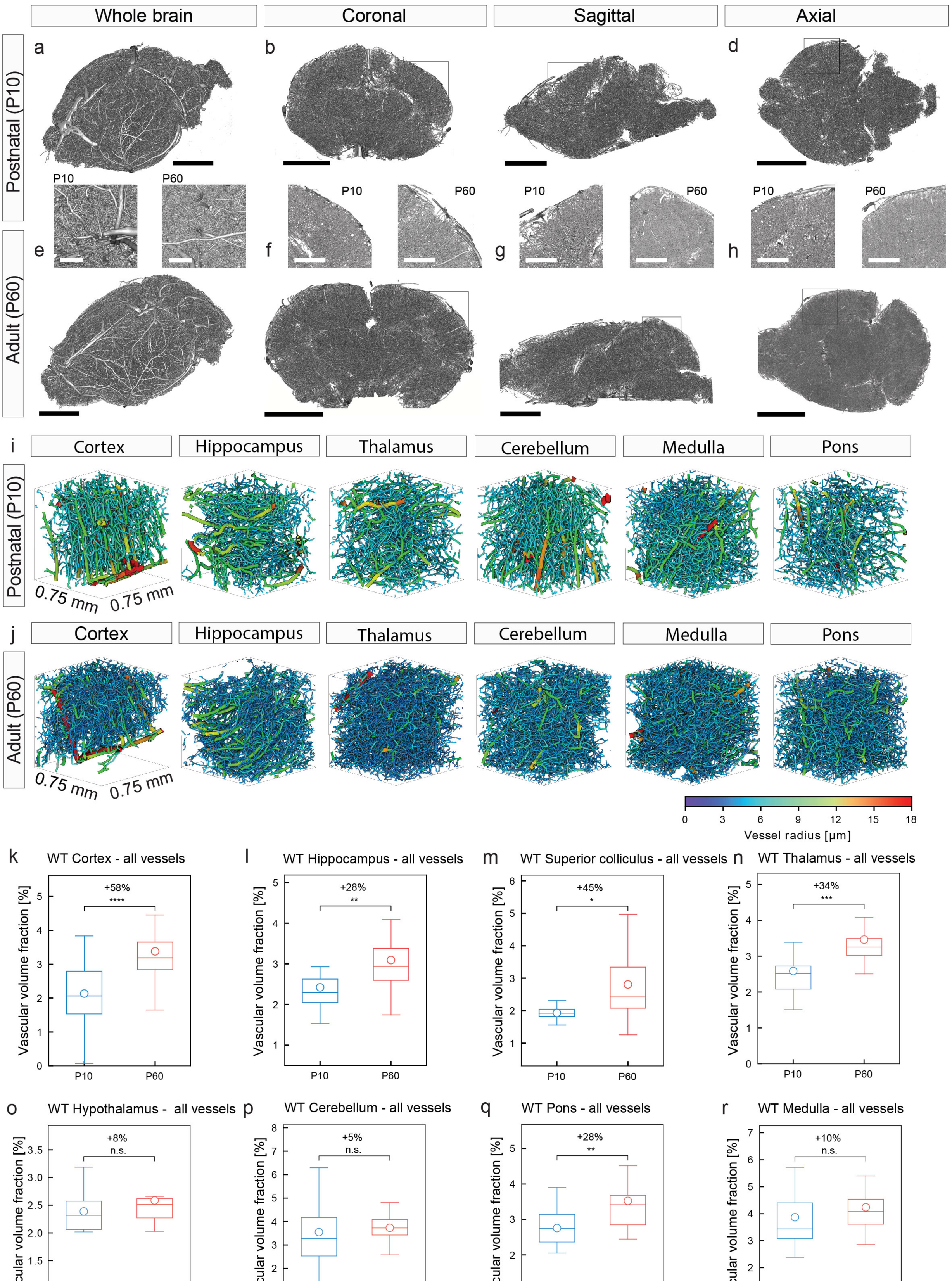
Whole brain
Coronal
Sagittal
Axial
Postnatal (P10)
Adult (P60)
a
b
d
P10
P60
e
f
g
h
i
Cortex
Hippocampus
Thalamus
Cerebellum
Medulla
Pons
0.75 mm
0.75 mm
j
0
3
6
9
12
15
18
Vessel radius [µm]
k
WT Cortex - all vessels
+58%
****
l
WT Hippocampus - all vessels
+28%
**
m
WT Superior colliculus - all vessels
+45%
*
n
WT Thalamus - all vessels
+34%
***
Vascular volume fraction [%]
o
WT Hypothalamus - all vessels
+8%
n.s.
p
WT Cerebellum - all vessels
+5%
n.s.
q
WT Pons - all vessels
+28%
**
r
WT Medulla - all vessels
+10%
n.s.

Figure 14

a Whole brain

b Cortex

c Hippocampus

d Superior colliculus

Postnatal (P10)

Adult (P60)

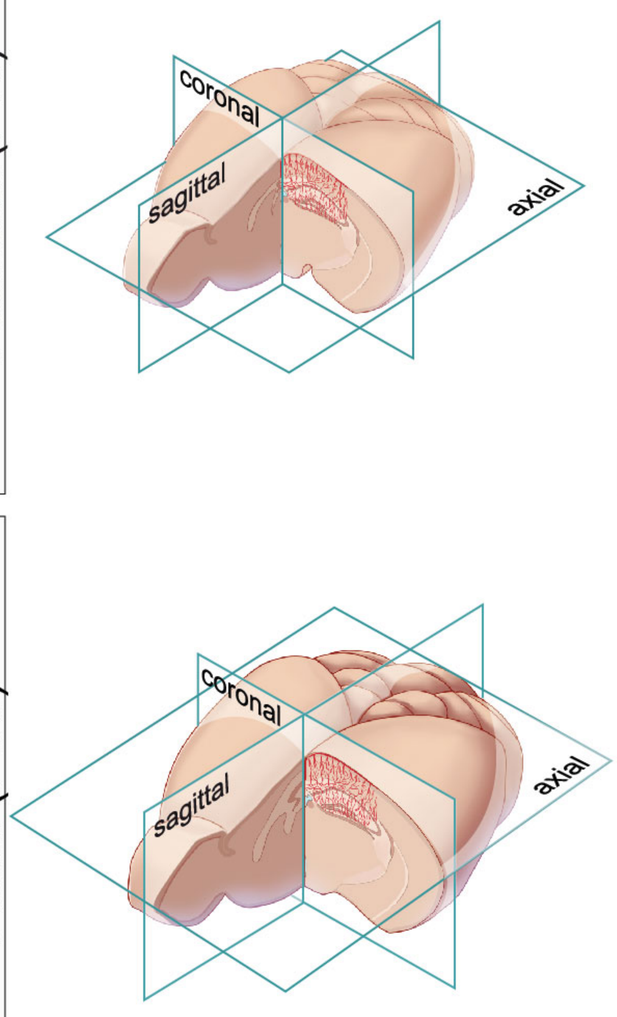

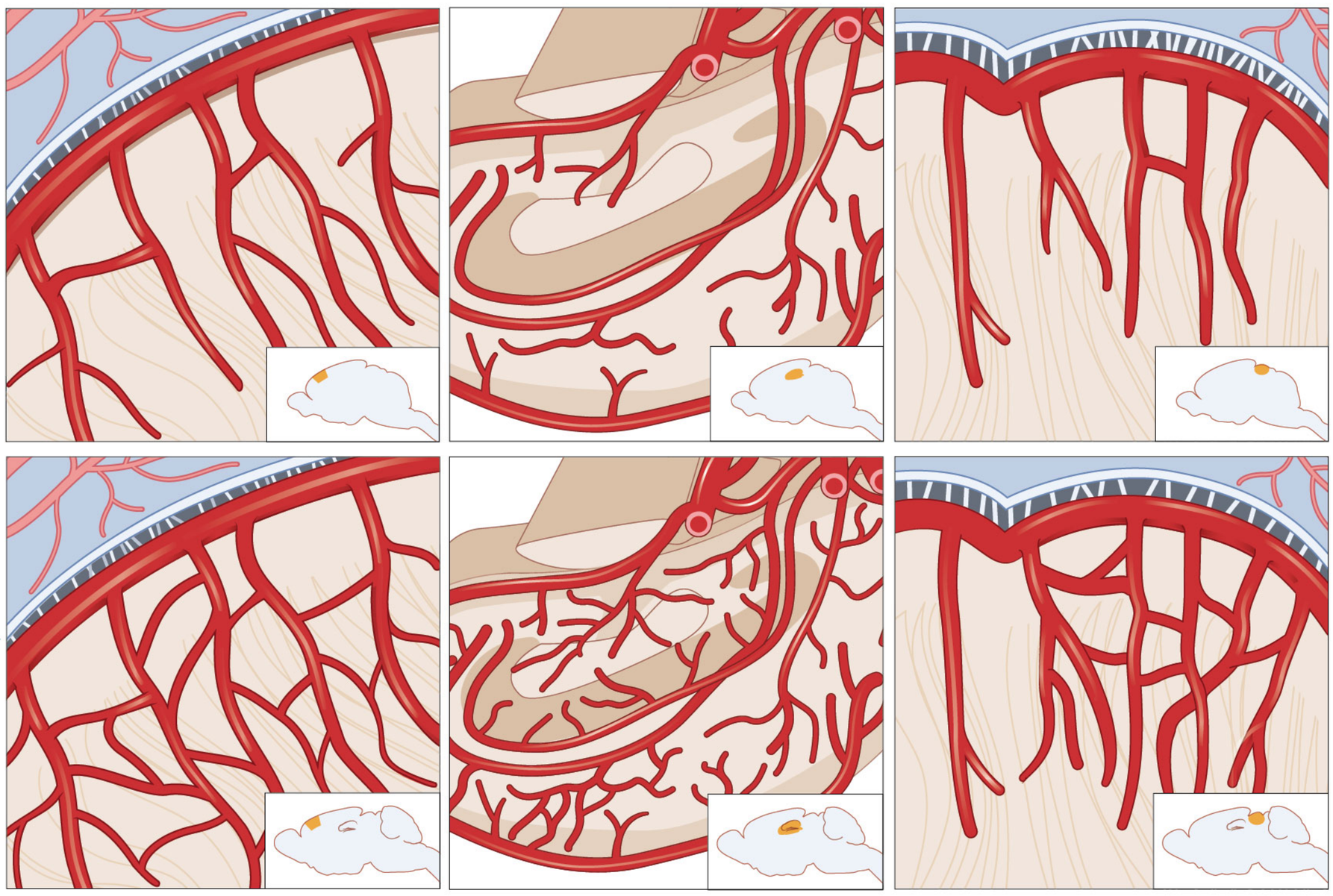

Vascular network

e

f

Postnatal (P10)

Adult (P60)



g Vascular parameters

Vascular volume fraction (%)

Branchpoint/segment density (mm^{-3})

Branchpoint degree

Vessel tortuosity

Segment length (μm) - volume ($μm^3$)

Segment/branchpoint diameter (μm)

Extravascular distance (μm)

Vessel directionality (adjacent segment angle)

P10

P60

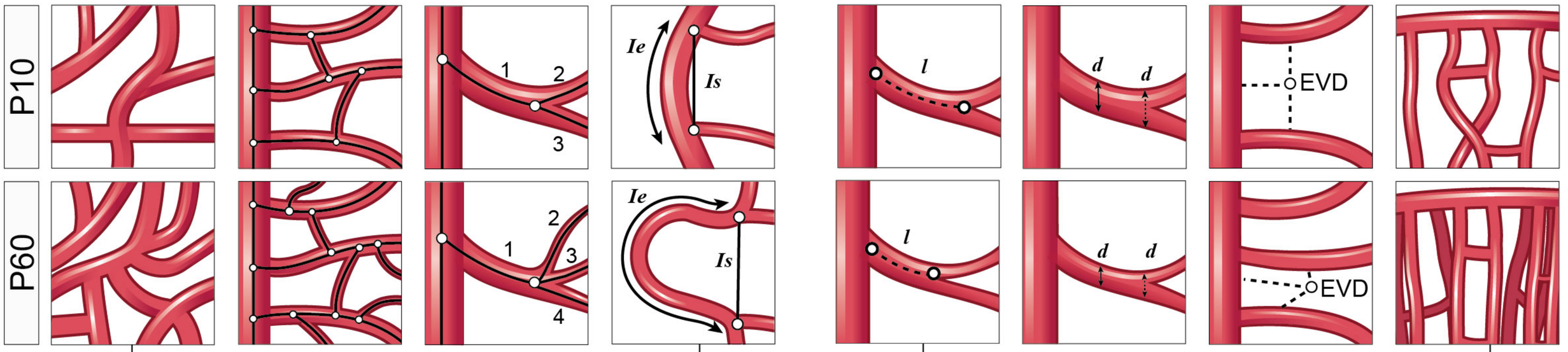

Increase

Decrease

Segment diameter

Branchpoint diameter

d = diameter

l = length

Extended Data Figure 1

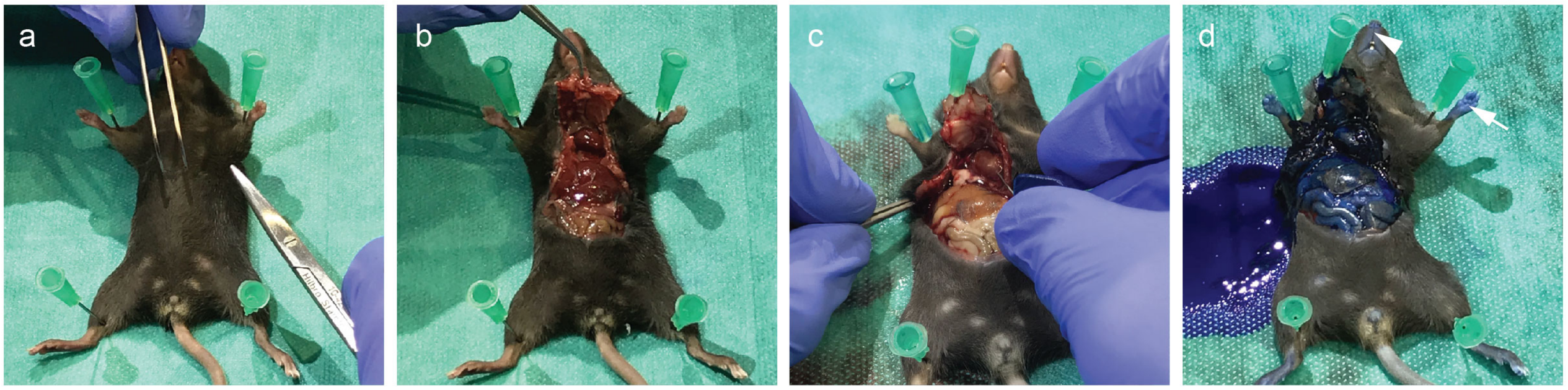

Extended Data Figure 2

a

b

Adult (P60)

c

d

Postnatal (P10) WT - Cortex

e

f

Postnatal (P10) WT - Cortex

Extended Data Figure 3

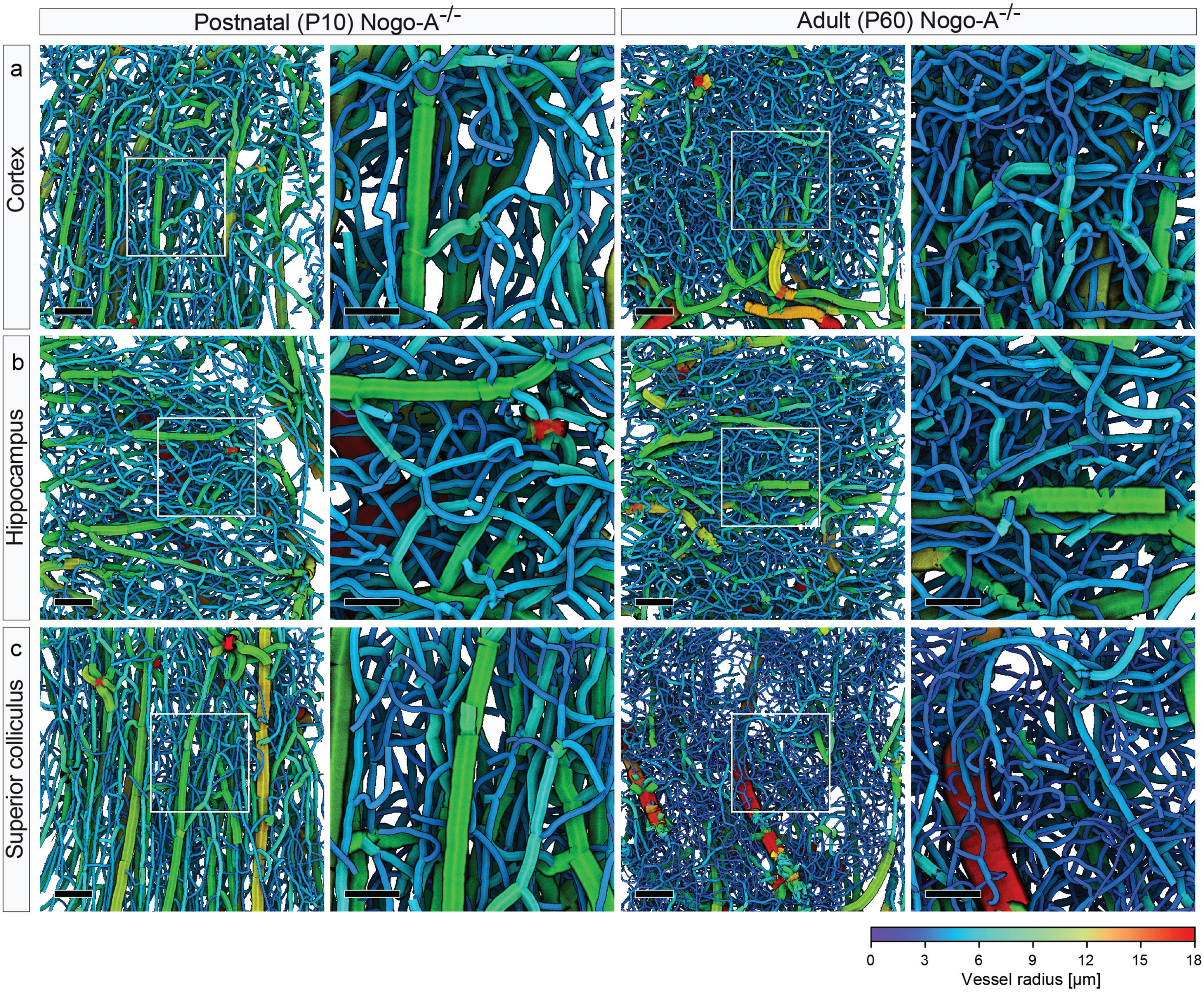

Extended Data Figure 4

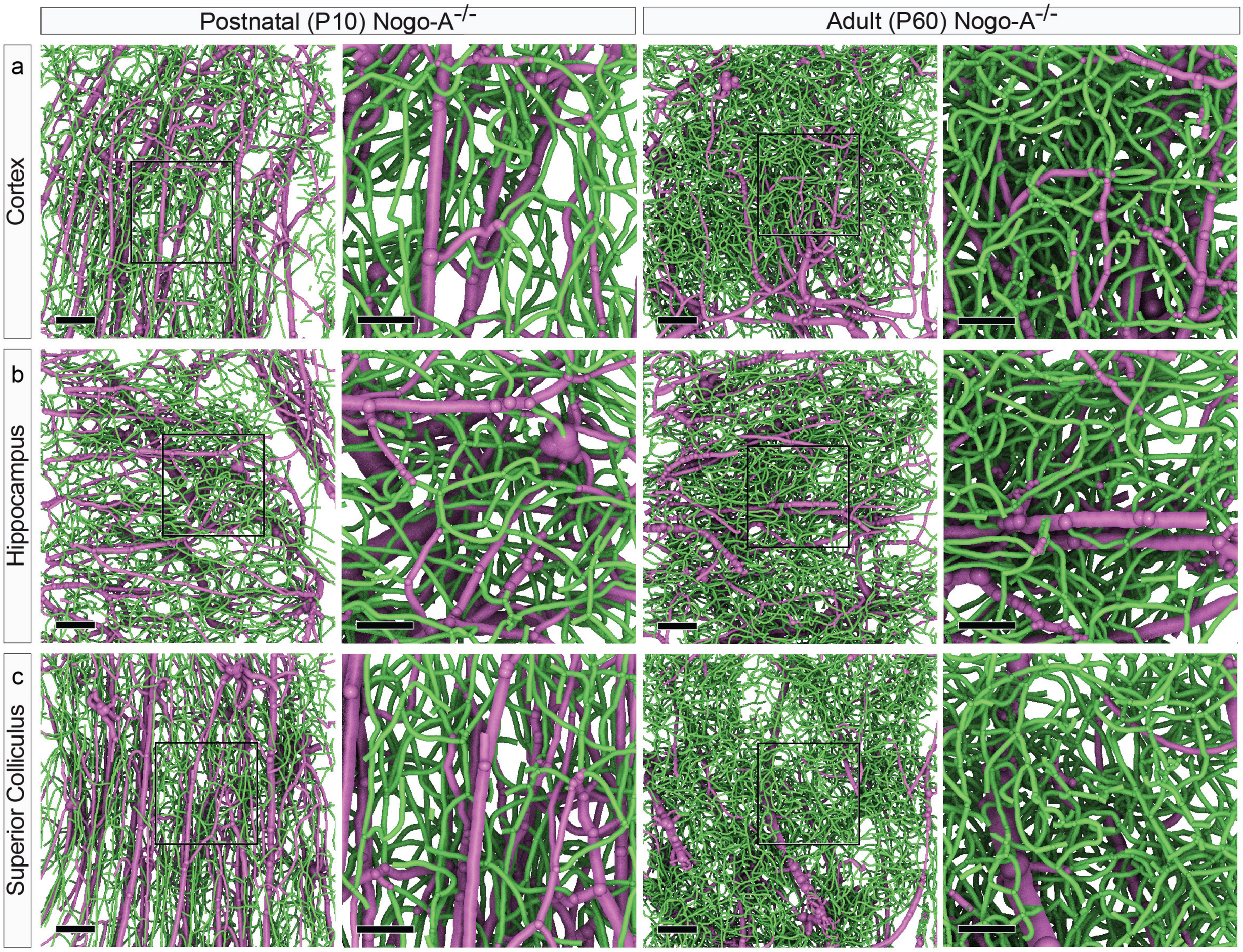

Extended Data Figure 5

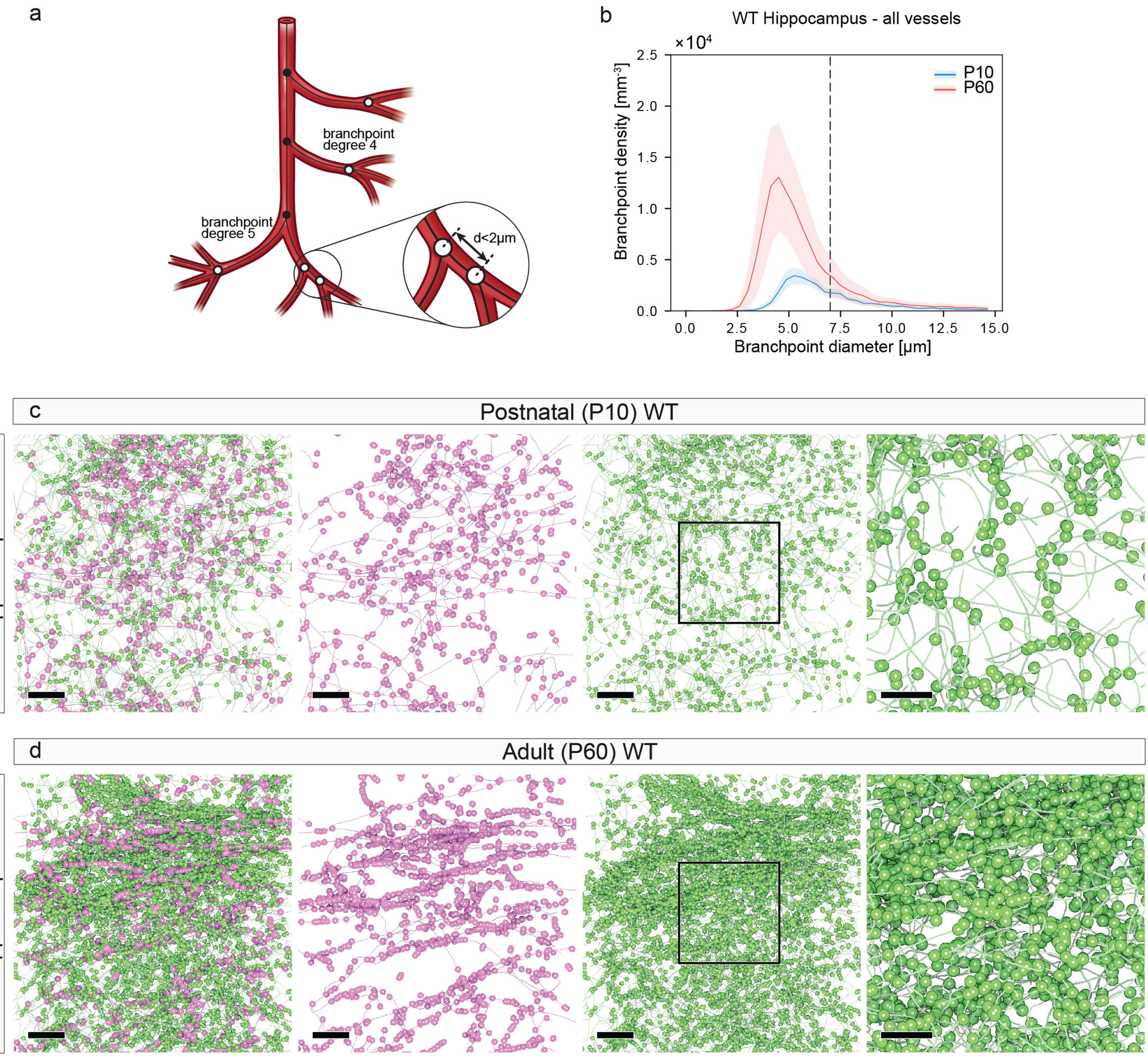

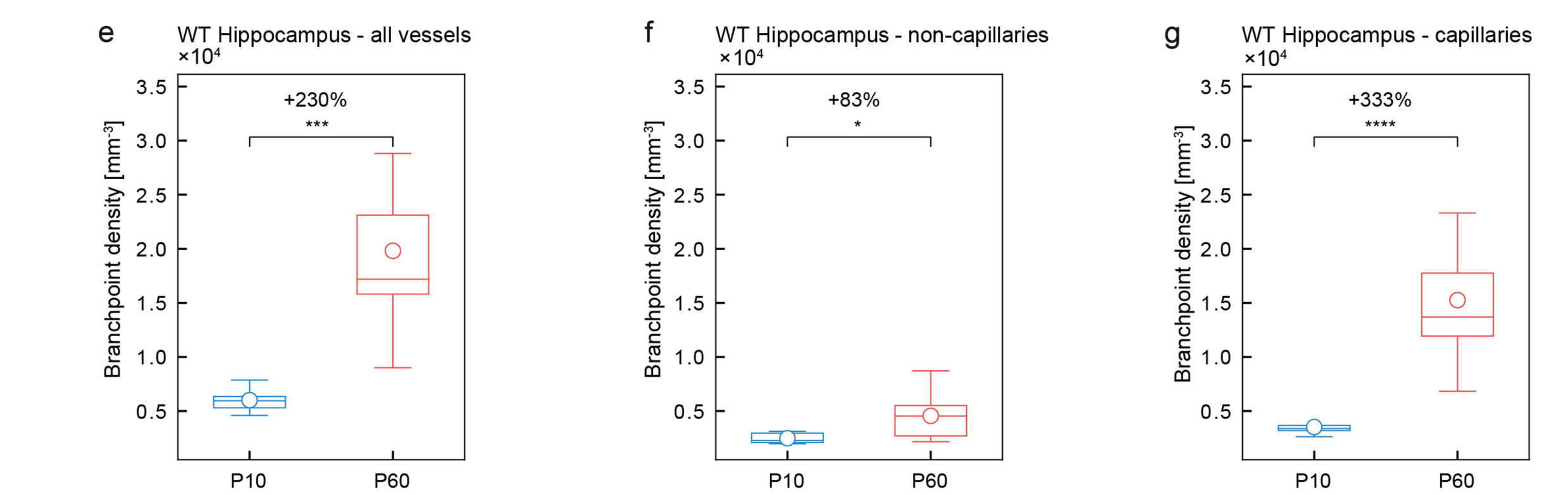

Extended Data Figure 6

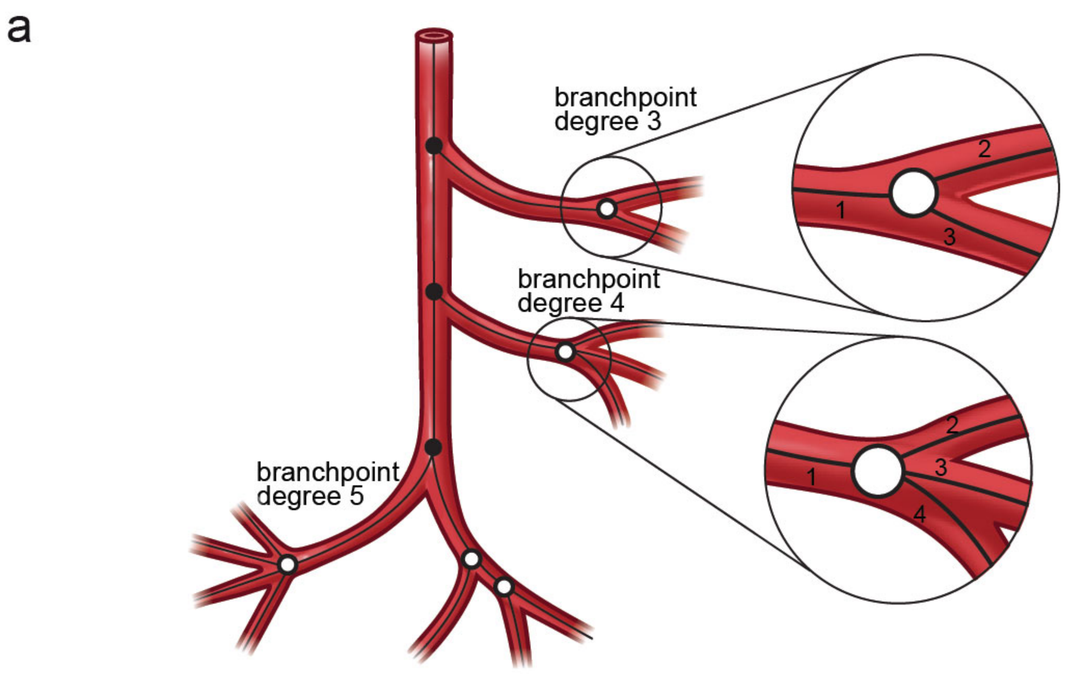

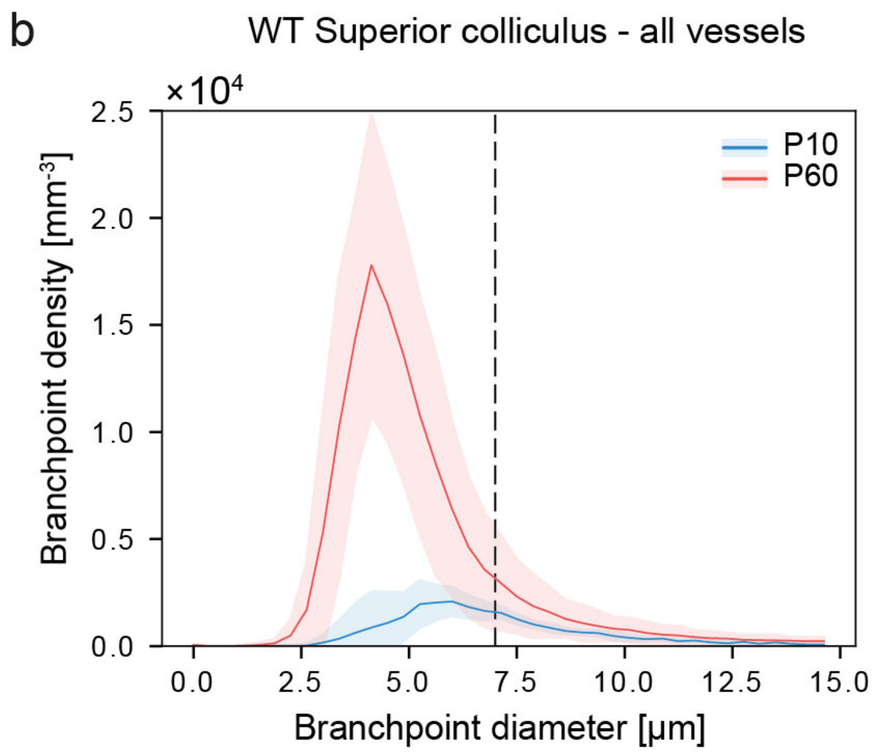

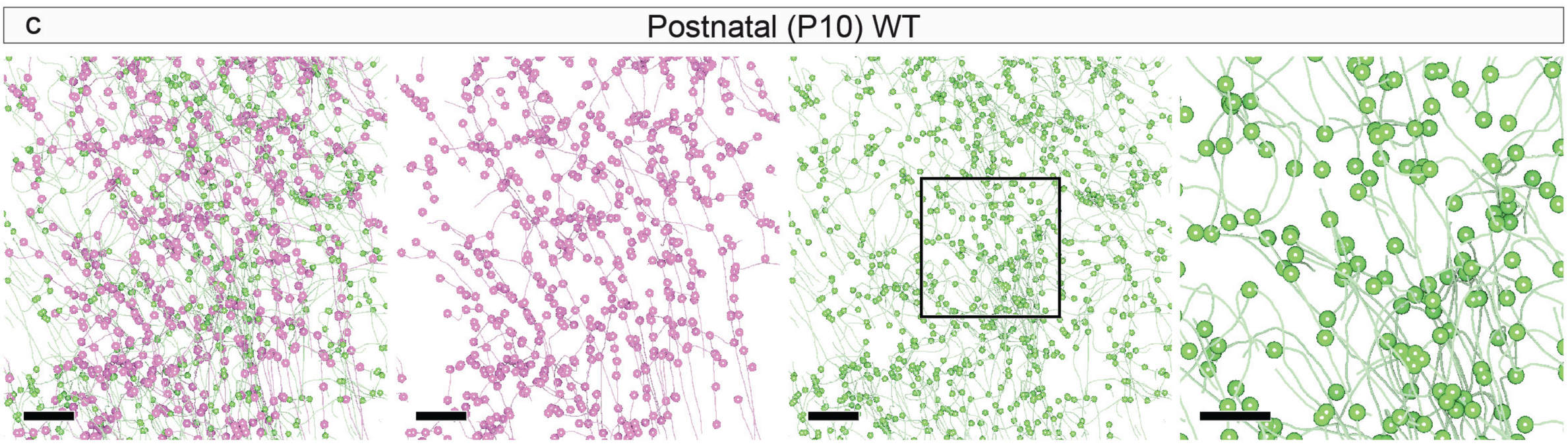

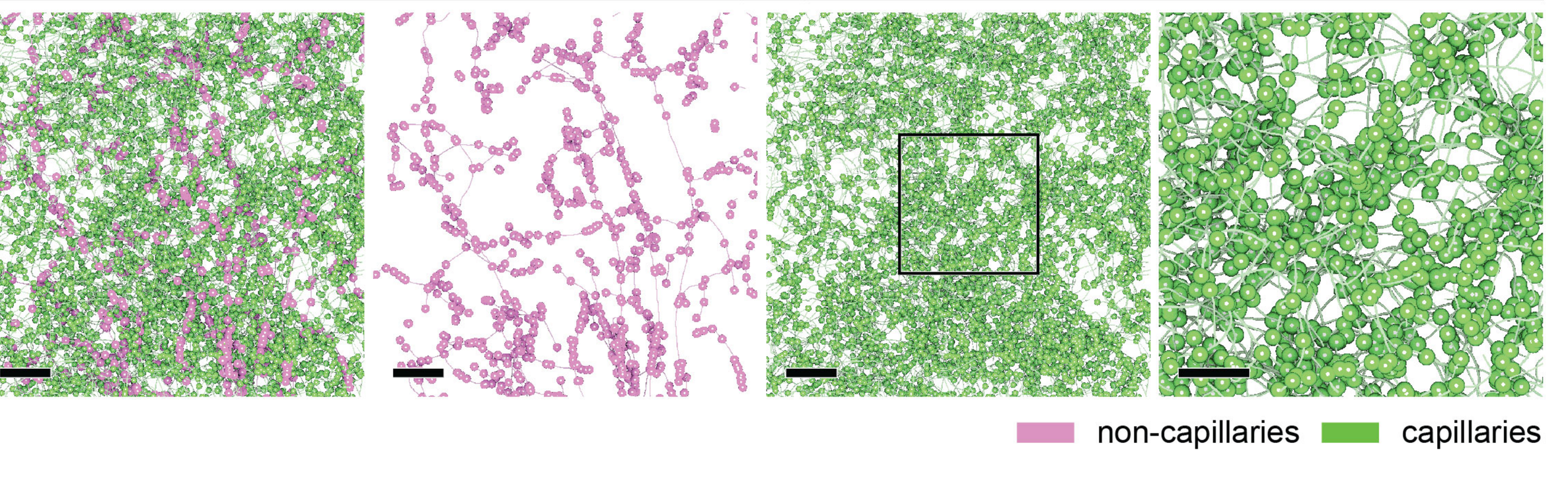

Extended Data Figure 7

